

# Investigation of muons in extensive air showers with the KASCADE-Grande Muon Tracking Detector

Paweł Łuczak

NATIONAL CENTRE FOR NUCLEAR RESEARCH,  
DEPARTMENT OF COSMIC RAY PHYSICS IN ŁÓDŹ,  
POLAND



*Thesis submitted in partial fulfilment  
of the requirements for the degree of  
Doctor of Philosophy in Physics*

*Supervised by prof. dr hab. Janusz Zabierowski*

Łódź, 2012



# Acknowledgements

I am very grateful to my supervisor prof. dr hab. Janusz Zabierowski for giving me possibility of working in KASCADE-Grande experiment and for many valuable suggestions, guidance and patience in course of preparation of this thesis.

I would like to thank dr Paul Doll for his valuable help during my stays in Germany, introduction to the KASCADE-Grande experiment, analysis techniques and countless, inspiring and fruitful discussions about physics and data analysis.

I would like to thank dr Andreas Haungs for help during my stays in Germany and valuable comments and discussions.

I would like to thank all my colleagues from the KASCADE-Grande collaboration for discussions and friendly atmosphere.

This work has been partially supported by Polish Ministry of Science and Higher Education grant No. NN 202 033836 and by Polish-German mobility grants PPP-DAAD/MNISW for years: 2007-2008 and 2009-2010.



# Contents

<b>Introduction</b>	1
<b>1 Cosmic rays and Extensive Air Showers</b>	<b>4</b>
1.1 The primary energy spectrum of cosmic rays	4
1.2 The mass composition of cosmic rays	8
1.3 Extensive Air Showers	9
1.3.1 The hadronic component	11
1.3.2 The electromagnetic component	12
1.3.3 The muonic component	13
1.3.4 Development of EAS for different primaries	14
1.4 EAS detection techniques	16
1.4.1 Arrays of particle detectors	16
1.4.2 Fluorescent light detectors	17
1.4.3 Air Cherenkov light detectors	18
1.4.4 Radio-emission detectors	19
1.4.5 Hybrid detector systems	19
<b>2 Simulations of EAS</b>	<b>20</b>
2.1 The purpose of the EAS simulations	20
2.2 EAS simulations in the KASCADE-Grande experiment	23
2.3 Short characteristics of high energy hadronic interaction models used in KASCADE-Grande	25
<b>3 The KASCADE / KASCADE-Grande EAS experiment</b>	<b>27</b>
3.1 Detector components of the experiment	28
3.1.1 The KASCADE detector Array	29
3.1.2 The Grande detector Array	31
3.1.3 The Central Detector	32
3.1.4 The Muon Tracking Detector	33
3.1.5 The Piccolo Array	33
3.2 The reconstruction of EAS	33
3.2.1 Reconstruction of arrival direction	34
3.2.2 Charge particle shower size and the slope of lateral distribution	34

3.2.3	Muon shower size- $N_\mu$ . . . . .	35
3.2.4	Iterative procedure of the event reconstruction . . . . .	36
3.2.5	Trigger and reconstruction efficiency . . . . .	37
3.2.6	Reconstruction accuracy . . . . .	38
3.2.7	An example of an EAS event . . . . .	41
<b>4</b>	<b>The Muon Tracking Detector</b>	<b>43</b>
4.1	Design of the MTD . . . . .	43
4.1.1	Streamer tube chamber design . . . . .	44
4.1.2	Detector module design . . . . .	45
4.1.3	Gas supply system . . . . .	46
4.1.4	Readout and data acquisition electronics . . . . .	46
4.2	Operation of the MTD . . . . .	48
4.2.1	Operation of a streamer tube chamber . . . . .	48
4.2.2	Event handling . . . . .	48
4.2.3	Reconstruction of the muon directions . . . . .	50
<b>5</b>	<b>Selection of the experimental data</b>	<b>51</b>
5.1	Selection of showers . . . . .	51
5.2	Selection of muons . . . . .	53
5.3	Analysis of the simulated data . . . . .	54
<b>6</b>	<b>Lateral muon density distributions</b>	<b>56</b>
6.1	Data selection and analysis . . . . .	56
6.2	Results and discussion . . . . .	58
<b>7</b>	<b>Pseudorapidity of muons in EAS</b>	<b>64</b>
7.1	Radial and tangential angle . . . . .	64
7.2	Pseudorapidity . . . . .	66
7.3	Shower and muon selection . . . . .	68
7.4	Tests of interaction models with pseudorapidity distributions	72
<b>8</b>	<b>Primary mass sensitivity of mean muon pseudorapidity</b>	<b>74</b>
8.1	Selection of shower events . . . . .	75
8.2	Data analysis and results . . . . .	77
<b>9</b>	<b>Muon production height studies</b>	<b>83</b>
9.1	Reconstruction of muon production height . . . . .	84
9.2	Muon production heights in showers induced by light and heavy primary masses . . . . .	86
9.3	Test of hadronic interaction models with muon production heights . . . . .	88
9.4	Cosmic ray composition derived with the muon production heights . . . . .	90

<b>10 Summary</b>	<b>92</b>
<b>A Selection of the experimental and simulated showers</b>	<b>96</b>
<b>B Lateral muon density distributions</b>	<b>98</b>
<b>C Pseudorapidity of muons in EAS</b>	<b>101</b>
<b>D Primary mass sensitivity of mean pseudorapidity</b>	<b>106</b>
<b>List of Tables</b>	<b>110</b>
<b>Bibliography</b>	<b>111</b>



# Introduction

Cosmic rays (CR) are the matter particles coming from the outer space and continuously bombarding the Earth atmosphere. They were first discovered in 1912 by Austrian physicist Victor Hess [1], who during several balloon flights observed that ionization of the air is increasing with the altitude. This could not be explained with natural radiation from Earth's crust. His conclusion was that radiation has its source in the outer space. Robert Millikan confirmed Hess discovery in 1925 and introduced the name "cosmic rays". Victor Hess received the Nobel Prize in Physics in 1936.

This discovery opened a new fruitful field of research in physics. In the late 1920s it was discovered by Jacob Clay that cosmic radiation consists, to some part at least, of charged particles. In the late 1930s the coincidence of signals from separated detectors was observed. This measurement lead to the development of the idea of an extensive air shower (EAS) [2]: charged particles that are ionizing the atmosphere are particles of the cascades generated by the interaction of high energy primary particles with air nuclei.

In the late 1940s measurements obtained with detectors attached to high-altitude balloons revealed the nature of primary particles. Most of them occur to be hydrogen and helium nuclei and abundance of other elements is very similar to that in the solar system.

Today the term "cosmic rays" refers to nuclei of elements, electrons, positrons and photons. Their energies range from a few GeV to more than  $10^{11}$  GeV and their flux decreases within this energy range by 32 orders of magnitude.

Due to this steep energy spectrum direct investigations of CR are only possible to an energy slightly above  $10^{14}$  eV. At higher energies the CR measurements become indirect, by means of studying the EAS phenomenon.

Large detector arrays have been built all over the world to study various components of EAS at different observation levels. Reconstruction of shower parameters allows to infer the properties of primary cosmic ray particles: their masses and energies, possibly the mechanisms of their acceleration and propagation, as well as to search for the sources of their origin. However, this inference relies heavily on the computer simulations of EAS development using the hadronic interaction models in the kinematical re-

gions not accessible for accelerator measurements. The KASCADE-Grande EAS experiment, which is the experimental environment of the investigations presented in this work, is a classical example of such installations.

Due to the efforts of many research teams all over the world, especially in the last few decades, our knowledge on CRs became quite substantial. However, there are still many uncertainties and question marks. In the 2008 ASPERA <sup>1</sup> Road Map document “The European Strategy in Astroparticle Physics” (updated in 2011) the investigation of the high-energy Universe by studying CRs addressed by one of the six basic questions, finding the answer to which has the priority in the research in Europe in the next 10 to 15 years. The question reads: “What is the origin of cosmic rays? What is the view of the sky at extreme energies?” The other five topics cover search for dark matter, gravitational waves, proton life-time and investigations of neutrino properties.

These question marks exist not only at highest energies, but also in the range covered by KASCADE-Grande, i.e.  $10^{16}$  eV– $10^{18}$  eV. The actual shape of the energy spectrum and the primary mass composition there is a hot topic of scientific investigations and discussions.

In the CR research with EAS technique it is important to measure and analyze as many of the shower parameters as possible, what allows to cross-check the obtained results of shower properties and the validity of hadronic interaction models (a key aspect in CR research, as it will be shown in the following). The KASCADE EAS experiment, a predecessor of KASCADE-Grande, was therefore supplemented with a large streamer-tube Muon Tracking Detector (MTD) in order to investigate shower properties with the muon tracking technique, in addition to the standard investigation with the scintillator array.

The investigation of the EAS longitudinal development, using the tracks of shower muons registered in the MTD, in order to contribute to the development of hadronic interaction models and to the determination of primary mass composition was the goal of the presented work.

In Chapter 1 basic elements of cosmic ray physics in the KASCADE-Grande range of energies are introduced. The energy spectrum of cosmic rays and its features are described. A short characteristics of models that can explain the shape of the spectrum is presented. General features of extensive air showers are discussed and methods of their detection are shortly introduced.

In Chapter 2 extensive air shower simulations in context of KASCADE-Grande experiment are introduced. A short description of high energy hadronic interaction models used in EAS simulations in KASCADE-Grande

---

<sup>1</sup>ASTroParticle ERA net – a network of national government agencies responsible for coordinating and funding national research efforts in Astroparticle Physics within the European Research Area (ERA) net scheme of the European Commission.

is presented.

Chapter 3 contains the description of the KASCADE-Grande EAS experiment. A short characteristics of each component is given. The procedures used to reconstruct air shower parameters and obtained reconstruction quality are presented.

Chapter 4 is devoted to the detailed description of the Muon Tracking Detector. Its design, operation and procedure of track reconstruction is presented.

In Chapter 5 selection of showers and muon tracks is described. General criteria used in selection of showers and muon tracks applied to measured and simulated data are given.

The following chapters contain results of the investigation of : the lateral muon density distributions (6), pseudorapidity of EAS muons and its sensitivity to the primary CR mass composition (7 and 8), and muon production height (9). In each chapter the details of the analysis are presented (shower and muon track selection), followed by results and conclusions.

The results of the thesis are summarised in chapter 10.

Appendices contain additional information and analysis results discussed in chapters from 5 to 9.

# Chapter 1

## Cosmic rays and Extensive Air Showers

Energetic cosmic ray particles entering the Earth atmosphere and initiating there a cascade of photons, leptons, muons and hadrons are called *primary CR particles*. All the other are *secondaries*. The properties of the *primaries* carry the astrophysical and cosmological information. They are indirectly inferred from the precise measurements of *secondaries* and involved theoretical assumptions on the development of shower cascades. The observations of *secondaries* in EAS, at the same time, allow to test and improve hadronic interaction models describing this cascade development.

### 1.1 The primary energy spectrum of cosmic rays

The CR spectrum extends over wide range of energies, exceeding  $10^{20}$  eV, an energy larger by several orders of magnitude than the energies available in the current and future accelerators. The flux changes from  $\approx 1000$  particles per  $\text{m}^2$  per second at  $10^9$  eV to  $\approx 1$  particle per  $\text{km}^2$  per century at the highest energies. The spectrum can be described by a simple power law:

$$dI/dE \sim E^{-\gamma} \tag{1.1.1}$$

In Fig. 1.1.1 a differential cosmic ray all-particle spectrum multiplied by  $E^{2.5}$ , as measured by the indicated EAS experiments, is shown. One can distinguish there several features. First, the spectral index  $\gamma$  changes from 2.7 to 3.1 at the energy  $\approx 4 \times 10^{15}$  eV forming a structure, known as the *Knee*. Just recently first analysis of KASCADE-Grande data [3] resulted in a knee-like feature at around  $8 \times 10^{16}$  eV caused by steepening in the spectrum of heavy primary cosmic rays by  $\Delta\gamma \approx -0.2$ , known as the *Iron Knee*. In the transition region from galactic to extragalactic origin of cosmic rays a small kink in the spectrum at around  $5 - 7 \times 10^{17}$  eV, as indicated by observations by Akeno [4] and HiRes [5] and named as *Second Knee* [6, 7].

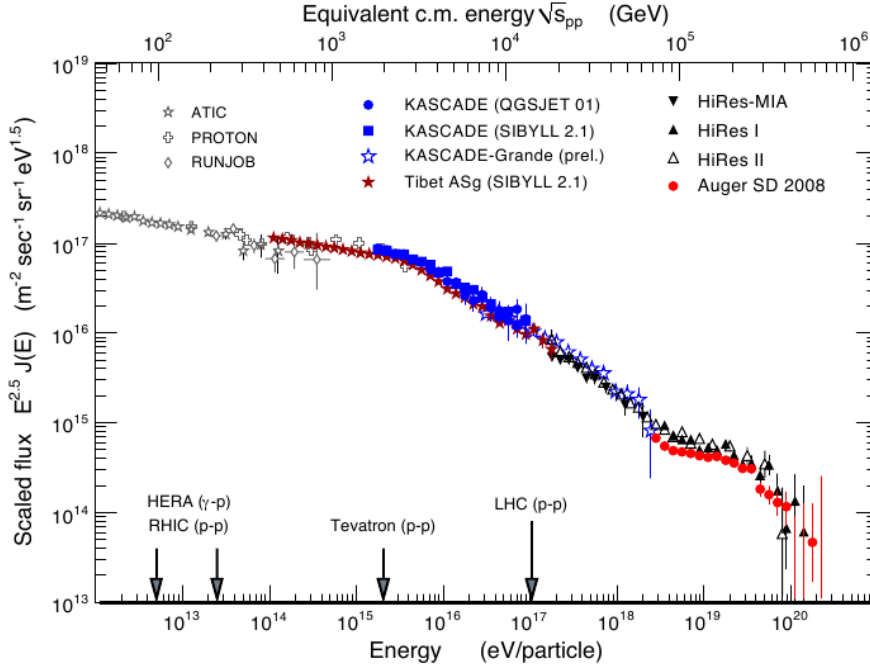


Figure 1.1.1: All-particle differential cosmic ray energy spectrum.

Then, at about  $5 \times 10^{18}$  eV a flattening of the spectrum is observed with the index back to  $\approx 2.7$ , known as the *Ankle*. At around  $5 \times 10^{19}$  eV a rapid cut-off of the spectrum begins, predicted by Greisen-Zatsepin-Kuz'min [8,9] (*GZK cut-off*) resulting in a very scarce population of the events in the region above  $10^{20}$  eV.

The main features of the CR spectrum are described by the *Standard Model of Cosmic Rays* [10]. The CR originate in the explosions of supernovae. In our Galaxy there are on average three such explosions per century. To explain the observed cosmic ray flux only a few percent of the energy generated in the explosion is necessary.

The fundamental process that explains how particles are accelerated is called the Fermi acceleration. In 1949 [11] Fermi has shown that charge particles gain energy by multiple reflections from the “magnetic mirrors”, being moving interstellar magnetized clouds. The gain in energy is proportional to the cloud velocity squared, hence, this process is now called *second-order Fermi acceleration*.

In 1977 [12], it was shown that Fermi acceleration by supernova remnant shocks, *the diffusive shock acceleration*, is particularly efficient. In a shock front the two regions with different characteristic of magnetic field are created. A particle of matter may traverse a shock front several times. When the particle is reflected at either side by a diffusive scattering it gains energy proportional to the speed of the shock wave, therefore this process

is called *first-order Fermi acceleration*. Both acceleration mechanisms lead to a resulting power-law energy spectrum with the index around  $\gamma=2$ . During propagation the energy of CR particles changes in various energy-loss processes, collisions and decays. This is the reason why the spectral index observed at Earth is not  $\gamma=2$  but  $\gamma=2.7$ .

The termination shocks of stellar or galactic wind are the other cosmic sources which exhibit shock fronts [13,14]. Also interaction between a pulsar and the atmosphere of the companion star in binary systems may exhibit shock fronts [15]. It has been estimated that the mentioned objects are able to accelerate cosmic rays up to  $10^{16}$  eV and are contributing to the *galactic* component of CR. Higher energies can be achieved when particles interact with shock fronts in relativistic jets from Active Galactic Nuclei (AGN, [16]), giant supernovae or polar caps of fast rotating pulsars. Some of these objects are considered as possible sources of *extragalactic* CR.

The Knee feature was first discovered in EAS measurements in 1958 [19] and became a matter of many-decades-long research. Only 50 years later it was found that the Knee in the cosmic ray spectrum is caused by the steepening of the spectra of light primaries [17] (Fig. 1.1.2, top panel). Simultaneously, the KASCADE experiment has shown the individual mass groups spectra [18] with a decrease of flux in the Hydrogen and Helium spectra in the Knee region (Fig. 1.1.2, bottom panel). There are several models interpreting this behaviour.

- One group of models gives an *astrophysical* explanation and relates the Knee to the *rigidity* dependent properties of the magnetic confinement of CR particles. Energy gained by the particles during acceleration process is limited and proportional to the charge of the element. In addition, particle Larmor radius (proportional to particle energy and inversely to charge  $Z$ ) becomes larger than the thickness of the galactic disk, they start to escape from the Galaxy. The Knee position is then *rigidity* dependent [17,18].
- *Particle physics* type explanations introduce new interaction mechanisms, not considered by the hadronic interaction models in the development of EAS, like new interaction channels and/or creation of new heavy particles, see [20,21]. A predicted consequence of those models is that the position of the Knee should be mass number  $A$  dependent (not charge  $Z$  dependent).
- A single, near and relatively young supernova remnant could be responsible for the shape of the spectrum around the Knee. Particles accelerated in its shock wave are superimposed on a featureless cosmic ray background from several distant sources [22].

Observation of the Iron Knee [3] favours the rigidity dependent Knee resulting both from reaching the maximum energy of the galactic CR accelerators and the leakage from the Galaxy during the CR propagation to the Earth [23].

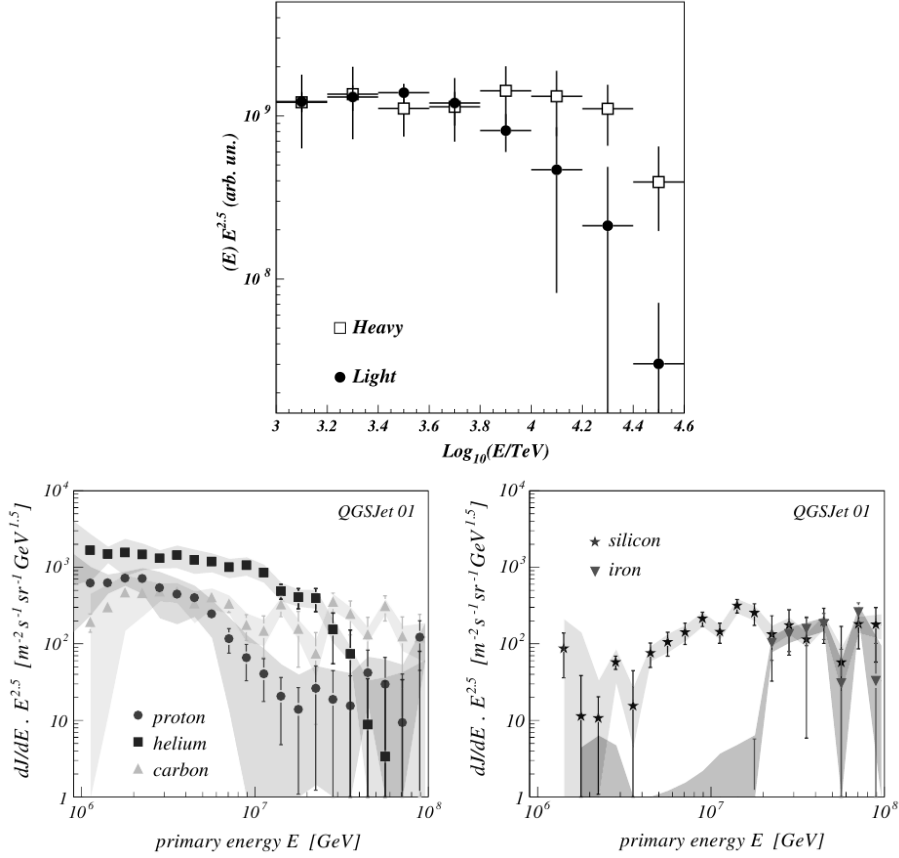


Figure 1.1.2: **Top panel:** the cosmic ray energy spectrum measured by EAS-TOP and Macro for the light and heavy primaries separately [17]. The break in the spectrum of light primaries is visible at the Knee energy. **Bottom panels:** the cosmic ray energy spectrum of different primary mass groups obtained at KASCADE with the unfolding method [18].

The shape of the cosmic ray spectrum above the Knee can be interpreted by increasing contribution of particles reaching Earth from outside of our Galaxy. Currently, two models are being investigated:

- According to the “Dip model” by Berezhinsky et al. [24] the galactic component breaks down around  $10^{17}$  eV and extragalactic component containing protons becomes dominant at  $\approx 10^{18}$  eV. Protons are accelerated by relativistic jets (like in AGNs). The observed Ankle is caused by the interaction of protons with the cosmic microwave background (CMB).
- The “Hillas model” [25] predicts that the galactic component extends up to  $10^{18}$  eV and the transition to extragalactic component occurs at the Ankle. He proposed in addition to the standard SNR component, a *component B* of cosmic rays of galactic origin. This component would

also experience a charge dependence of break-offs, but now shifted to approximately ten times higher energy. As a result, the transition occurs at the Ankle and the Second Knee would be a feature of component B. In this approach the mixed composition of cosmic rays should be seen up to  $E \approx 10^{18}$  eV.

The cut-off present at the high-energy end in the particle spectrum, and now confirmed by Pierre Auger Observatory [26], is interpreted as a strong suppression of cosmic ray flux due to the production of pions in the interaction of particles with CMB (GZK cut-off) or by reaching an upper energy limit in the accelerating sources.

## 1.2 The mass composition of cosmic rays

Direct measurements of CR particles up to energy  $10^{14}$  eV revealed their mass composition. They consist of about 98% of hadrons and 2% of electrons and photons. The hadronic component is composed of 87% protons and 12% helium nuclei. The rest consists of fully ionized nuclei of heavier elements. The relative abundance of the elements in CR and solar system normalized to silicon is presented in Fig. 1.2.1. All elements present in cosmic rays are also present in the solar system. This suggests that CR are ordinary matter being produced by nucleosynthesis in stars and accelerated to high energies.

Cosmic rays contain less H and He than the solar system, which sug-

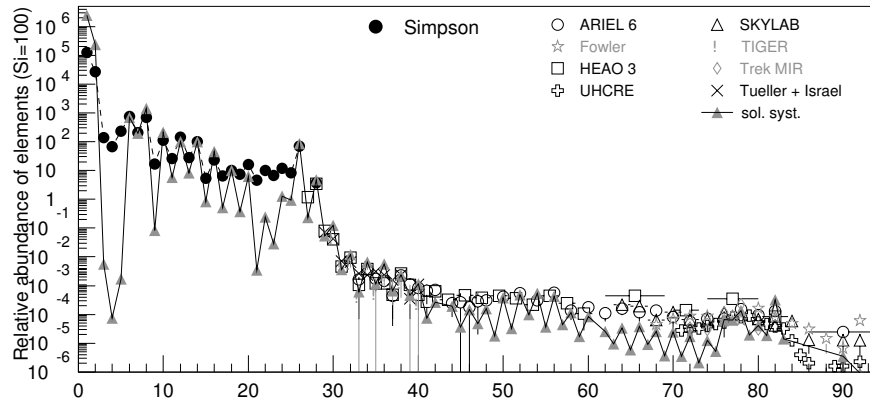


Figure 1.2.1: Abundance of elements in cosmic rays as function of their nuclear charge number  $Z$  at energies around 1 GeV/n, normalized to Si = 100 [27]. Abundance for nuclei with  $Z \leq 28$  according to Ref. [28]. Heavy nuclei as measured by ARIEL 6 , HEAO 3 , SKYLAB , TIGER , TREK/MIR , as well as UHCRE . In addition, the abundance of elements in the solar system is shown according to Ref. [29]. From Ref. [23].

gests that relatively small amount of these elements (compared with their estimated total abundance) is being ionized and accelerated in the place of origin.

Two groups of elements are more abundant in cosmic rays than in solar system: Li, Be, B and Sc, Ti, V, Cr, Mn. This can be explained with the spallation processes during propagation of the CNO group at lower masses and of Fe at higher masses.

Above  $10^{14}$  eV the direct detection of CR is not possible because of the low flux. That is why large detector arrays have been built all over the world to study the CR using the phenomenon called *extensive air showers* (EAS). Reconstruction of the shower parameters allows to study the CR mass composition either by relative abundances of several mass groups [18] or via the quantity called the *mean logarithmic mass*  $\langle \ln A \rangle$ . The  $\langle \ln A \rangle$  of the CR particles can be estimated either from EAS electrons, muons and hadrons at the observation level (Fig. 1.2.2) or measurements of the shower maximum  $X_{max}$  (Fig. 1.2.3).

There is large discrepancy in behaviour of the  $\langle \ln A \rangle$  derived from the average  $X_{max}$  and from measurements of electrons, muons and hadrons. In Fig. 1.2.3 the  $\langle \ln A \rangle$  is decreasing up to the energy  $4 \times 10^{15}$  eV and then above  $3 \times 10^{16}$  eV. In the intermediate energy range the  $\langle \ln A \rangle$  is increasing with energy. This is not consistent with the behaviour of the  $\langle \ln A \rangle$  derived from particle detector measurements (Fig. 1.2.2).

As further studies show (see [30, 31]), interpretation of the data with other commonly used models of high energy hadronic interactions (QGSJetII, SIBYLL) do not change the situation qualitatively. Observed discrepancies can be reduced by introducing modifications (in case of QGSJet01 model: reduction of the inelastic cross section and/or increasing values of the elasticity of hadronic interactions).

In the next chapters of this thesis it will be shown that pseudorapidity of EAS muons calculated from muon direction with respect to the shower axis is a mass sensitive parameter and can be used to estimate the mean logarithmic mass. In KASCADE-Grande experiment muon directions are reconstructed with the Muon Tracking Detector with high accuracy. The muonic component of EAS will be described in the next section. Here it is important to point out that the muons carry information about high energy interactions and development of the shower in the atmosphere, thus muon tracking provides a cross-check of the results obtained with the charged particle detector arrays.

### 1.3 Extensive Air Showers

When CR particles reach the Earth's atmosphere they interact with its constituents, mainly with Nitrogen and Oxygen nuclei. This leads to multiple production of secondary particles: mesons, baryons, hyperons, nuclei fragments, etc. Secondaries with enough energy will continue their path through the atmosphere and interact further, producing mainly pions and

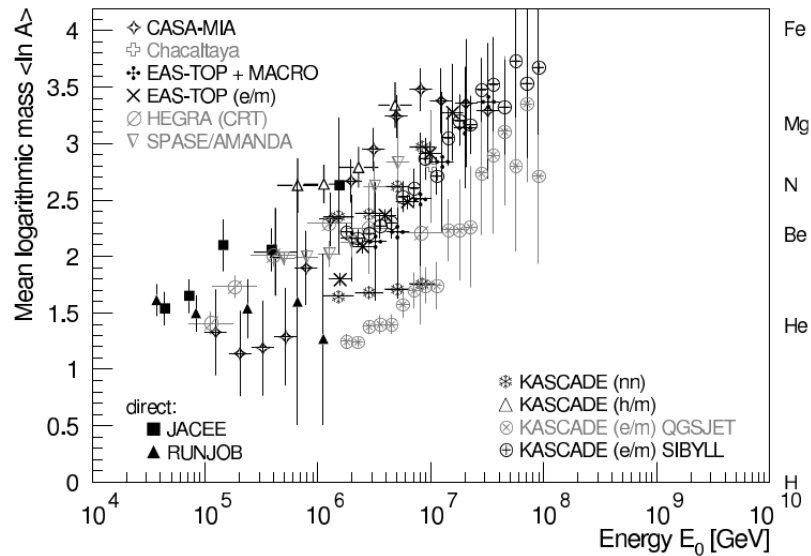


Figure 1.2.2: Mean logarithmic mass of cosmic rays derived from the measurements of electrons, muons, and hadrons at ground level. The hadronic interaction models QGSJET 01 and SIBYLL are used to interpret the measurements. From Ref. [23].

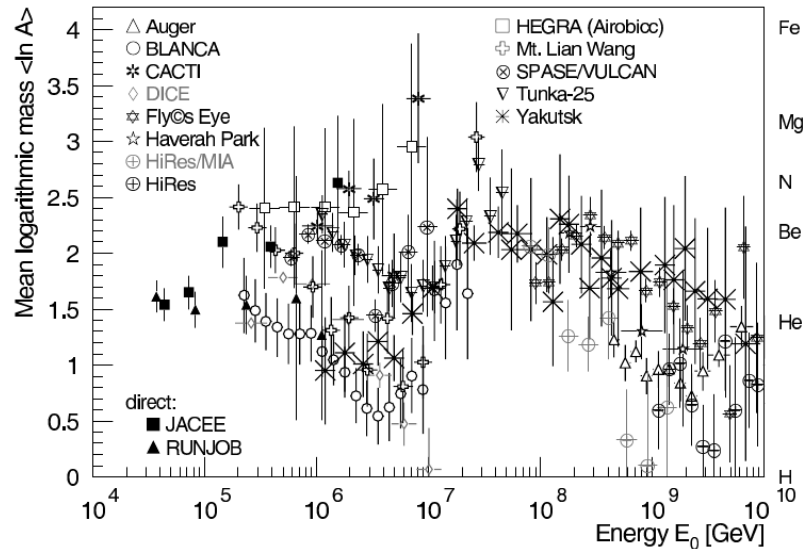


Figure 1.2.3: Mean logarithmic mass of cosmic rays derived from the average depth of the shower maximum. The hadronic interaction model QGSJET 01 is used to interpret the measurements. From Ref. [23].

kaons. New particles in the cascade are being produced as long as the average energy per particle is above the specific energy threshold for production. After reaching a maximum in the development, the number of particles in a shower is decreasing and constituents of the cascade lose their energy.

One can distinguish three main components of an extensive air shower: hadronic, electromagnetic and muonic. General scheme of EAS development is shown in Fig. 1.3.1. The hadronic component feeds the muonic and electromagnetic components.

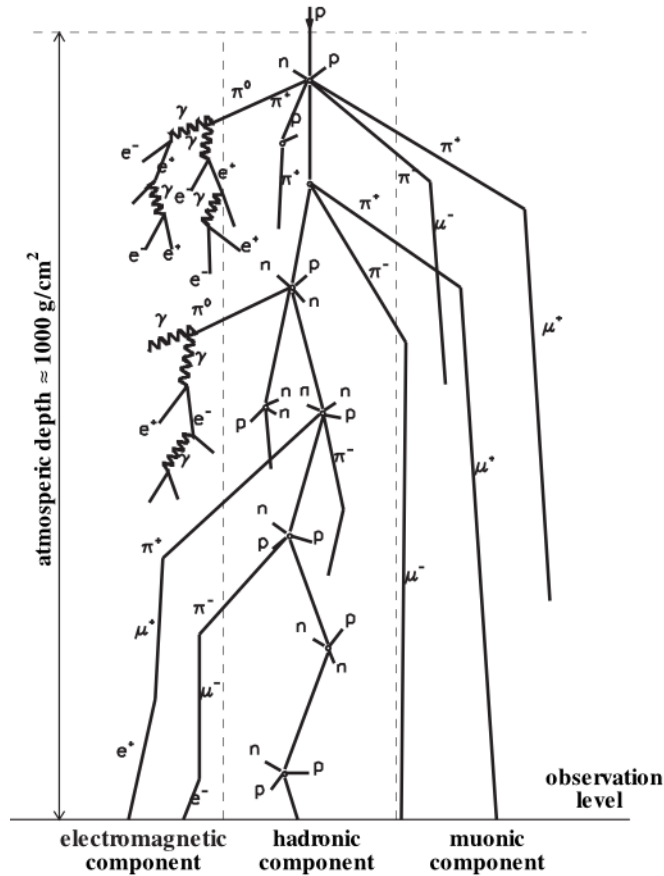


Figure 1.3.1: General overview of EAS components.

### 1.3.1 The hadronic component

Cosmic ray particles collide with constituents of the Earth's atmosphere, mainly with Nitrogen and Oxygen nuclei, after travelling a depth  $\lambda$ , with a probability:

$$P(\lambda) = 1/\lambda_{int} e^{(-\lambda/\lambda_{int})} \quad (1.3.1)$$

where,  $\lambda_{int} = A/(N\sigma(E))$  is a mean free path ( $\approx 90 \text{ g/cm}^2$  for proton),  $A$  is a mass number,  $N$  is Avogadro constant and  $\sigma(E)$  is a cross section.

In case of a proton with energy  $\approx 10^{15} \text{ eV}$ , the first interaction takes place, on average, at  $\approx 20 \text{ km}$  above sea level, but some particles can reach even  $10 \text{ km}$  deeper before the first collision. In case of heavy cosmic ray

nuclei, like Iron, the first interaction takes place, on average, higher in the atmosphere, because the cross-section for the interaction is larger.

The secondary hadrons produced in the first interaction (mainly neutral and charged pions, kaons, baryons like protons and neutrons, and nuclear fragments) that live long enough to undergo further interaction are a source of new generation of secondaries. The consecutive interactions take place creating a hadronic cascade. The number of hadrons increases with atmospheric depth, reaches its maximum and then decreases exponentially. The atmosphere provides an average thickness of 11 hadronic interaction lengths.

The secondary hadrons have relatively low mean transverse momenta, of about 400 MeV/c, therefore, highly energetic hadrons create a shower core of a radius of about 20 meters (called the shower axis) that propagates along the direction of the primary particle.

The hadronic component being a source of other shower components constitutes on ground about 1% of the total number of all secondary particles.

### 1.3.2 The electromagnetic component

The decay of the neutral pions contributes mostly to the electromagnetic component of the shower. Neutral pions decay predominantly into two photons. Those photons have enough energy to create electrons and positrons via pair production. Created leptons lose their energy via bremsstrahlung process, creating photons. These two processes alternate leading to the development of the electromagnetic cascades that develop as long as the energies of the photons have large enough energy for pair production and the probability of bremsstrahlung process is higher than the probability of ionization losses for electrons.

The longitudinal development of the cascade induced by the photon of energy  $E_0$  can be described by [32] :

$$N_e(E_0, t) = \frac{0.31}{\sqrt{\beta_0}} \exp \left[ t \left( 1 - \frac{3}{2} \lg(s) \right) \right] \quad (1.3.2)$$

where  $\beta_0 = \lg(E_0/E_c)$ ,  $t$  is atmospheric depth,  $s = 3t/(t+2\beta_0)$  is the shower *age*. At the maximum of the shower development  $s=1$ . Before the maximum  $s<1$ , and after  $s>1$ . A critical energy  $E_c$  is the energy at which the energy loss rates due to ionization and due to bremsstrahlung are equal.

Created neutral pions feed the electromagnetic cascades with new particles. That is why the number of electrons, positrons and photons in the shower grows rapidly making this component the most numerous in the shower. The lateral spread is dominated by the multiple Coulomb scattering of the electrons that is characterized by Moliere radius  $r_M$ , being equal to 9.5 g/cm<sup>2</sup> ( $\sim 100$  meters at sea level) for electrons in air.

The lateral distribution function for a pure electromagnetic cascade in a homogeneous atmosphere is well described by the Nishimura-Kamata Greisen (NKG) formula [33]:

$$\rho(r) = C(s) \left( \frac{N_e}{r_M^2} \right) \left( \frac{r}{r_M} \right)^{s-2} \left( \frac{r}{r_M} + 1 \right)^{s-4.5} \quad (1.3.3)$$

where shower age  $0 < s < 2$  and  $C(s)$  is a normalization constant.

It is important to mention three additional components related to the electromagnetic cascade of the shower:

- fluorescent light that is emitted isotropically by the nitrogen atoms (in the wavelength of 300-430 nm range) being excited by EAS electrons;
- Cherenkov light, emitted in a narrow cone around the trajectory of the ionizing particle (mostly electron or positron) that is travelling with a speed greater than speed of light in air;
- coherent geo-synchrotron radiation (in the radio-frequency band) that is emitted by the electrons and positrons propagating in the Earth magnetic field.

### 1.3.3 The muonic component

The muonic component stems from decays of pions and kaons:

$$\begin{aligned} \pi^\pm &\rightarrow \mu^\pm + \nu_\mu(\bar{\nu}_\mu) \quad (\approx 99.99\%) \\ K^\pm &\rightarrow \mu^\pm + \nu_\mu(\bar{\nu}_\mu) \quad (\approx 63.5\%) \\ K^\pm &\rightarrow \pi^0 + \mu^\pm + \nu_\mu(\bar{\nu}_\mu) \quad (\approx 3.2\%) \\ K_L^0 &\rightarrow \pi^\pm + \mu^\pm + \nu_\mu(\bar{\nu}_\mu) \quad (\approx 3.2\%) \end{aligned}$$

High energy mesons not only can decay but also can strongly interact with constituents of the atmosphere. The competition between the two processes depends on the lifetime and energy of mesons, as well as the density of the medium. At constant density the probability of interaction is rising with increasing energy and chance of decay is reduced by the time dilatation. This trend is amplified with increasing density of the medium in which particles propagate.

The most energetic muons ( $E > 100$  GeV), that originate from the early stage of EAS development can travel in straight lines from the place of origin to the observation level and lose energy ( $\sim 1\%$ ) mainly through ionization process. Those particles do not spread significantly because the scattering is strongly suppressed compared to electrons. Low energy muons created

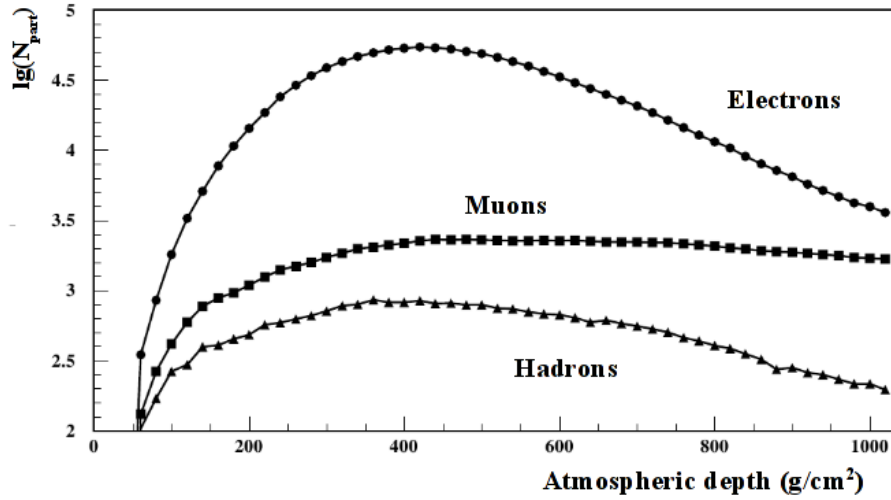


Figure 1.3.2: Longitudinal profile of the hadronic, electromagnetic and muonic component of the shower development. Primary particle was a proton with energy  $10^{14}$  eV. Number of electrons with energies down to 3 MeV and muons and hadrons down to 300 MeV as a function of atmospheric depth is presented [34].

in the late stage of the development of the cascade have a large chance to decay before reaching the observation level.

$$\mu^\pm \rightarrow e^\pm + \bar{\nu}_\mu(\nu_\mu) + \nu_e(\bar{\nu}_e)$$

### 1.3.4 Development of EAS for different primaries

The basic shower development can be described with lateral and longitudinal distributions. The way the number of secondaries changes as a function of the atmospheric depth is reflected in the longitudinal development of an air shower, while the lateral distribution describes the particle densities as a function of the distance from the shower axis. These descriptions show different features of the shower, depending on the primary cosmic ray particle mass  $A$  and energy  $E_0$ .

Figure 1.3.2 shows an example of longitudinal development of all three components of the shower that developed from interaction of  $10^{14}$  eV proton with air. As it was explained in previous section the number of electrons and hadrons is decreasing fast after reaching the atmospheric depth of maximum development of the component (here  $\sim 450$  g/cm<sup>2</sup> for electrons and  $\sim 350$  g/cm<sup>2</sup> for hadrons). The number of muons is not changing significantly.

The iron primary has greater chance to interact higher in the atmosphere than proton (see chapter 1.3.1). As a consequence: all three components of EAS are developing higher for iron than for proton primary. This is reflected in the lateral and longitudinal distributions of electrons shown in Fig. 1.3.3a

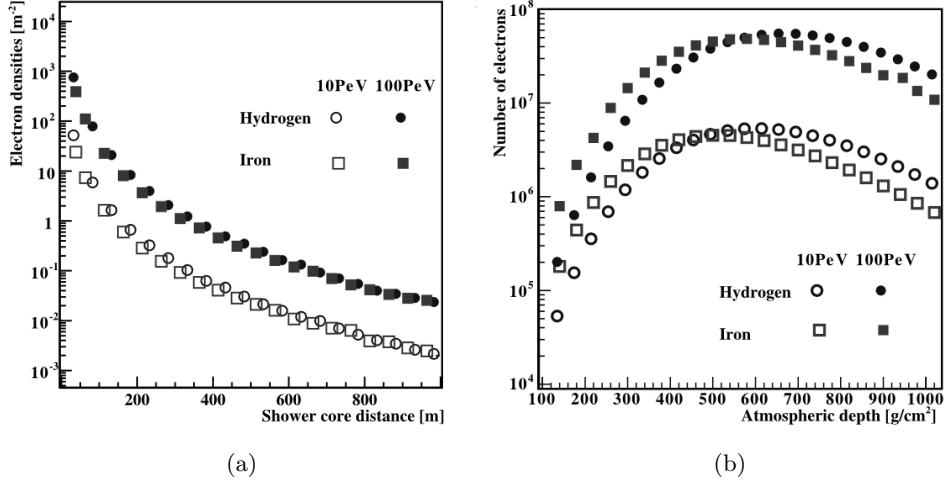


Figure 1.3.3: Average lateral (a) and longitudinal (b) distributions for electrons of 50 simulated air showers for different energies and primaries [35].

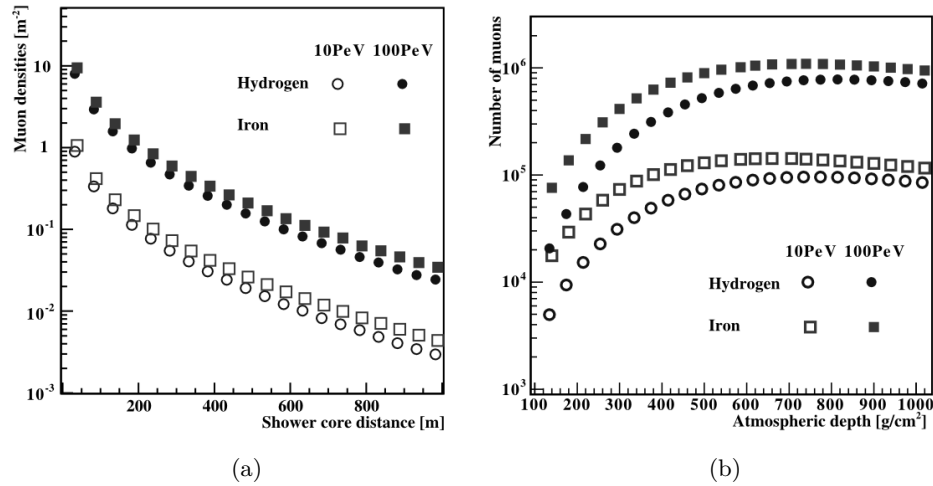


Figure 1.3.4: Average lateral (panel a) and longitudinal (panel b) distribution for muons of 50 simulated air showers for different energies and primaries [35].

and 1.3.3b, and of muons in Fig. 1.3.4a and 1.3.4b. The distributions are shown for the two types of CR primary and two energies.

At a given energy, the maximum number of electrons and muons is reached at lower atmospheric depth for iron than for proton primary (see Fig. 1.3.3b and 1.3.4b). After reaching its maximum the number of particles is decreasing. The electromagnetic cascade dies out faster because of the larger content of low energy particles. The content of muons is decreasing slowly due to energy loss for scattering and consecutive decay. The num-

bers of particles at atmospheric depth of  $1000 \text{ g/cm}^2$  (significant for analysis in the KASCADE-Grande experiment) depend on the cosmic ray primary type. For iron initiated showers the number of electrons is smaller than for proton primary while the number of muons is larger. This behaviour of muonic and electromagnetic component helps to distinguish between iron and proton initiated showers.

At a given observation level, the differences in EAS development are reflected in differences in the lateral density distributions of electrons and muons (Fig. 1.3.3a and 1.3.4a). The proton showers develop deeper in the atmosphere and more electrons can reach the observation level. Electrons from iron showers have to travel longer distance in the atmosphere, thus the electron densities are smaller up to 400 meters. At larger distances, densities for iron and proton are similar. The muon component develops differently than the electromagnetic. The iron showers create more muons than proton ones and more of them can reach the observation level, thus densities from iron showers are larger than from proton initiated showers.

## 1.4 EAS detection techniques

To detect particle components of EAS various types of detectors are used: plastic and liquid scintillators, streamer tubes, multi-wire proportional chambers and water Cherenkov detectors.

In scintillators, a specific fraction of incident energy carried by striking particles is absorbed and transformed into detectable photons that can be converted to electric signals, e.g., by photomultipliers.

Streamer tubes and multi-wire proportional chambers are types of gas detectors. The chamber is filled with a gas mixture and certain electric field is created by applying high voltage. When ionizing particle is passing through the volume of the chamber ion-electron pairs are being created. The ions and electrons drift then under the applied electric field to the electrodes where they are collected. The gas detector can operate in various modes that are depending on gas mixture and applied high voltage.

In water Cherenkov detector ionizing particles, travelling with a speed larger than the speed of light in water, are a source of radiation emitted in a narrow cone around the direction of propagation. This *Cherenkov light* can be detected with photomultipliers. Depending on the geometry of the detector it is possible to detect and distinguish between electrons and muons.

### 1.4.1 Arrays of particle detectors

As already mentioned the flux of cosmic rays decreases with energy very fast and above  $10^{14}$  eV direct measurements are not possible. The most efficient method of investigation of cosmic rays above this energy is to study EAS

with arrays of particle detectors. Such an array can occupy an area from a few hundred square meters to thousands of square kilometers. The size determines the upper limit of detectable primary energies, which can exceed  $10^{20}$  eV.

Various types of particle detectors can be used in different organization schemes. The most popular are single particle detectors, with or without shielding, made of scintillators or water Cherenkov tanks, particle telescopes under a shielding and calorimeters.

Experiments built as arrays of particle detectors have many advantages over other organization schemes. They are relatively easy and cheap to build, rebuild and extend to any size, providing the space and resources are available. When equipped with dedicated detectors they can detect all three particle components of EAS with high accuracy. The arrays can operate for a long time, day and night, and are moderately sensitive to weather conditions. They can collect data even if part of the array is not working correctly or is damaged. Also, the location of the array is not crucial for its operation or data analysis, but it has to be noted that an array built at a certain height above the sea level detects showers that are in a certain stage of their development.

There are many experiments which were built according to this scheme, like Haverah Park [36], AGASA [37], EAT- TOP [38], KASCADE [39] and KASCADE-Grande [40].

### 1.4.2 Fluorescent light detectors

The air shower develops an electromagnetic cascade which is a source of the fluorescent radiation. This radiation is detected with telescope - like detector: the light is reflected from mirrors and hits a camera, made out of photomultipliers.

This technique is efficient for showers that stem from cosmic rays with energy above  $10^{17}$  eV because such showers can produce enough photons available for detection.

Today, it is common to use arrays of fluorescent telescopes that are viewing the same volume of the atmosphere where an EAS develops. With the multi-telescope setup it is possible to estimate the energy and direction of the shower with high accuracy.

A big advantage of the fluorescent detector technique over arrays of particle detectors is that it allows to obtain longitudinal profile of a shower (Fig. 1.4.1). In the shower profile most important features of the cosmic ray particle are reflected: its type, energy and arrival direction. These parameters can be used to answer the most important questions about the cosmic rays: their composition, energy and sources. Thanks to the development in space science, it was possible to design fluorescent telescope that can operate

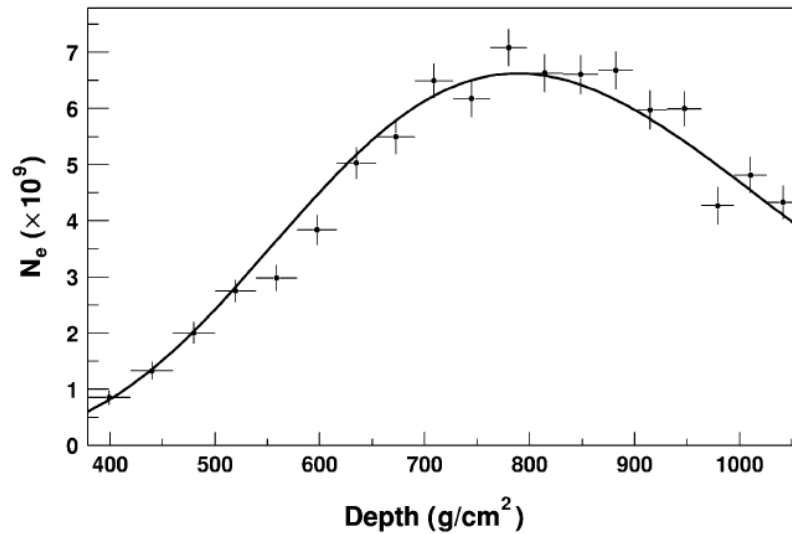


Figure 1.4.1: Longitudinal profile of the  $\sim 10^{19}$  eV shower as seen by the Pierre Auger Observatory fluorescence detector [41].

above the atmosphere of the Earth. The telescope in JEM-EUSO [42, 43] experiment will be mounted on the International Space Station and will be able to detect inclined showers of the highest energies.

Detection of air showers with these detectors has its limitations. Telescopes can operate only at moonless nights and perfect weather condition. Dust and light pollution created by human activity also limits the possible locations of such detectors. The fluorescent emission can be detected up to a certain angle with respect to the shower axis. Radiation close to the shower axis is dominated by Cherenkov emission that is considered as a pollution and should be corrected for in a multi-telescope setup. That is why not all showers are a source of valuable information. All of the described factors limit the duty cycle to 10%.

### 1.4.3 Air Cherenkov light detectors

The air Cherenkov light detectors are very similar in construction and operation to the fluorescent light detectors. The only difference is that they detect Cherenkov light coming from the shower axis. This technique occurs to be specially useful in high energy gamma-ray astronomy but it is also possible to study air showers with it. Arrays of Cherenkov light telescopes provide information about total energy released by the cascade and position of the shower axis. This technique has similar limitations as fluorescent light detection. An example of EAS experiment using this technique is HEGRA [44].

#### 1.4.4 Radio-emission detectors

The coherent radio emission that is accompanying EAS cascade originates from electrons and positrons bent in Earth's magnetic field. This was confirmed by LOPES [45] and CODALEMA [46] experiments.

Currently, detection of radio emission for the purpose of EAS studies is being developed in KASCADE-Grande (LOPES) and PAO (AERA [47]) experiments. Various types of antennas and in various configurations are being tested to develop a low cost, self-triggering system which is able to deliver precise information about the most energetic showers. Detection of geo-synchrotron emission is efficient for showers above  $10^{17}$  eV.

The array of radio antennas can operate for long periods of time, 24 hours per day and, as in case of arrays of particle detectors, it is little sensitive to weather conditions or malfunction/damage of a part of the array.

#### 1.4.5 Hybrid detector systems

Development of the all mentioned above detection techniques and detectors made it possible to combine different detectors into one EAS experiment. A good example of such a setup is Pierre Auger Observatory [41], where an array of water Cherenkov tanks is combined with four stations of fluorescent light telescopes. The hybrid technique provides valuable information about shower development on many levels and allows to cross-check hadronic interaction models that are used to understand what is measured in particle detector arrays.

The cross-check and cross-calibration between different components of the experimental setup is a useful tool for checking and correcting for systematic errors in measurements.

## Chapter 2

# Simulations of EAS

To draw specific conclusions about cosmic rays from their indirect investigation it is very important to know how they interact with the atmosphere and how the EAS develops. This knowledge is obtained by means of computer Monte Carlo simulations. The details of the high-energy interaction models are not known at energies and kinematic region that are most valid for the evolution of the particle cascade and their parameters must be extrapolated within assumptions of the model. Interaction of the primary cosmic ray particle and their secondaries are described by the high- and low-energy hadronic interaction models. The information about particles in the cascade is stored and can be compared with the measurement from the experiment.

Comparing features of the simulated showers with the measurements it is possible to estimate the mass composition and energy of the primary particle from the measured data and to test the quality of the hadronic interaction models at energies not available in the man-made colliders.

In this chapter a short overview of the Monte Carlo EAS simulations with CORSIKA [48] code and model testing in context of KASCADE-Grande experiment is given. Short characteristics of the commonly used high-energy interaction models are included at the end of the chapter.

### 2.1 The purpose of the EAS simulations

The arrays of particle detectors, like KASCADE-Grande experiment, measure energy deposits from EAS particles above defined energy threshold at a certain distance range from the shower core, and arrival time at the observation level. The results from many showers deliver information about average parameters of the detected showers.

To derive from this data information about the mass composition and energy of the cosmic rays it is essential to know how the air showers develop in the atmosphere and the ranges of their characteristic parameters at the observation level.

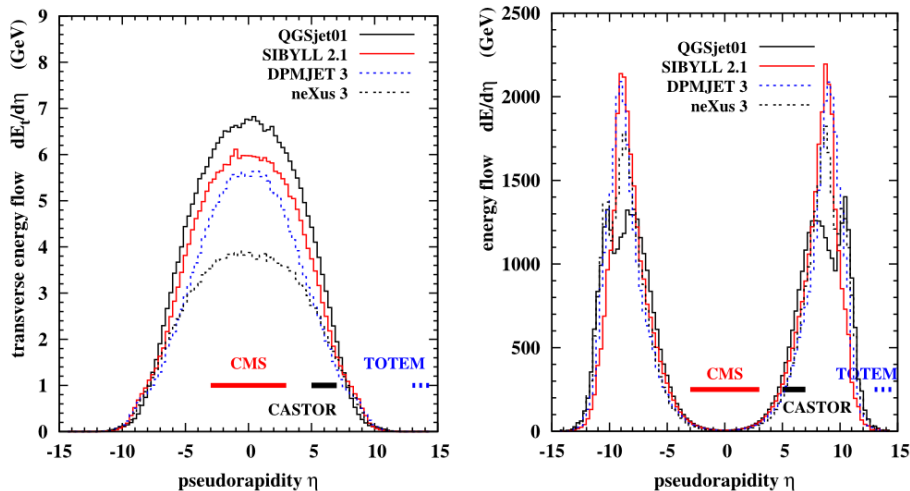


Figure 2.1.1: Predicted energy flow at LHC. Model predictions are compared with the acceptance of the central CMS and the forward CASTOR [49] and TOTEM detectors. The **left hand panel** shows the transverse energy flow which is the typical quantity measured in high energy physics experiments. The **right hand panel** shows the total energy flow which is the quantity of direct relevant to air shower simulations. From Ref. [50].

The evolution of the electromagnetic shower is well described by quantum electrodynamics up to the highest energies, but the most important processes, being a driving force of EAS development, the high-energy hadronic interactions, are still not well known. To describe the development of the air shower it is necessary to treat hadronic collisions on a general ground to minimize the bias, predict the inelastic hadron-nucleon interaction cross-section and energy lost for production of secondary particles (inelasticity). The interaction parameters are extrapolated from the results of collider experiments where the energies are many orders of magnitude smaller than those in EAS and from low to high rapidity  $y$  region (typically  $y \lesssim 5$  in colliders and  $y > 5$  in EAS, see Fig. 2.1.1).

On the other hand, the details of hadronic final states like production of short-lived resonances, contribution of high  $p_{\perp}$  hadrons or particles with small inclusive cross-sections have negligible influence on lateral or longitudinal development of the shower.

In collider experiments various types of particles and ions interact with each other ( $p\bar{p}$ ,  $pp$ ,  $pA$ ,  $ion-ion$ ) in a stable environment at cms energies from a few hundred GeV (RHIC) to 14 TeV (LHC, to be achieved) per nucleon, which corresponds to laboratory energy range from  $\sim 10^{13}$  eV to  $10^{17}$  eV.

At the LHC experiments for the first time the forward region of the high-energy interaction will be available from the measurement in LHC-forward (LHCf), TOTAl Elastic and diffractive cross section Measurement (TOTEM) and Zero Degree Calorimeter (ZDC) detectors.

The LHCf experiment is designed to measure energy and transverse momentum spectra of gamma-rays and neutral hadrons in pseudorapidity range  $\eta > 8.4$  up to an energy of 7 TeV. The design of this experiment is described in [51], and preliminary results are in Ref. [52].

Figure 2.1.1 shows an example of predictions of pseudorapidity distribution of secondary particles in  $pp$  collisions in LHC. The transverse energy flow and the total energy flow in inelastic proton-proton collisions at LHC with the CMS, CASTOR [49], and TOTEM [53] detector acceptance ranges are compared. Only the dedicated LHCf experiment will fully cover the pseudorapidity range of interest to EAS physics.

The TOTEM experiment is dedicated to measurement of the total and elastic cross-section in proton-proton collisions and of the elastic scattering in pseudorapidity range  $3.1 \geq \eta \geq 6.5$  and  $|\eta| > 10$ . Design documentation can be found in [53], preliminary results in [54].

The ZDCs are installed on both sides of the interaction points in ATLAS, ALICE and CMS experiments. They are designed to measure the energy carried by the non-interacting nucleus travelling at zero degree with respect to the beam direction in heavy ion collisions [55].

In the EAS simulations the development of the air shower depends on assumptions of the interaction cross sections and multiplicity of particle productions in inelastic processes. For example: the primary cosmic ray particle can interact and develop particle cascade high in the atmosphere when interaction cross section and particle multiplicity are high. When the interaction cross section and particle multiplicity are low, primary particles interact and develop particle cascades deep in the atmosphere. Both showers will give different particle numbers at the observation level, leading to different conclusions about mass and energy of the primary particles when compared with the measured data.

The parameters of the theoretical interaction models, based on certain assumptions about constituents of the particles and their interactions, are tuned to describe the collider data as precisely as possible. The interaction models with those parameters are then used to simulate the EAS. The results are compared with measurements of the ground based experiments. Any discrepancies between the measurement and the simulated EAS are used to improve the description of the shower development, thus to improve the hadronic interaction model. This is a long iterative process but it is essential for the interpretation of measured EAS data and the development of the interaction models at energies that are unreachable in accelerator experiments.

## 2.2 EAS simulations in the KASCADE-Grande experiment

EAS simulations are performed with the Monte Carlo code specially developed for the KASCADE experiment: the COsmic Rays Simulation for KASCADE (CORSIKA) [48]. This software is designed to simulate in detail the development of the EAS in the atmosphere, reproducing correct fluctuations around the average values of the observables. All processes that have noticeable influence on the quantities of the EAS are included.

The CORSIKA code covers 50 types of particles and nuclei up to  $A=56$ . All these particles can be tracked until they undergo reactions with air nuclei or they decay, until they reach predefined observation level or their energy falls below predefined energy threshold. In particle decays all decay branches down to the 1% level are taken into account.

The interactions within EAS are described by high-energy and low-energy hadronic interaction models. In CORSIKA it is possible to choose the combination of models. Available high-energy hadronic interactions models are: QGSJet [56–60], EPOS [61], SIBYLL [62], DPMJET [63], VENUS [64], NEXUS [65] and HDPM [66]. Low energy hadronic interactions can be described by FLUKA [67,68], GHEISHA [69] or URQMD [70,71] models. The electromagnetic interactions can be treated with EGS4 [72,73] model or analytically described with the NKG function [74].

The shower can be initiated by various types of the high-energy cosmic ray particles and the transition energy between high and low-energy interaction models can be set by user. Normally it is 200 GeV when using FLUKA or 80 GeV with GHEISHA.

Currently CORSIKA is used by many air shower experiments all over the world.

Parameters of particles reaching observation level of the experiment are a starting point for simulation of the response of the detector array. In the KASCADE-Grande experiment the detector response is simulated with GEANT [75] based Cosmic Ray Event Simulation (CRES) software. Hadronic interactions within the detector are simulated with FLUKA code.

CRES contains description of all detectors in the KASCADE-Grande experiment, their location, geometry, type and technical features (time delays etc.). Information about particles crossing the observation level from CORSIKA is correlated with detector position and the energy released in the detector is calculated. CRES output contains the same type of parameters as obtained with measured data. The simulated data are stored in the same format as the data from the measurement and in the following step of the analysis they can be processed with the same software as measured data.

General scheme of the data analysis in KASCADE-Grande experiment is shown in Fig. 2.2.1.

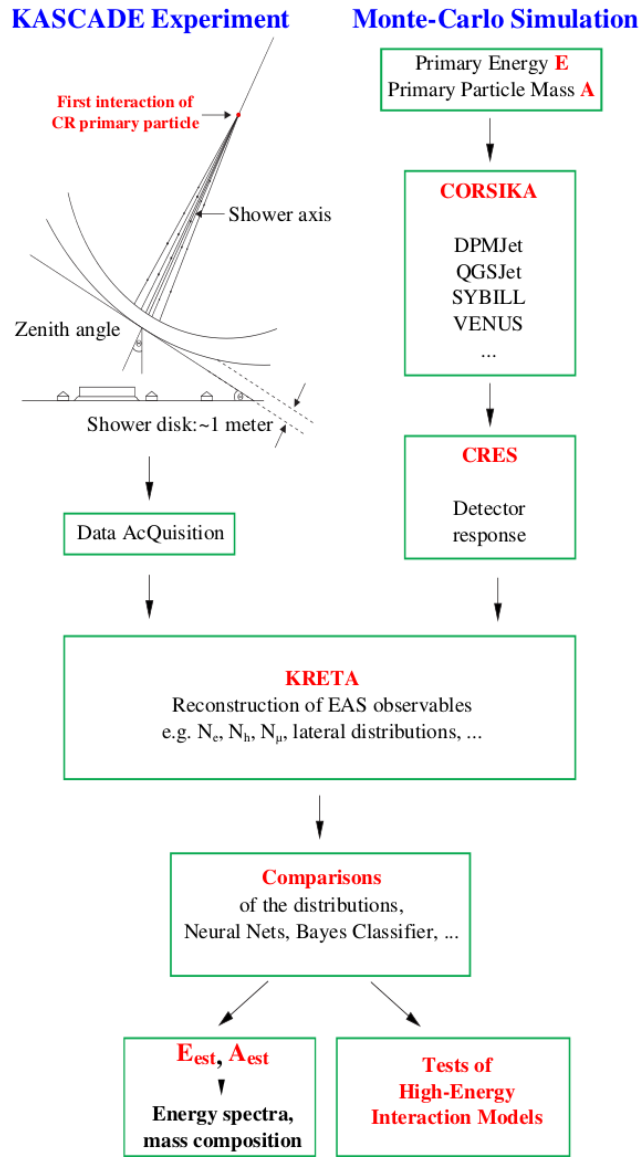


Figure 2.2.1: General scheme of the data analysis in the KASCADE-Grande experiment.

From the particle densities measured in the detector array various EAS observables and their distributions are reconstructed. Independently, the EAS simulations are performed with the CORSIKA.

The CORSIKA output of the simulated EAS that stem from predefined type of cosmic ray particle, energy range and angle range is analyzed with CRES software and then reconstructed with KRETA, using the same routines as measured data. The KRETA output from the simulations and experimental data contains the same EAS observables. Both sets of data

are analyzed with dedicated software.

Reconstruction of the shower parameters from the measured data and simulation with the same software routines can improve EAS simulations by further development of the interaction models. Evolution of the air shower is sensitive to a number of parameters and one can try to predict how they should be changed in EAS description to achieve better agreement with the measurement. However, these parameters are not independent from each other; tuning a model of interest is done in a long, iterative process of introducing small changes into a model and comparing the results with the measurements. Any change in the description of hadronic interactions should give correct description of the collider data and the development of the air showers. As the interaction models improve and the discrepancies between simulations and the measurement are becoming smaller, it is possible to use this model as a reference in comparison with other models that use different approach in describing the interactions. A good example of this approach to model testing can be found in [76] where KASCADE data and QGSJet simulation are used to test the EPOS model.

Figure 2.2.2 shows the inelastic proton-air cross-section as a function of energy, estimated by measurements and predicted by interaction models in 1997 and 2008 (from Ref. [77]). Constant cross-check between measurements and simulations helps to develop interaction models and leads to better description of the data. Currently developed models describe the available low-energy data very well. Differences are visible in high-energy range but they are significantly lower in 2008 than in 1997.

### 2.3 Short characteristics of high energy hadronic interaction models used in KASCADE-Grande

The **QGSJet-II** model is based on the Pomeron phenomenology [78]. The hadronic multiple scattering processes (Gribov's reggeon approach [79, 80]) are described as multiple exchanges of independent microscopic parton cascades - Pomerons. For the soft low-virtuality cascades a phenomenological 'soft' Pomeron amplitude is employed, whereas semi-hard scattering processes are treated as exchanges of 'semi-hard' Pomerons, the latter composed of a piece of QCD parton ladder 'sandwiched' between two soft Pomerons [57, 81]; the soft Pomerons and the ladder describing correspondingly the low and high virtuality parts of the underlying parton cascade. The non-linear parton effects are treated as Pomeron-Pomeron interactions, based on all order re-summation of the corresponding Reggeon Field Theory diagrams [82, 83].

**SIBYLL 2.1** [62] also employs the Pomeron formalism to describe soft processes, while semi-hard ones are treated in the framework of the 'mini-jet'

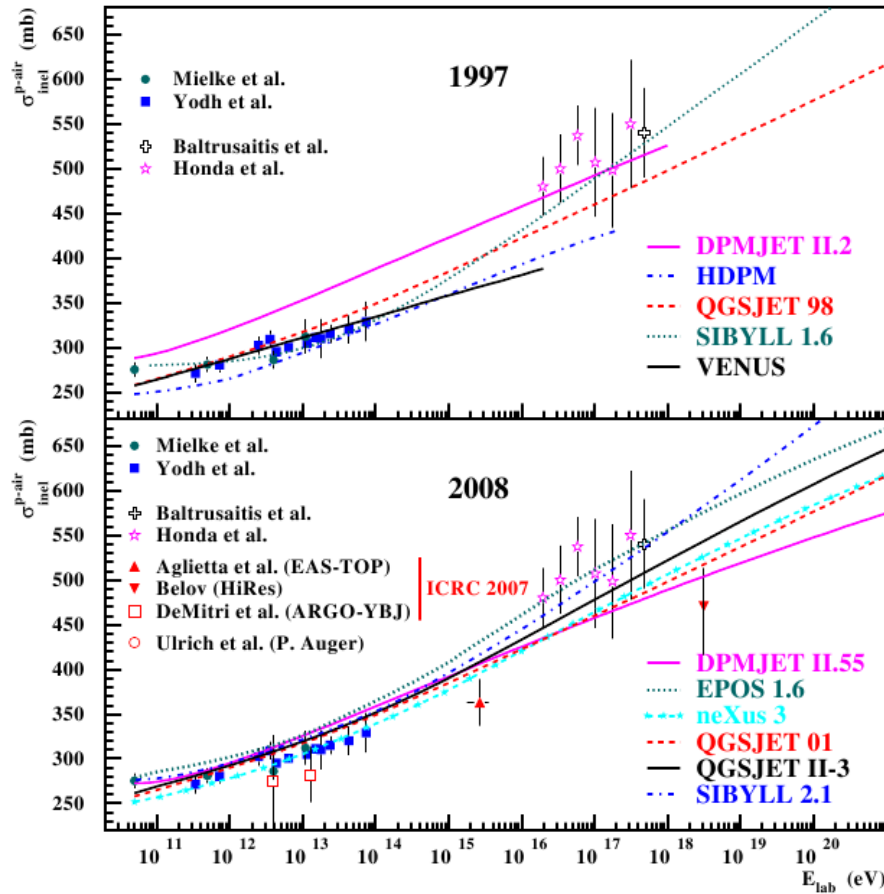


Figure 2.2.2: Inelastic proton-air cross-section as a function of energy estimated by various experiments (symbols) and predicted by various modes and their versions (curves) in 1997 and 2008. From Ref. [77].

approach [84]. The differences between the mini-jet approach and 'semi-hard' Pomeron approach are discussed in [85, 86]. The treatment of non-linear effects in that model is based on the parton saturation [87]. On the other hand, non-linear effects are neglected for the 'soft' interaction component.

The **EPOS 1.99** model employs the soft and semi-hard Pomeron scheme and takes into account energy-momentum correlations between multiple rescatterings [61]. The description of non-linear effects is based on an effective treatment of lowest order Pomeron-Pomeron interaction graphs, with the corresponding parameters being adjusted by comparison with RHIC data. A big advantage of the model is an excellent calibration to available collider data. A special feature is the explicit treatment of projectile and target remnants, leading to a better description of baryon and antibaryon production than in the other models used for cosmic-ray analysis.

## Chapter 3

# The KASCADE / KASCADE-Grande EAS experiment

KASCADE (KARlsruhe Shower Core and Array DETector) [39] is an EAS experiment located at Karlsruhe Institute of Technology (KIT) Campus North (former Forschungszentrum Karlsruhe) in Germany (49° N, 8° E, 110 m a.s.l.  $\approx 1023 \text{ g cm}^{-2}$ ).

The main goals of the experiment, taking data since 1996, have been to study in detail the cosmic ray energy spectrum, mass composition and to identify point sources in the energy range from  $3 \times 10^{14}$  eV to  $10^{16}$  eV. The basic approach of KASCADE is to measure a large number of parameters for each individual shower: electron and muon numbers, the lateral distributions of electromagnetic and muonic components and the number, energy and spatial distribution of hadrons in the shower core. To study cosmic rays above the energy of  $10^{16}$  eV it was necessary to extend the area of the KASCADE experiment. This was done with an array of 37 scintillator detector stations, called Grande [40] and put into operation in 2003.

With an area of  $0.5 \text{ km}^2$  the KASCADE-Grande experiment is able to detect efficiently extensive air showers that stem from cosmic ray particles with energy up to  $10^{18}$  eV. The Grande Array provides information about the all-charged particle component while the KASCADE Array supplies the information on muons and electrons separately. Investigation of the  $3 \times 10^{14}$  eV to  $10^{18}$  eV region of the energy spectrum aims to answer the questions about the origin of the Knee, the question of galactic-to-extragalactic CR transition and of other features of the spectrum, like “the Iron Knee”, predicted by cosmic ray models.

Another important goal is the development of the high energy hadronic interaction models in an energy range and kinematic region not accessible to man-made accelerator experiments. Comparing the multi-observable mea-

surements of KASCADE-Grande with the Monte Carlo simulations of EAS and detectors it is possible to draw conclusions about the validity of the interaction models in the ultra-high energy range.

### 3.1 Detector components of the experiment

The KASCADE-Grande experiment is composed of the KASCADE Array and Grande Array, the Central Detector (CD) with Hadron Calorimeter, the Muon Tracking Detector (MTD) and the Piccolo Array. The layouts of KASCADE and KASCADE-Grande are shown in Fig. 3.1.1 and Fig. 3.1.2. This multi-detector setup was designed to measure all three components of EAS. The electromagnetic component is measured with an array of scintillator detectors, the muonic component by shielded scintillators and tracking chambers at four energy thresholds, and the hadronic component in a sampling calorimeter. A short description of the experiment components can be found in Tab. 3.1. The KASCADE Array and Grande detector stations are connected with the Grande Data Acquisition station (DAQ) located in the centre of the Grande Array.

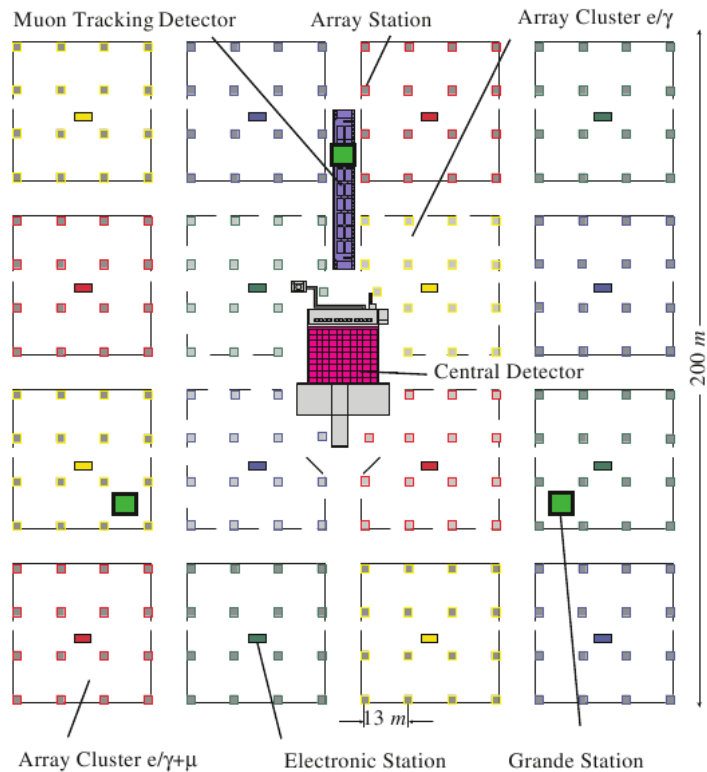


Figure 3.1.1: Layout of the KASCADE experiment. Note the location of the MTD within the Array.

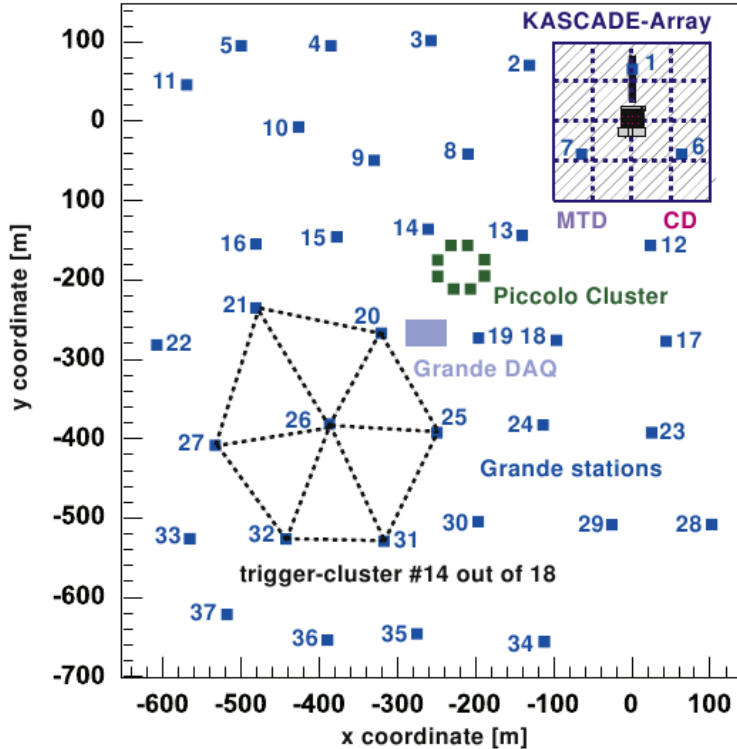


Figure 3.1.2: Layout of the KASCADE-Grande experiment indicating locations of its all components. An example of a trigger hexagon cluster is also shown.

### 3.1.1 The KASCADE detector Array

The KASCADE Array (Fig. 3.1.1) is composed of 252 detector *stations* with a spacing of 13 meters, organized on a square grid  $200 \times 200 \text{ m}^2$  in 16 *clusters*. The stations are grouped in 12 outer clusters with 16 detectors each, and 4 inner clusters with 15 detectors each. The 192 stations located in the outer clusters contain 2 unshielded liquid scintillators, sensitive to charged particles and photons, and 4 shielded plastic scintillators that serve as muon detectors. Each station in the inner clusters contains only 4 unshielded charged particle and photon detectors. The details of the design of the detector station in the outer cluster is shown in Fig. 3.1.3. Extended information about the design and operation of the array can be found in [39].

#### Array of charged-particle/ $\gamma$ detectors

Each charged-particle/ $\gamma$  detector in the KASCADE Array (shown in detail in Fig. 3.1.3 as  $e/\gamma$  because electrons dominate the sample) consists of a circular stainless steel vessel container of 1 meter diameter, filled with 5 cm of a liquid scintillator. The light collection cone and 3 inch photomultiplier (PMT) is mounted on top of it. The volume above the scintillator is filled

Table 3.1: Components of the KASCADE-Grande experiment

Detectors	Detected EAS particles	Area	Energy threshold
<b>KASCADE Array:</b>			
Liquid scintillators	$e/\gamma+\mu$	490 m <sup>2</sup>	5 MeV
Plastic scintillators	$\mu$	622 m <sup>2</sup>	230 MeV
<b>Grande Array:</b>			
Plastic scintillators	$e/\gamma+\mu$	37×10 m <sup>2</sup>	5 MeV
<b>Central Detector:</b>			
Ionization chambers	h	9×304 m <sup>2</sup>	50 GeV
Plastic scintillators	$\mu$	208 m <sup>2</sup>	490 MeV
Streamer tubes	$\mu$	247.5 m <sup>2</sup>	2.4 GeV
MWPC <sup>a</sup>	$\mu$	2×129 m <sup>2</sup>	2.4 GeV
Plastic scintillators	e	23 m <sup>2</sup>	5 MeV
<b>MTD:</b>			
Limited streamer tubes	$\mu$	4×128 m <sup>2</sup>	800 MeV
<b>Piccolo:</b>			
Plastic scintillators	$e/\gamma+\mu$	80 m <sup>2</sup>	5 MeV

<sup>a</sup> Multi-Wire Proportional Chambers

with argon to prevent oxidation of the scintillator. The cylindrical geometry helps to achieve homogeneous response and time resolution of 0.77 ns. The linear dynamic range of the PMTs reaches 2000 particles per m<sup>2</sup>. The energy resolution is  $\approx 8\%$  at 12 MeV. The energy threshold for a charged-particle/ $\gamma$  is 5 MeV.

### Array of muon detectors

The muon detectors in the Array (shown in details in Fig. 3.1.4 ) consist of plastic scintillators under absorber, made out of 10 cm of lead and 4 cm of iron (what corresponds in total to 20 radiation length). The shielding eliminates most of the particles from electromagnetic component of EAS and results in an energy threshold of 230 MeV for vertical muons. There are four quadratic segments (90×90 cm<sup>2</sup> each) of 3 cm thick plastic scintillator. The light signal emitted in the two neighboring segments is collected by the wavelength shifter bar and read out by one of the four 1.5 inch PMTs. The time resolution of the muon detector was estimated to be  $\approx 2.9$  ns. The obtained energy resolution is  $\approx 10\%$  at 8 MeV.

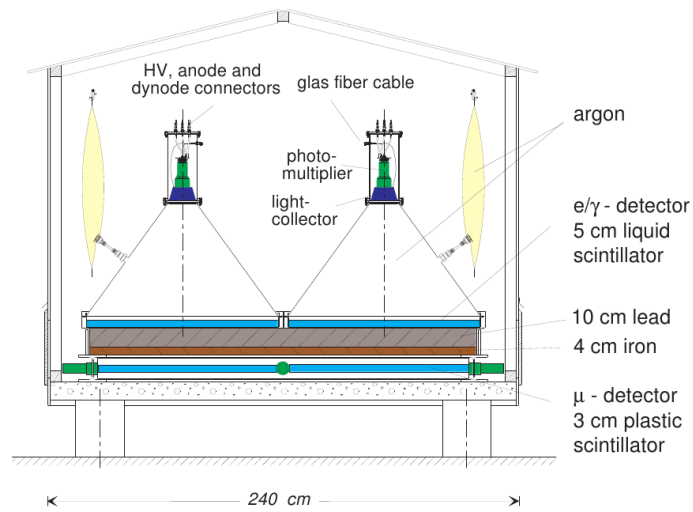


Figure 3.1.3: Sketch of the fully equipped detector station in the KASCADE Array.

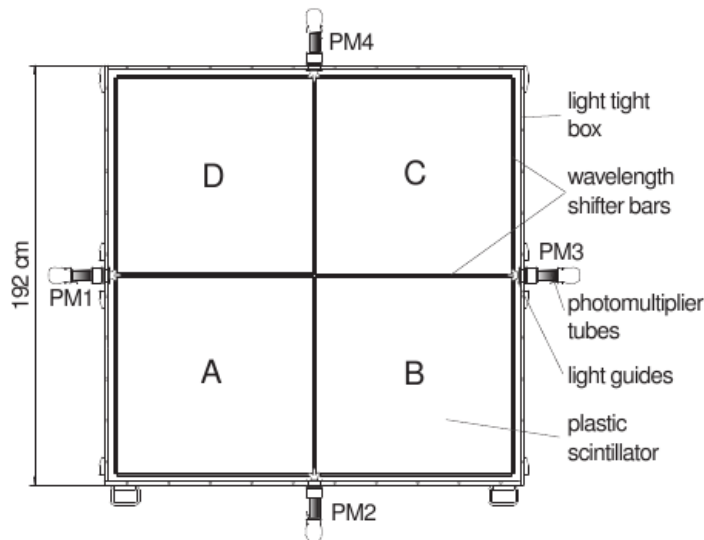


Figure 3.1.4: Schematic layout of the muon detector in the Array.

### 3.1.2 The Grande detector Array

The detector Array which constitutes the Grande extension to KASCADE (see Fig. 3.1.2) is composed of 37 detector stations measuring the electromagnetic component of the shower. Containers with the hardware are distributed all over the Campus North and occupy an area of  $700 \times 700 \text{ m}^2$ . Three Grande stations are located within the KASCADE Array.

Grande detectors are organized in 18 clusters on a hexagonal grid with a mean spacing of 137 meters. Each station contains 16 plastic scintillators ( $10 \text{ m}^2$  of total area) in  $4 \times 4$  configuration (Fig. 3.1.5). The scintillator module is closed in a pyramidal metal case for protection from external light. The scintillation light is detected with PMT mounted at the top of each pyramid. All modules are equipped with high gain PMTs that generate a signal when particle density is in range 0.03–200 particles per  $\text{m}^2$ . To avoid saturation in case of high particle densities, the inner four modules are equipped with low-gain PMTs giving signal when particle density is in the range 200–3000 particles per  $\text{m}^2$ . An extended description can be found in [40].

All 37 Grande stations are connected to the Grande-DAQ via 700 meter long cables. Here, the stations are electronically connected into 18 hexagonal trigger clusters, each consisting of one central and six surrounding stations, except the cluster 15, which is composed out of 6 detector stations only. The trigger signal is created when 7-out-of-7 stations in the hexagon are fired.

Inputs for the Grande DAQ are: the shaped detector signals, logic and timing signals from the 37 stations, the time-stamp signals (1 Hz and 5 MHz) and the KASCADE trigger from the KASCADE components.

### 3.1.3 The Central Detector

The Central Detector (CD) is located in the centre of the KASCADE Array. Its main task is the measurement of hadron densities in EAS core and the energies of individual hadrons.

The main part of the detector is the hadron sampling calorimeter that covers an area of  $320 \text{ m}^2$ . It is constructed from 8 layers of warm- liquid ionization chambers separated by 9 layers of casted iron slabs. The total

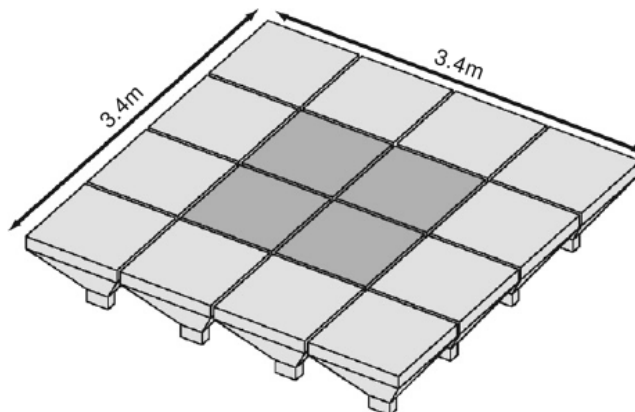


Figure 3.1.5: Schematic diagram of a Grande detector station. Modules with low gain PMTs are marked in dark yellow.

calorimeter thickness is equivalent to 11.5 nuclear interaction lengths and absorbs hadrons with energies up to 25 TeV. A detailed description of the calorimeter can be found in Ref. [88].

On top of the CD the top-cluster and top-layer are mounted. The top-cluster is composed of 25 plastic scintillators. Its purpose is to fill the gap in the centre of KASCADE Array. The top-cluster together with top-layer are also used to investigate the electromagnetic cores of low energy EAS.

Underneath the third absorber plane, a layer of plastic scintillators serves as timing facility and source of trigger for all components of the CD. It covers an area of  $\approx 205 \text{ m}^2$  and detects muons with energy above 490 MeV.

In the basement of the CD the muon chamber system is installed for measurement of muons that accompany the hadrons. It is a combination of multi-wire proportional chambers and a layer of limited streamer tubes that improves the reconstruction of muon tracks. It covers an area of  $129 \text{ m}^2$  and can detect muons with energy above 2.4 GeV.

More information about the Central Detector can be found in [39,88–90].

#### 3.1.4 The Muon Tracking Detector

The Muon Tracking Detector (MTD) is installed in a concrete tunnel 1.7 meter below the level of Array detectors in the northern part of KASCADE. To select muons with energy above 800 MeV and to eliminate the influence of the electromagnetic component of the shower the tunnel is covered with a shielding made out of soil, iron plates and concrete. The MTD consists of 16 muon telescopes made out of limited streamer tubes. This detector is presented in detail in chapter 4.

#### 3.1.5 The Piccolo Array

In cases when the shower core is located within the Grande Array, far away from KASCADE, it is possible that the trigger signal from Grande would be too late for the muon detectors in the CD and the MTD. To provide an efficient trigger also in such cases a small trigger array, called Piccolo, was build. It is composed out of eight stations, each containing  $10 \text{ m}^2$  of plastic scintillators, sensitive to charged particles with energy above 5 MeV. More details about the design and operation can be found in Ref. [40].

### 3.2 The reconstruction of EAS

Each extensive air shower is characterized by a number of observables: arrival direction, core position, slope of lateral distribution function (*shower age s*), total number of charged particles  $N_{ch}$ , muons  $N_\mu$  and electrons  $N_e$  (called *shower sizes*). The aim of the reconstruction procedure is to derive

those parameters from energy deposits and timing information in scintillation counters. For this purpose the KASCADE Reconstruction of ExTensive Air showers (KRETA) code was developed, which later has been adapted for the analysis of Grande Array data.

KRETA reads the raw data (digitalized integrated anode signals of each station and arrival time of the first particle there), performs the calibration and reconstructs the basic observables. The results are being stored as histograms and vectors of parameters.

In the following we shall focus on the description of reconstruction algorithms used for an event where the Grande Array, KASCADE Array and the MTD are taking part in an event.

### 3.2.1 Reconstruction of arrival direction

To obtain the arrival direction of registered EAS the shower transit times measured by Grande detectors are used. The information about the arrival times of the first particle are compared with expected one from a theoretical shower front structure through a minimization of  $\chi^2$  procedure.

Theoretical shower front is obtained with CORSIKA air shower simulations and GEANT based simulations of the detectors in the experiment. Outputs of the fitting procedure are the zenith and azimuth angles that identify the orientation of the shower axis and arrival time of the particles in the shower core.

### 3.2.2 Charge particle shower size and the slope of lateral distribution

In order to reconstruct the shower size the energy deposit in the scintillators is converted into the number of charged particles. This is performed by applying a *lateral energy correction function* (LECF), which corrects for the energy dependence of the stopping power and the energy release originating from photon conversion in the detector or its surroundings. This function is derived from CORSIKA and detailed GEANT simulation of the detectors. The dependence of the LECF on the distance to the shower core is described by equation 3.2.1 and shown in Fig. 3.2.1. The constant value above 450 meters corresponds to the mean energy deposit of vertical muons. The LECF shows the energy deposit in MeV per charged particle.

$$\text{LECF}(r) = \begin{cases} e^{(1-0.1r)} + 7.51 + 0.02r + r^2 5.5 \cdot 10^{-5} + r^3 5.4 \cdot 10^{-8} & r \leq 450 \\ \text{LECF}(450) & r > 450 \end{cases} \quad (3.2.1)$$

The charged particle shower size  $N_{ch}$  and the slope parameter of the lateral distribution function – age  $s$  – are calculated by means of a maximum likelihood procedure comparing the measured *lateral distribution function*

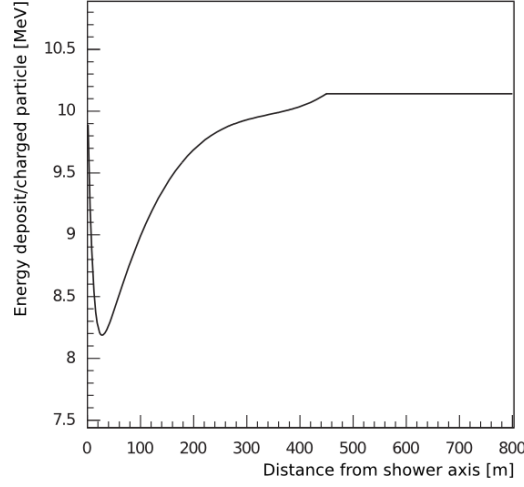


Figure 3.2.1: The LECF for Grande detectors

(LDF) with a theoretical one. The expected LDF is a modified NKG [32,33] lateral distribution function of charged particles:

$$\rho_{ch}(r) = N_{ch} \cdot f_{ch}(r) = N_{ch} \cdot C(s) \left(\frac{r}{r_0}\right)^{s-\alpha} \left(1 + \frac{r}{r_0}\right)^{s-\beta} \quad (3.2.2)$$

where  $r$  is the distance from the shower core, and

$$C(s) = \Gamma(\beta - s) / (2\pi r r_0^2 \cdot \Gamma(s - \alpha + 2) \cdot \Gamma(\alpha + \beta - 2s - 2))$$

The values of the parameters,  $\alpha = 1.5$ ,  $\beta = 3.6$ ,  $r_0 = 40$  meters, are obtained with CORSIKA simulations [91].

### 3.2.3 Muon shower size— $N_\mu$

In order to obtain the lateral distribution of muons the energy deposits in the KASCADE muon detectors are first converted to particle numbers by means of a conversion function. The conversion function is given by the equation (3.2.3) and shown in Fig. 3.2.2.

$$\frac{E_{dep}(r)}{\text{muon}} = \left(7.461 + e^{(1.762 - 0.0166 \cdot r)} + 0.0002886 \cdot r\right) MeV \quad (3.2.3)$$

The lateral distribution of muons is fitted with a function based on the one proposed by Lagutin and Raikin [92,93], where  $N_\mu$  is set to the reconstructed mean muon number  $N_\mu^{rec}$ .

$$\begin{aligned} \rho_\mu &= N_\mu \cdot f_\mu(r) \\ &= N_\mu \cdot \frac{0.28}{r_0^2} \left(\frac{r}{r_0}\right)^{p_1} \left(1 + \frac{r}{r_0}\right)^{p_2} \left(1 + \left(\frac{r}{10 \cdot r_0}\right)^2\right)^{p_3} \end{aligned} \quad (3.2.4)$$

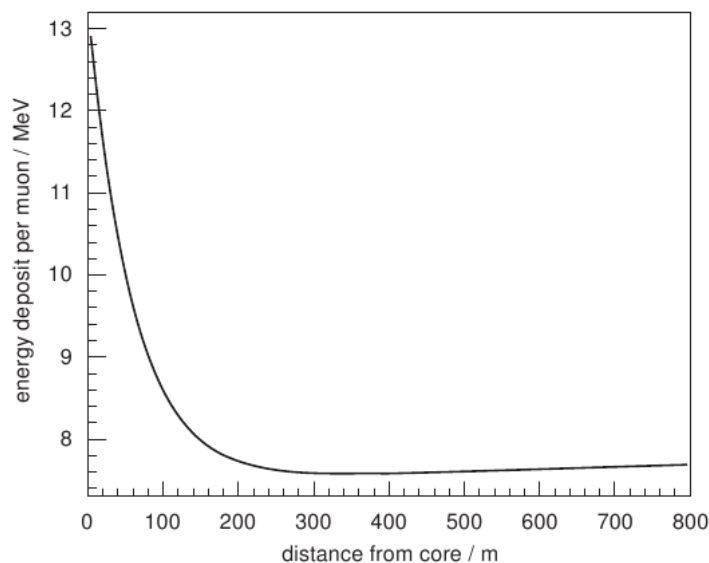


Figure 3.2.2: Muon LECF: average energy deposit per muon in KASCADE muon detectors as a function of the detector distance to the shower core.

The parameters  $p_1 = -0.69$ ,  $p_2 = -2.39$ ,  $p_3 = -1.0$ ,  $r_0 = 320$  meters are found by means of CORSIKA simulations using the QGSJet01 model.

The reconstructed muon number  $N_\mu^{rec}$  is obtained from the maximum likelihood estimation assuming the locally detected muons to fluctuate according to a Poisson distribution:

$$N_\mu^{rec} = \frac{\sum_{i=1}^k M_i}{\sum_{i=1}^k (f_\mu(r_i) \cdot A_i \cdot \cos\theta)} \quad (3.2.5)$$

where  $M_i$  is the number of particles measured at a core distance  $r_i$  in one of the  $k$  detectors with sensitive area  $A_i$ ,  $\theta$  is the zenith angle of the shower, and  $f(r_i)$  is the lateral distribution function (3.2.4).

### 3.2.4 Iterative procedure of the event reconstruction

To obtain the best determination of the shower observables the following iterative procedure is applied:

1. Shower parameters are estimated analytically: the coordinates of the shower core are being found as the barycenter of charges measured by the detectors.
2. The core position is being moved over a  $7 \times 7$  grid with 8 meter spacing. In each position of the shower core slope  $s$  and charged particle shower size  $N_{ch}$  are fitted. The position providing the minimum  $\chi^2$  is chosen as a starting point.

3. The arrival direction is found as described in chapter 3.2.1.
4. The lateral distribution of charged particles is fitted with the maximum likelihood procedure, using equation (3.2.2) with  $N_{ch}$  and  $s$  as free parameters.
5. The lateral distribution fit is performed again with shower core coordinates as free parameters.
6. The steps 3 and 4 are repeated, to obtain the final values for the arrival direction,  $N_{ch}$  and  $s$ .
7. The number of muons  $N_{\mu}$  is obtained with the procedure described in chapter 3.2.3.
8. The electron size  $N_e = N_{ch} - N_{\mu}$  is calculated.

### 3.2.5 Trigger and reconstruction efficiency

The trigger and reconstruction efficiencies are determined using Monte Carlo simulations of EAS and detector response. Only showers that fulfill quality conditions with a shower core within defined fiducial area and with properly reconstructed shower sizes are taken into account. Details on the work for the definition of these cuts can be found in Ref. [94]. The behaviour of the total (trigger and reconstruction) efficiency is shown in Fig. 3.2.3 as a function of the reconstructed total number of charged particles  $N_{ch}$  and the primary energy  $E_0$ .

The full efficiency is reached for energies above  $\approx 10^7$  GeV. Looking at the efficiency as a function of  $N_{ch}$ , one can notice that iron initiated showers reach full efficiency earlier. This is due to the fact that for lower energy showers the geometrical structure of the Grande Array requires already muons for triggering these events.

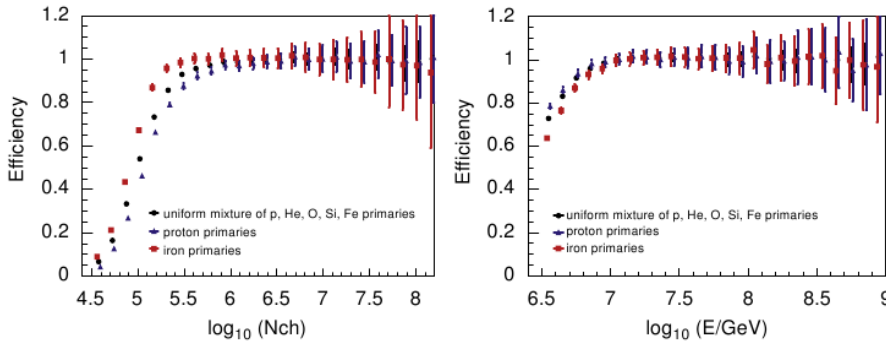


Figure 3.2.3: Trigger and reconstruction efficiency for different primaries versus reconstructed shower size (left panel) and simulated primary energy (right panel). The points for proton and iron assumption are slightly shifted for a better visibility [40].

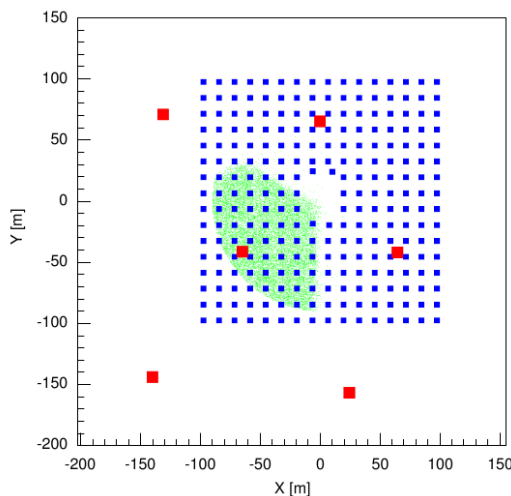


Figure 3.2.4: The event selection for the comparison of Grande and KASCADE data. Green dots display core positions of some events. Position of the Grande and KASCADE stations are marked as red and blue squares.

### 3.2.6 Reconstruction accuracy

One of the methods through which the reconstruction accuracies can be derived is comparison with a reference experiment. In case of the KASCADE Grande experiment the Grande Array can be compared with KASCADE where the detector sampling fraction is 15 times larger than in Grande. Therefore, the resolutions in KASCADE are expected to be much better than in Grande so that the reconstructed KASCADE observables may be regarded as *reference* ones in the comparison between the two arrays. The differences of the shower parameters reconstructed by Grande and KASCADE are analysed for a subsample of Grande showers, having core location common to the fiducial areas for both arrays (Fig. 3.2.4) where the shower size covers the range between Grande full efficiency threshold  $\lg(N_{ch}) > 5.8$  and the KASCADE highest reconstructable size  $\lg(N_{ch}) < 7.2$ .

For the **charged size accuracy** the following distribution (Fig. 3.2.5) is taken into account:

$$\delta N_{ch} = \frac{N_{ch}^G - N_{ch}^K}{N_{ch}^K} \quad (3.2.6)$$

where  $N_{ch}^G$  and  $N_{ch}^K$  are sizes obtained for Grande and KASCADE, respectively. The relative accuracy of charged size of a shower is of 10% - 15%.

The **core position accuracy** is derived from the distribution of core differences (see Fig. 3.2.6):

$$\delta_r = \sqrt{(x_G - x_K)^2 + (y_G - y_K)^2} \quad (3.2.7)$$

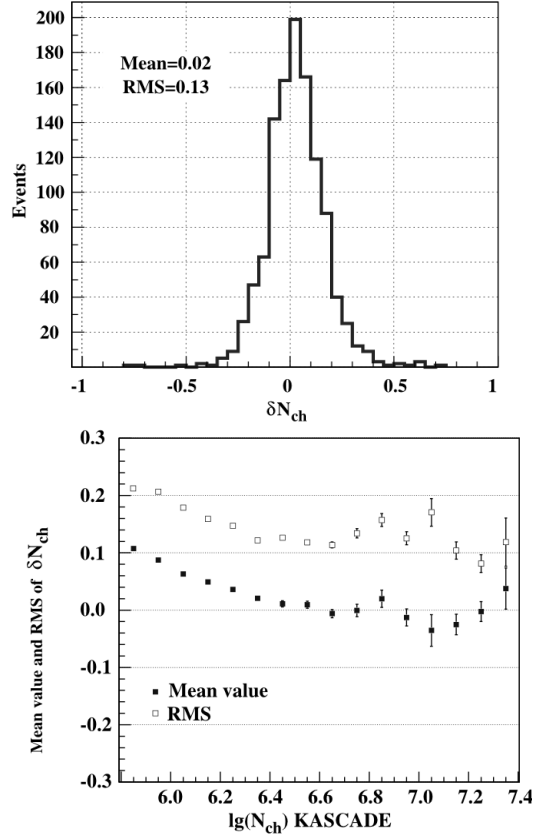


Figure 3.2.5: **Top panel:** example of the distribution of  $\delta N_{ch}$  for  $6.4 < N_{ch} < 6.5$ . **Bottom panel:** accuracies and fluctuations on the shower size, obtained as the mean values and the RMS of  $\delta N_{ch}$  (3.2.6). Large fluctuations in the RMS at larger shower sizes is due to small statistics. [40]

where  $x_G, y_G$  and  $x_K, y_K$  are the x, y coordinates of the reconstructed core position of Grande and KASCADE, respectively, and defined by a condition that 68% of the events have deviations less than it. As it is visible on the right panel of Fig. 3.2.6 the core position accuracy improves from 8 to 5 meters with increasing  $N_{ch}$ .

The **arrival direction accuracy** is derived from the distribution of the angle between KASCADE and Grande reconstructed arrival directions (see Fig. 3.2.7) and defined by 68% of the events having deviations less than it.

$$\delta_\alpha = \arccos(\cos(\theta_K) \cdot \cos(\theta_G) + \sin(\theta_K) \cdot \sin(\theta_G) \cdot \cos(\phi_K - \phi_G)) \quad (3.2.8)$$

where  $\phi_K, \theta_K$  and  $\phi_G, \theta_G$  are zenith and azimuth angles of the same shower reconstructed by KASCADE and Grande, respectively. The accuracy exhibits weak dependence on shower size with the minimum at about  $\lg(N_{ch}) = 6.4$ , being basically constant at the level of  $\approx 0.8^\circ$ .

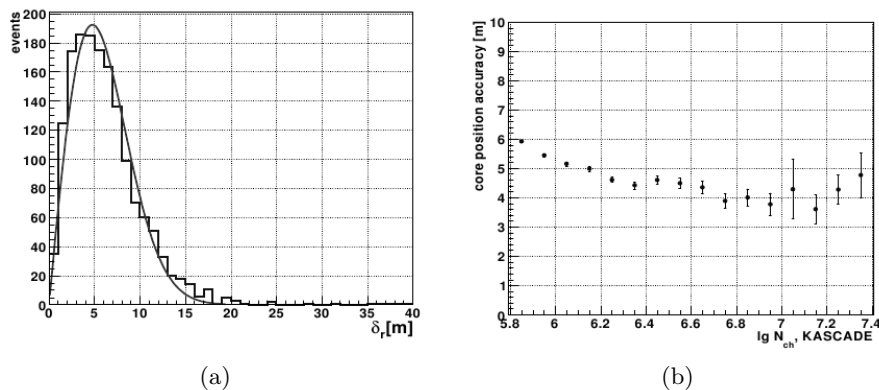


Figure 3.2.6: Panel (a): example of  $\delta_r$  distribution of the core position compared to a 'Rayleigh' probability distribution in the interval  $6.3 < \lg(N_{ch}) < 6.4$ . Panel (b): the core position accuracy as a function of charged particles shower size. [40]

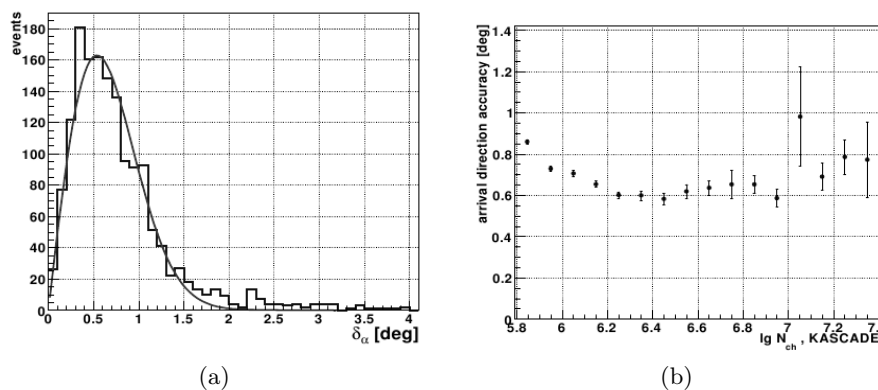


Figure 3.2.7: Panel (a): example of  $\delta_\alpha$  distribution of the arrival direction compared to a 'Rayleigh' probability distribution. Panel (b): the arrival direction accuracy as a function of charged-particle shower size. [40]

Since muon numbers are only reconstructed from KASCADE muon detectors, their uncertainties can only be derived from EAS simulations. In this analysis showers initiated by different primaries (H, He, C, Si and Fe) in equal abundances, with  $E^{-3}$  power law spectrum, up to  $40^\circ$  in zenith angle and shower cores randomly distributed over the Grande Array were considered. Showers were reconstructed with CRES and KRETA software. Only those which fulfill trigger efficiency condition  $\lg(N_\mu^{true}) > 5.0$  were taken into account. Fig. 3.2.8 shows the result of the analysis: the median of relative deviation of the reconstructed to the true muon number as a function of the true muon number (panel (a)) and as a function of the distance of the shower core to the centre of the KASCADE Array (panel (b)). The errors bars, that

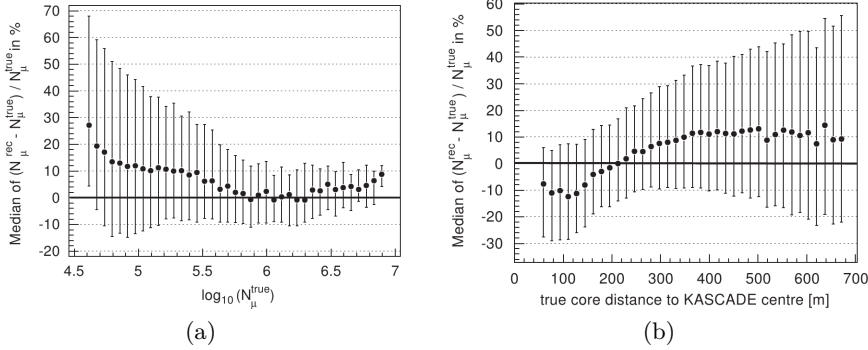


Figure 3.2.8: Muon reconstruction quality derived from Monte Carlo simulations. Panel (a): median of relative deviation of the reconstructed to the true muon number as a function of the true muon number. Panel (b): median of relative deviation of the reconstructed to the true muon number as a function of the distance of the shower core to the center of the KASCADE Array. Error bars represent the quantiles at 84% and at 16%.

represent quantiles at 16% and 84%, between which 68% of the distribution is contained. For the muon numbers above  $\lg(N_{\mu}^{true}) > 5.6$  ( $\sim 5 \times 10^{16}$  eV) the deviation of the reconstructed muon number is less than 5% with statistical error on an event-by-event basis of 10% (panel (a)). The uncertainty of the reconstructed muon number increases with increasing distance from the KASCADE centre from approximately 20% at 100 meters to 60% at 600 meters (panel (b)). The lateral distribution function fitted to measured local densities does not reflect the true values of the densities. This leads to over- and underestimation of the total muon number to about +10% and -10% at large and small distances to the shower core, respectively.

### 3.2.7 An example of an EAS event

In Fig. 3.2.9 an example of an EAS event is shown. The registered by KASCADE and Grande Array energy deposits in charged particle detectors are presented in the left pictures (top and middle panels). The energy deposits in muon detectors in the KASCADE Array are shown in the left bottom picture. From this information the electron and muon shower sizes and the position of the shower core can be estimated. In the example the shower core is located in KASCADE Array: 66 meters to the West and 49 meters to the South of the centre of KASCADE, the electron shower size  $N_e$  is  $9.5 \times 10^6$ , the muon shower size  $N_{\mu}$  is  $1.2 \times 10^5$ . The relative arrival times of the particles in charged particle detectors registered by KASCADE and Grande Array are shown on the right pictures (top and middle panels). The relative arrival times of the particles in muon detectors in the KASCADE Array are

shown in the right, bottom picture. This information is used to estimate arrival direction of the shower (here the shower came from South-West (zenith angle= $33.1^\circ$  and azimuth angle= $226^\circ$  in geographical coordinate system).

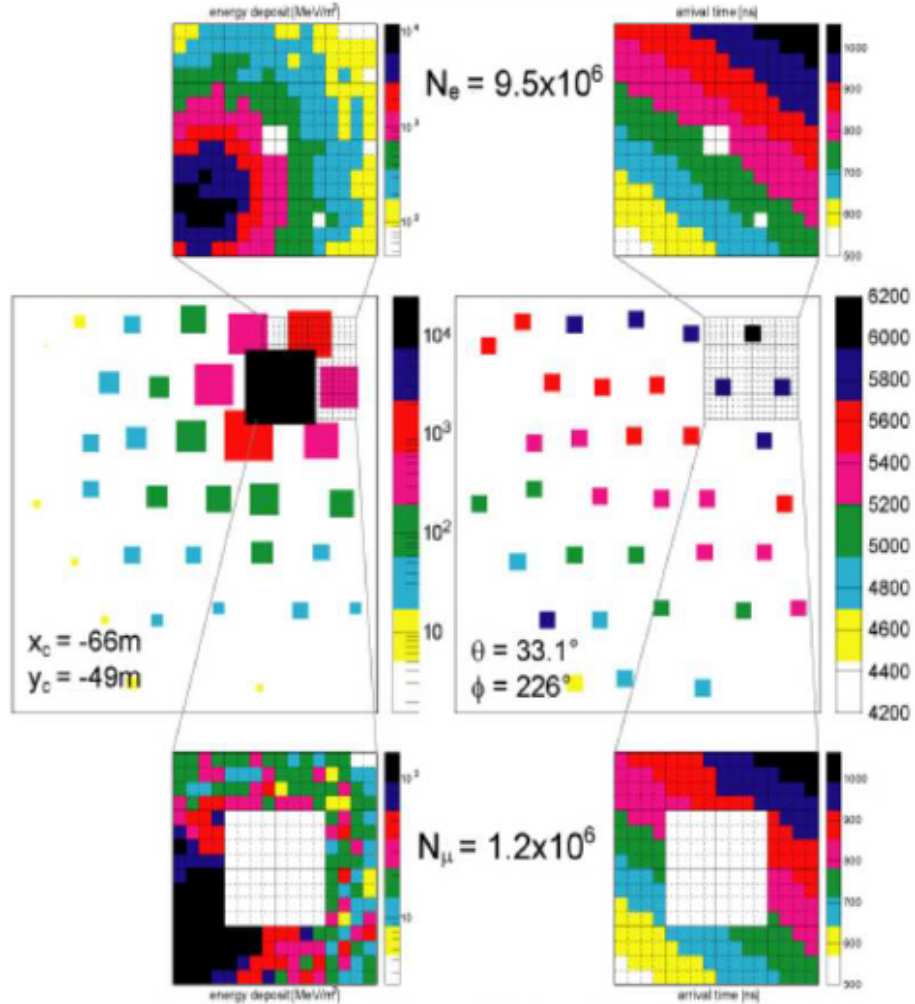


Figure 3.2.9: KASCADE-Grande event-display, on the left the energy deposit, on the right the arrival time, measured by KASCADE Array  $e/\gamma$ -detectors (top panel), KASCADE Array muon detectors (bottom panel) and Grande detectors (middle panel).

## Chapter 4

# The Muon Tracking Detector

The Muon Tracking Detector is designed to reconstruct directions of muons in EAS detected by KASCADE and Grande detector arrays. The detector is a setup of streamer tube (ST) muon telescopes located in a concrete tunnel under the soil-iron-concrete absorber. Directions of muons reconstructed with the muon telescopes allow to investigate the mean muon production height (MPH), pseudorapidity of muons, muon densities and their multiplicities.

### 4.1 Design of the MTD

The MTD is located in the northern part of the KASCADE Array (as shown in Fig. 3.1.1). Its components are placed in the  $5.4 \times 2.4 \times 44$  m<sup>3</sup> concrete tunnel buried under absorber made of iron plates separated with soil. This shielding is an equivalent of 18 radiation lengths and absorbs most of the low-energetic electromagnetic particles, thus enhancing the identification of the tracks from muons with an energy larger than 800 MeV. The centre of the MTD tunnel is 54.65 meters away from the centre of the KASCADE scintillator array which supports the detection of muons with some transverse momentum with respect to the hadrons detected in the hadron calorimeter.

The MTD tunnel houses 16 muon telescopes (called *detector towers*) made out of *streamer tubes*, (ST). The streamer tubes are grouped in *detector modules*. Each telescope is made out of four modules, three horizontal and one vertical (Fig. 4.1.1). The middle module is located 1.7 meter below the level of the KASCADE scintillator array. Total area for detection of vertical muons is 128 m<sup>2</sup>.

An extended description of the design, performance and tests of the MTD can be found in [95,96].

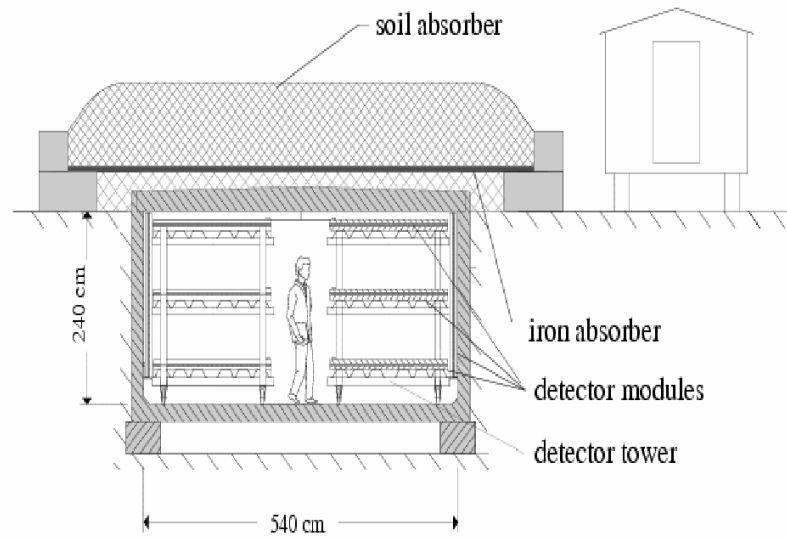


Figure 4.1.1: Cross-section of the MTD.

#### 4.1.1 Streamer tube chamber design

The ST chambers are made of comb profiles of high resistivity PVC with very-well defined conductivity. The chamber is covered with bakelite sheet closing the electric field around the anode wire when a negative high voltage is applied to the cathode profile.

The ST chamber houses 16 anode wires in two cathode comb profiles, extruded for eight parallel ST cells,  $9 \times 9 \text{ mm}^2$  in cross-section and 4 meters in length each. The tolerance of the ST cell geometry is better than 0.1 mm. Anode wires are made out of copper-beryllium alloy,  $100 \mu\text{m}$  in diameter, tempered and smoothed by evaporating  $\approx 0.3 \mu\text{m}$  of silver which helps to reduce the dark current. The wires are supported by spacers every 500 mm.

To the each comb profile end-pieces were glued, which carry printed circuit boards, onto which the anode wires are soldered. The comb profiles, together with the mounted wires, were slid into PVC envelopes, which were sealed off with endcaps exhibiting connectors for anode wires, high voltage (HV) and gas. Two neighboring ST wire cells are combined on the adapter board giving four wire signals out of one 8-cell comb profile. Details of the ST chamber design are shown in Fig. 4.1.2 and its main technical parameters are summarized in Tab. 4.1. The ST chambers are filled with a gas mixture containing: 54% of carbon dioxide, 30% of isobutan, 14% of argon and 2% of ethanol. The cathode voltage is of the order of 4.7 kV.

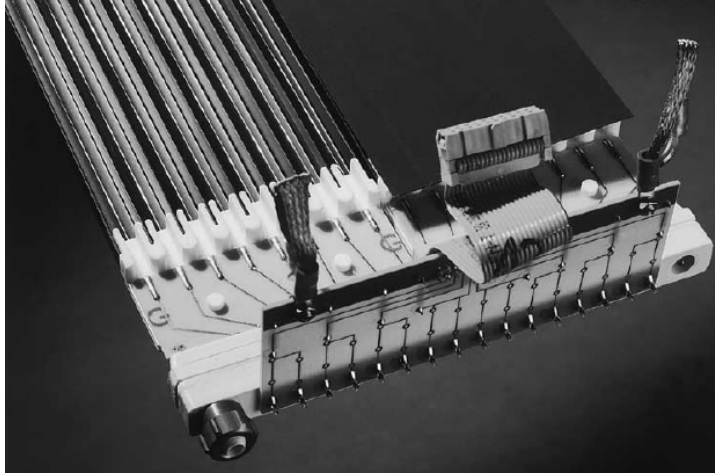


Figure 4.1.2: Detailed view of an opened ST chamber with installed adapter board.

Table 4.1: ST chamber design parameters

PVC profile resistivity	$10^5 \Omega/\square$
Bakelite cover resistivity	$10^{11} \Omega \text{ cm}$
Anode wire diameter	$100 \mu\text{m}$
Anode wire tension	$3 \text{ N at } 20^\circ\text{C}$
Wire sagging between spacers	$42 \mu\text{m}$
ST chamber dimensions	$13 \times 166.6 \times 4000 \text{ mm}^3$

#### 4.1.2 Detector module design

A detector module of the size  $2 \times 4 \text{ m}^2$  is made out of 12 ST chambers. The ST chambers are contained between two layers of a rigid polyester foil,  $75 \mu\text{m}$  thick, with evaporated aluminum strips with a pitch of 20 mm. Strips in the top layer are perpendicular to the wires while strips on the bottom layer are oriented at an angle of  $30^\circ$  with respect to the wires. The electrical contact with strips is achieved by screwing a broad zinc-coated washer together with the polyester foil onto a rigid PVC board. Further adapter boards are soldered onto the silver-coated screws for enabling connection to the readout electronics (Fig. 4.1.3).

The ST chambers with the strip foils are sandwiched between the two layers of high-density styrofoam and are resting on a thin, 0.7 mm, rigid steel structure (Fig. 4.1.4). In a detector tower wires in horizontal modules are spaced vertically by 820 mm.

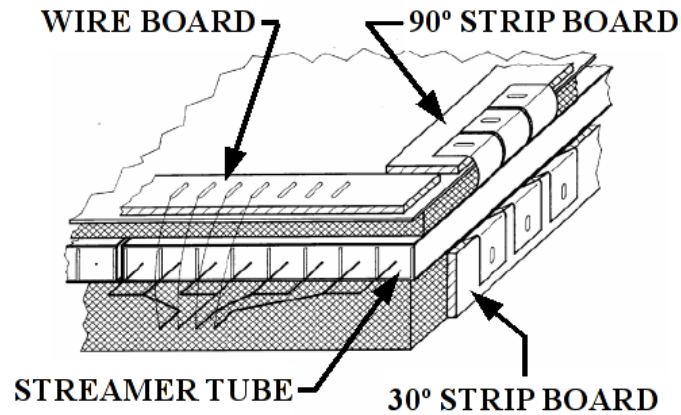


Figure 4.1.3: Scheme of the MTD module design. The PVC boards for fixing signal outputs from wires and strips are shown.

### 4.1.3 Gas supply system

The streamer tubes are supplied with argon-isobutan-carbon dioxide-ethanol gas mixture<sup>1</sup>. From a temperature stabilized container located outside the MTD these gases flow to a gas mixer, where membrane valves allow a fine tuning of the pressure of each gas component. The gas composition is checked with gas flow meters after each membrane valve and before the mixer. From the mixer the gas is distributed into 16 channels using 16 needle valves. Each channel is connected to one detector tower; gas runs in series through all chambers of the top, middle, bottom and vertical modules (240 dm<sup>3</sup> per module). With a gas flow rate of 0.5 dm<sup>3</sup>/h the gas is exchanged in the full detector volume after about 20 days.

### 4.1.4 Readout and data acquisition electronics

The chain-type readout system is used, being divided into three levels:

- Front-End electronics (FE)
- Splitter Boards (SB)
- Streamer Tube Acquisition System (STAS) controllers

The Front-End electronics, made in 32-channel architecture, is mounted on the detector modules. Each module requires three wire boards and nine strip boards to convert analog signals from wires and strips, that exceed predefined threshold, into binary information (hit/no-hit) that is used in track reconstruction. This conversion is done with circuits combining the

<sup>1</sup>see chapter 4.1.1

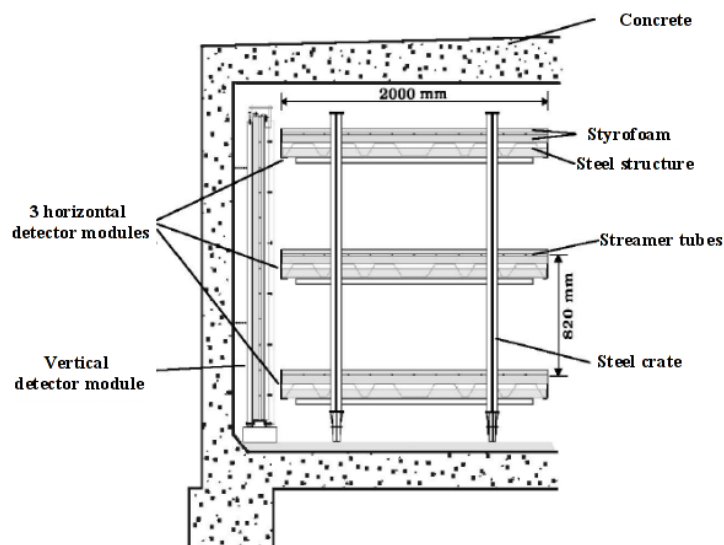


Figure 4.1.4: Scheme of the detector tower. Positions of the detector modules within the tower are shown.

discriminator and one shot functions. The output of the one-shot is a logical pulse  $4 \div 6 \mu\text{s}$  long, depending on the time-over-threshold value of the input pulse [96]. A logical “OR” of all 32 discriminator output pulses on board (DIGOR) is used internally for loading shift register when a coincidence with an external trigger occurs. It is also available for external use outside the board (e.g. for triggering purposes of other devices).

A coincidence with external trigger must occur within the time when the pulse is present at the one-shot output, in order to register a hit. This condition is always met for KASCADE Array generated triggers, for which the MTD was originally built. The MTD operation in KASCADE and Grande environment is discussed in chapter 4.2.2.

In addition, an analog sum (ANOR) of the combined wire signals for 4 ST chambers (one board) delivers additional information about the hit pattern [95].

When the trigger condition is fulfilled, this binary information is loaded into 32-bit long shift register. The FE boards of two module combinations (bottom+middle and top+wall) are connected in series and connected to the dedicated Splitter Board, forming one 768-bit long shift register.

During the readout cycle, the data from the register are shifted out via the bus into the CAEN C267 STAS controller. Four controllers are needed to handle information from 16 detector towers. One CAMAC crate contains STAS controllers. A VME crate houses trigger electronics, controller for CAEN HV System, ADC for monitoring temperature, gas pressure and flow rate, and a Transputer-based VME controller for communication via

optic links with the central host in the KASCADE acquisition system. The VME crate communicates with the STAS controllers via CES 8210 CAMAC Branch Driver.

## 4.2 Operation of the MTD

### 4.2.1 Operation of a streamer tube chamber

A streamer tube is a gas detector operating in limited Geiger-Müller mode. Its anode wire raised to a high voltage is placed a few millimeters from the cathode and operates in a quenching gas mixture (e.g. argon+isobutane).

When a fast charged particle passes through the filling gas in a region between the anode wire and the surrounding high-resistivity cathode it produces ion pairs ( $\text{Ar}^+ + e^-$ ). The electrons drift rapidly towards the anode wire, in vicinity of which the electric field increases (approximately as  $1/R$ ), causing them to accelerate. At a distance from the wire, small compared to other lengths involved, these electrons start a chain reaction (*avalanche*): they ionize and recombine with argon ions. This leads to increase of the number of electrons and emission of UV photons that are able to further interact with gas molecules.

Growing avalanche is reducing the local electric field due to space charge created with fast moving electrons and slow, heavy ions of the gas molecules. The streamer is formed. Within a few nanoseconds large number of electrons is reaching the anode wire depositing their charge in a very small region which begins to propagate as a wave along the wire in both directions. The charge deposited on the anode wire is able to induce opposite charge locally on all nearby conductors. In case of the MTD this charge is induced in aluminum strips located above and below the streamer tube (see chapter 4.1.2).

Production of new ion-electron pairs is stopped by a virtue of quenching gases like isobutane. These heavy molecules can exchange charge and energy with argon ions and interact with electrons and UV photons without creation of new electrons. The absorbed energy is turned mainly into rotation and vibration of the molecule.

Detailed description of the operation principles of the gas detectors can be found in Ref. [97].

### 4.2.2 Event handling

The MTD is triggered by a custom-made Trigger Unit (TU) being an adapted version of TU from KASCADE Array [98]. Two trigger modes are possible: internal and external. In the internal triggering mode a multiplicity of DIGOR signals from wire boards of all towers is used.

The source of the external trigger are KASCADE/Grande components

like the KASCADE Array (for showers above  $10^{14}$  eV), Grande Array (for showers above  $10^{16}$  eV), the Top Cluster and Trigger Plane from the Central Detector, and the Piccolo.

For a shower generating only triggers in Grande Array (mostly showers far away from KASCADE centre) the delay of the trigger signal reaching the MTD becomes comparable with the length of the one-shot pulse in the front-end electronics. This creates inefficiency in muon registration in such showers.

The Trigger Unit is responsible also for generation of the Time Label (TL) for each event, with a precision of 200 ns. The TL information is used by the acquisition software to build an air shower event.

Whenever a trigger condition is fulfilled in the TU, the TVC receives an EVENT signal and a NIM-pulse is generated. The TVC locks the TU to inhibit more triggers and reads out the TL and trigger registers. The NIM-pulse is split and fed into the START inputs of all STAS modules that send a LOAD signal. The data from the comparators are moved into the shift-registers of the front-end boards. Then, clock pulses are used to shift the data along the chain into the memory of the STAS. When this is finished, the first STAS in the CAMAC crate generates a Look-At-Me (LAM) signal which is fed into an external interrupt input of a CAMAC Branch Driver to generate a VME-interrupt. This interrupt causes a high priority process of the TVC to scan all STAS and ADC modules for LAM signals and to transfer the data into the memory of the TVC. When the transfer is completed the TU is unlocked and a low priority process preprocesses the data and sends them, via a second TVC over TCP/IP, to the central event builder.

The high priority Data Acquisition Program (DAQ) [99,100] coordinates the experiment control, time and event handling and data storage. It uses routines on the TVC to initialize the hardware: the VME and CAMAC crates, the TU, the STAS controllers and the ADC modules.

In some cases, when high energy showers hit the ground close to the detector the data acquisition system saturates. The trigger is created but the number of particles reaching the MTD is high enough to create overlapping clusters. The information about these clusters is represented by a single, long string of data. STAS Controllers have a limit of allowed data size. If this string of data is longer than 512 words it is automatically rejected by the acquisition system and information about the muon tracks is lost. As a result in a shower some of the muons are missing. In extreme cases, when all STAS Controllers are in saturation, in the data there is no muons in the shower and the shower is rejected by shower selection criteria.

### 4.2.3 Reconstruction of the muon directions

General description of the reconstruction of EAS can be found in chapter 3.2. Here, the algorithm of the reconstruction of the muon directions from the hit information will be described.

From the raw data the information about signals on wires, diagonal and perpendicular strips is retrieved and converted into positions of each wire and strip. The cluster sizes along the wires and strips (in cm) are reconstructed for each detector module. The position, where the particle crossed the module is estimated as the centre of the cluster and becomes the position of a hit.

Muon directions can be reconstructed from three or two hits. The three hit tracks are reconstructed first. In a first approach the algorithm is looking for hits that are aligned, parallel to the shower axis (determined in the KASCADE-Grande Array), in three modules. The quality of the track is described with the Q parameter that behaves like  $\chi^2$ :

$$Q^2 = \sum_{i=1}^3 \frac{D_{tr}^2(Hit_i)}{A_{HIT_i}} \quad (4.2.1)$$

where  $D_{tr}$  is the distance in space between the hit and the track coordinate and  $A_{HIT_i}$  is the area of the hit (wire cluster size  $\times$  strip cluster size). The track quality Q is not a standard  $\chi^2$  because the reciprocal of the area of the hit is used as a weight of the square of the hit-track distance. The track quality cut  $Q < 2.5$  efficiently rejects accidental tracks without reducing significantly the particle track sample.

Using all possible hits for three hit tracks, the information about them is stored in a data bank. The procedure is then repeated for two hit tracks but only for hits that are not involved in three hit tracks. The hits that do not fit to any track are ignored.

At high muon densities clusters may overlap and not all tracks are reconstructed, or are reconstructed with poor quality. This reconstruction inefficiency occurs when showers fall too close to the MTD. At extreme cases none of the muon tracks is reconstructed. The minimum distance to the shower core where there is still the full reconstruction efficiency increases with shower energy.

## Chapter 5

# Selection of the experimental data

### 5.1 Selection of showers

The investigation being a subject of this work is based on over 45 million showers registered by KASCADE-Grande experiment from November 2003 to 3<sup>rd</sup> June 2009.

Selection criteria for showers in KASCADE-Grande were a subject of extended investigation. After detailed studies of the performance of the Grande Array a set of conditions, superimposed on measured and reconstructed shower parameters, was developed to obtain highest reconstruction accuracy and to minimise systematic errors.

In the MTD analysis only showers with muon tracks are taken into account. In addition showers selected for the MTD analysis fulfill the following conditions:

1. the highest energy deposit is recorded by a central detector station of a trigger hexagon (Fig. 3.1.2);
2. at least 12 stations have a signal above the discriminator threshold (i.e. provide a valid TDC-count);
3. the ratio between the detected and the total reconstructed number of particles is above a given threshold [94];
4. all Grande and KASCADE detector stations are active during the event;
5. shower zenith angle is less than  $18^\circ$ ;
6. shower age:  $-0.39 < s < 1.49$

All analyses in this thesis, where only KASCADE-Grande data have been used, are done for showers with reconstructed primary energy  $E_0$  above  $10^{16}$  eV, where KASCADE-Grande has full efficiency (Fig. 3.2.3).

The MTD registration is fully efficient in a certain distance range to

the shower core. Close to the core reconstruction efficiency is affected (see Chapter 4.2.2 and 4.2.3). At larger distances, where muon density becomes anyway smaller, the registered number of muons (and, consequently, showers with at least one muon) is further reduced by trigger inefficiency effects (see Chapter 4.2.2). This leads to the core distribution of showers available for the investigation in the MTD as shown in Fig. 5.1.1. Most of the showers are located within 192400 m<sup>2</sup> of standard KASCADE-Grande fiducial area

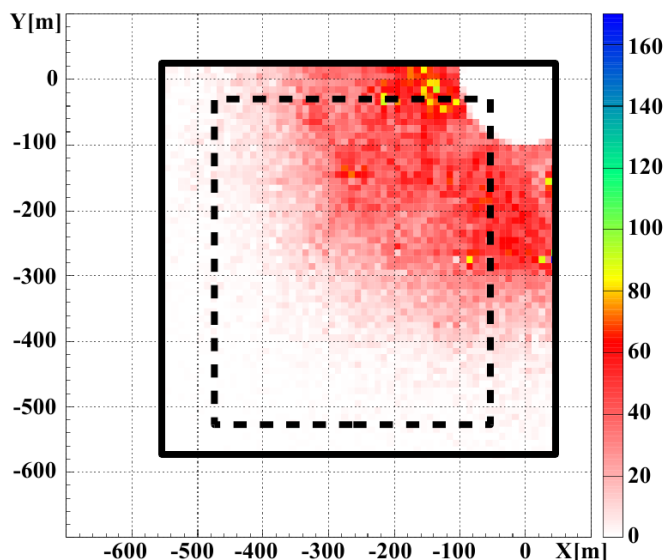


Figure 5.1.1: Shower core distribution over the fiducial area used in the MTD analysis (solid-line rectangle). The standard fiducial area (dashed-line rectangle) used in KASCADE-Grande EAS analyses is shown for comparison.

around the centre of the Grande Array (dashed-line rectangle). To improve statistics in the MTD analysis it was necessary to extend fiducial area to 319000 m<sup>2</sup> (-550 m < x < 50 m, -580 m < y < 20 m, solid-line rectangle) what increased the number of showers with muons (without any other condition) from 1676393 to 2977697. This extension, however, has no influence on the quality of reconstructed showers used in the MTD analysis.

The numbers of showers before and after applying cuts described above are given in Appendix A in Tab. A.1.

Whenever the analysis is performed in energy bins the energy is calculated with the formula based on linear combination of electron and muon sizes:

$$\lg(E[GeV]) = 0.313 \cdot \lg(N_e) + 0.666 \cdot \lg(N_\mu) + 1.24/\cos(\theta) + 0.580 \quad (5.1.1)$$

This formula was obtained by means of a linear regression analysis based on CORSIKA showers for five different primaries [101].

To stay up-to-date with the development of the KASCADE-Grande analysis of the EAS the analysis from chapters 6 to 8 was repeated for the recently developed formula (5.1.2) for the energy of the showers:

$$\begin{aligned} \lg(E[GeV]) &= [a_H + (a_{Fe} - a_H) \cdot k] \cdot \lg(N_{ch}) + b_H + (b_{Fe} - b_H) \cdot k \\ k &= \frac{\lg(N_{ch}/N_\mu) - \lg(N_{ch}/N_\mu)_H}{\lg(N_{ch}/N_\mu)_{Fe} - \lg(N_{ch}/N_\mu)_H} \end{aligned} \quad (5.1.2)$$

The formula is based on the number of charged particles, obtained with KASCADE and Grande arrays, and number of muons, obtained with KASCADE muon detectors (see Ref. [102] for details). The energy assignment is defined as  $E = f(N_{ch}, k)$ , where  $N_{ch}$  is the size of the charged particle component and the parameter  $k$  is defined through the ratio of the sizes of the charged ( $N_{ch}$ ) and muon ( $N_\mu$ ) components. The main aim of the  $k$  variable is to take into account the average differences in the  $N_{ch}/N_\mu$  ratio among different primaries with the same  $N_{ch}$ , and the shower-to-shower fluctuations for events of the same primary mass. The coefficients  $a$ ,  $b$ ,  $c$ ,  $d$  are obtained through the fits to the scatter plots ( $N_{ch}$ ,  $N_{ch}/N_\mu$ ) and ( $N_{ch}$ ,  $E$ ) in the region  $6 < \lg(N_{ch}) < 8$ , which means  $\sim 100\%$  trigger efficiency, and up to the energy for which the simulated statistics is sufficiently high.

To distinguish the energy formulas (5.1.1) and (5.1.2), the terms “ $N_e$  formula” or “ $E_0^{rec}$ ” will refer to formula (5.1.1), and terms “ $N_{ch}$  formula” or “ $E_{N_{ch}}$ ” will refer to the formula (5.1.2) if not stated otherwise. All results obtained with  $N_{ch}$  formula are presented only in the appendices B, C and D. All examples presented in the following chapters are obtained using  $N_e$  formula, if not stated otherwise.

## 5.2 Selection of muons

Standard set of parameters used in the description of muon directions obtained with the MTD contains characteristics of each hit (hit parameter array) used to calculate direction, coordinates of the point where the muon track crosses the plane of the KASCADE scintillator array (*track position*), azimuth and zenith angles of the track, and the *track pattern* (patt3 for 3-hit tracks and patt2 for 2-hit tracks), describing which modules were involved in the track reconstruction. Top, middle, bottom and wall modules are assigned to number 1, 2, 3 and 4, respectively. For example, pattern 124 means that track was reconstructed out of hits in the top, middle and wall modules. In the following analysis only tracks with patterns 123, 124, 423 for 3-hit and 12, 23, 13, 14, 24, 42, 43 for 2-hit ones are taken into account.

The direction of a muon is reconstructed from the hits in detector modules. To select high quality tracks it was necessary to investigate dimension of each hit along wires (x axis – wire cluster size) and perpendicular strips (y axis – strip cluster size) and the *hit area*, being a product of those two.

When a muon is accompanied by other particles, very often passing through the module they create large clusters, at least in one module, and the most penetrating particles create hits in the last module. Muon direction based on large clusters is not as accurate as the one based on small clusters and should be eliminated from the analysis. That is why for the analyses based on muon directions hits with the wire cluster size restricted up to 5 cm and with the strip cluster size up to 10 cm are taken into account, only. Additionally, the area of the last hit in a track must be smaller than the area of other hits used to reconstruct that track.

Due to the reconstruction inefficiency effects it was necessary to restrict the muon-to-shower-axis distance  $R_\mu$ , calculated from shower core position and shower direction obtained with Grande Array and the track position in the shower coordinate system, to be larger than 100 meters.

The following list summarises the conditions for muon track selection:

1. patt3= 123,124, 423;
2. patt2= 12, 23, 13, 14, 24, 42, 43;
3.  $100 \text{ m} < R_\mu < 700 \text{ m}$ ;
4. wire cluster size  $\leq 5 \text{ cm}$ ;
5. strip cluster size  $\leq 10 \text{ cm}$ ;
6. hit area in the last hit used to reconstruct the track is the smallest one.

In Tab. A.1 the numbers of muon tracks before and after applying cuts described in this chapter are listed.

### 5.3 Analysis of the simulated data

EAS were simulated with CORSIKA. In a standard KASCADE-Grande simulations QGSJet-II or EPOS are high-energy (HE) hadronic interaction models and FLUKA is the low-energy (LE) interaction model. Showers were simulated for H, He, C, Si and Fe primaries with the spectrum  $\sim E^{-2}$  in the energy range from  $10^{14} \text{ eV}$  to  $10^{18} \text{ eV}$  and in the zenith angle range  $0^\circ - 42^\circ$ . These simulations will be called “the standard set of simulations”.

There are also available special simulations, where showers have energy up to  $3.16 \times 10^{18} \text{ eV}$  or zenith angle up to  $70^\circ$ , or showers are distributed over different area than the standard  $1.5 \times \text{area-of-the-Grande-Array}$ . These simulations will be called “the special set of simulations”.

Numbers of showers available for the analysis and number of reconstructed muon tracks are summarised in Tab. A.1.

In the following text, “QGSJetII” refers to QGSJet-II-2 version of the HE hadronic interaction model, “EPOS” refers to EPOS 1.99 version of the HE hadronic interaction model. “FLUKA” refers to FLUKA2002.4 version of LE hadronic interaction model used in combination with QGSJetII, and FLUKA2008.3 in combination with EPOS, if not stated otherwise.

It takes several weeks of computing time on a large, powerful computer farm (available at KIT) to simulate with CORSIKA one set of EAS for a single primary particle and one high-energy model. To increase the number of showers available for comparisons with the experimental data each simulated shower is used then several times. The core position of the shower is randomly distributed 10 times over an area 1.5 times larger than the area of the experiment, and detector responses are simulated. Obtained set of data is then processed with KRETA in the same way as it is done with the experimental data.

In the standard simulation set, due to the location of the MTD within the experiment and relatively small detection area, as well as the higher muon energy threshold, the number of events with muon tracks was too small for statistically significant comparisons of the experimental and simulated data. To overcome this problem and to lessen the bias in parameter values created by multiple use of CORSIKA simulated showers a special set of proton and iron initiated showers was created with QGSJetII+FLUKA model combination. Showers were simulated only up to  $20^\circ$  in zenith angle and each shower was in the detector simulations used 5 times only over the fiducial area used in the MTD analysis. This increased the number of simulated events for our analyses significantly (see Tab. A.1). These simulations will be called “the special MTD set of simulations”.

One would require similar set of simulations (preferably special MTD ones) for the EPOS+FLUKA model combination to be able to test with the MTD data also these models. However, due to simulation priorities in the KASCADE-Grande collaboration, only standard set, one set of special (with high energy showers) and a fraction of special MTD set of simulations were available for the analysis (Tab. A.1). Therefore, only very general conclusions on the quality of EPOS in reproducing the MTD data were possible.

The simulations are performed with the slope of the energy spectrum equal to -2 to increase the number of high energy showers. Analysis presented in this work is done in the energy range above the Knee, that is where the all-particle CR spectrum is described with the spectral index  $\gamma \approx -3.1$ . To match the slope of the spectrum of the detected and simulated showers muons from each simulated shower are weighted with the energy dependent factor<sup>1</sup>.

In the following analysis, the selection of simulated showers and muons is identical as for the measured data, and is done with the reconstructed parameters. Additionally, all simulated showers fulfill the “software trigger” condition that at least 10 stations in the outer clusters of the KASCADE Array have signal from charged/ $\gamma$  detectors above the threshold. This condition is an equivalent of trigger condition present in measured data.

---

<sup>1</sup> The factor is  $(E_{true}/10^6)^{-1.1}$  where  $E_{true}$  is the true energy of a simulated shower in GeV.

## Chapter 6

# Lateral muon density distributions

The lateral distributions of particle density are one of the most important shower characteristic of EAS reconstructed from the response of ground based detector arrays and they are a starting point for the investigation of energy and mass composition of cosmic rays. Their shape reflects the longitudinal development of particle cascade in the atmosphere. When compared with simulations, it is a powerful tool that helps to cross-check and improve our understanding of the development of each particle component of a shower and provide valuable information about the performance of the detectors. The design of the KASCADE-Grande experiment allows to obtain lateral distributions of all three components of EAS on an event basis at different energy thresholds [103].

In this chapter the lateral muon density distributions obtained for the first time with the tracking detector in a wide range of distances from the shower core are presented. The results from the MTD are compared with lateral distributions obtained with KASCADE Array and simulations, in four primary energy ranges.

### 6.1 Data selection and analysis

The selection of showers was performed with the standard set of cuts described in Chapter 5.1. The lateral density distributions of muons were obtained with all muons which direction was reconstructed from the two and three hit tracks that fulfill all selection conditions (Chapter 5.2) but conditions on cluster sizes of the hits and their relation (conditions 4, 5 and 6 in the list).

The geometry of an exemplary shower event is shown in Fig. 6.1.1. The vertical shower hits the ground in Grande Array. The core position, direction and other parameters are reconstructed with the information from

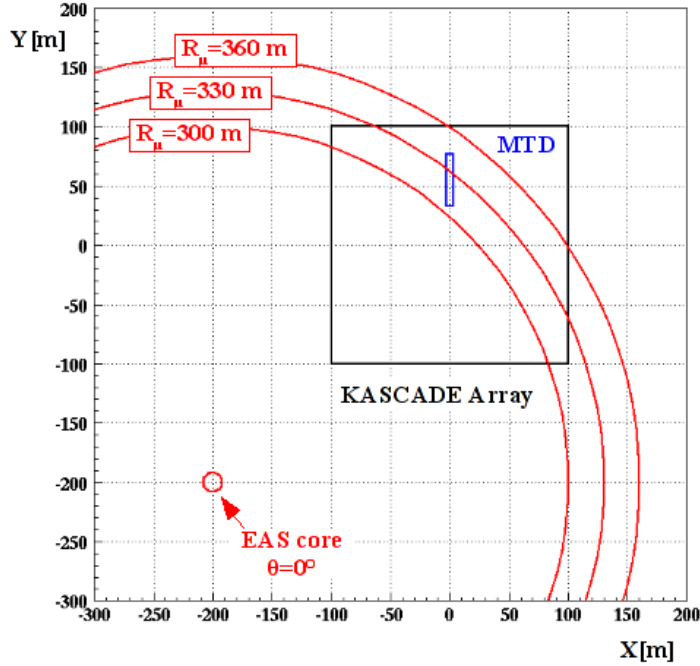


Figure 6.1.1: Distance between the muon track and shower axis  $R_\mu$  is divided into 30 m bins. In each bin number of muon tracks and area of the MTD are calculated.

arrays of charged particles and muon detectors. To obtain the lateral distributions of muon registered in the MTD the following procedure was applied:

1. For each shower, the distance  $R_\mu$  was divided into 30 m-large radial bins around the reconstructed shower core position.
2. In each distance bin, the number of muons was calculated using position of the middle hit in 3-hit tracks or extrapolation of the position of the hit to the level of the middle module in 2-hit tracks.
3. The calculation of the area of the detector in each distance bin is done in a following way. In a standard set of data taking two neighbouring wires are combined. With perpendicular strip they create a  $2\text{ cm} \times 2\text{ cm}$  cell that is a basic detection area in the module. With the positions of wires and strips, location of each cell is calculated and its size added to detector area contained in the particular  $R_\mu$  bin. The area was corrected for the zenith angle of a shower multiplying it by a cosine of this angle.

The number of reconstructed muon tracks may be distorted by the data acquisition and/or trigger inefficiencies (Chapter 4.2). As a result, one can obtain no tracks in a distance bin where the size of the detector area there, and the registered muon density in the neighbouring bin make the zero-

track registration highly improbable. Therefore, it was necessary to impose an additional condition on the way of calculating the area in each distance bin. For the muon density calculations only the area in distance bins where at least one muon track was reconstructed was taken into account. Such an approach is equivalent of the case of having different active detector area for each shower. Without this condition the detector area without muons would be accumulated and calculated density of muons would be biased towards lower values.

The number of muon tracks in each distance bin was corrected for the reconstruction efficiency  $\epsilon$ . The calculation of the track reconstruction efficiency is based on the assumption that 2-hit tracks are the 3-hit tracks with one hit missing and all modules are equally efficient in creating a hit. This assumption leads to the following formula [104]:

$$\epsilon = \frac{1}{1 + \frac{N_{tr2}}{3 \cdot N_{tr3}}} \quad (6.1.1)$$

where  $N_{tr2}$  and  $N_{tr3}$  are two and three hit tracks, respectively.

In the reconstruction procedure 2-hit and 3-hit tracks are not independent, therefore it was necessary to introduce a proper correction factor  $\mathcal{K}$  given by the formula:

$$\mathcal{K} = \frac{1}{3 \cdot \epsilon^3 + 2 \cdot \epsilon^2} \quad (6.1.2)$$

The density in each distance bin was calculated as a sum of all muons from all showers corrected for reconstruction efficiency being divided by detector area in that distance bin corrected for zenith angle ( $A_{MTD}$ ).

$$\rho_i = \frac{\sum_{k=1}^{N_s} (N_{tr2}^k + N_{tr3}^k) \cdot \mathcal{K}}{\sum_{k=1}^{N_s} A_{MTD}^{k,i}} \quad (6.1.3)$$

where  $i$  is distance bin number,  $N_s$  is number of showers,  $A_{MTD}^{k,i}$  is detector area in  $i^{th}$  distance bin for  $k^{th}$  shower.

## 6.2 Results and discussion

The MTD results, being based on muon counting, obtained for the first time at these energies and for such large distance range, are presented in Fig. 6.2.1 by full and empty circles. These distributions are compared with lateral density distributions based on number of muons reconstructed out of energy deposits in shielded plastic scintillators in the KASCADE Array. Preliminary results were presented at the European Cosmic Ray Symposium in 2008 [105], the International Cosmic Ray Conference [106] and DPG Spring Meetings [107, 108].

In Fig. 6.2.1 the lateral muon density distributions are presented in

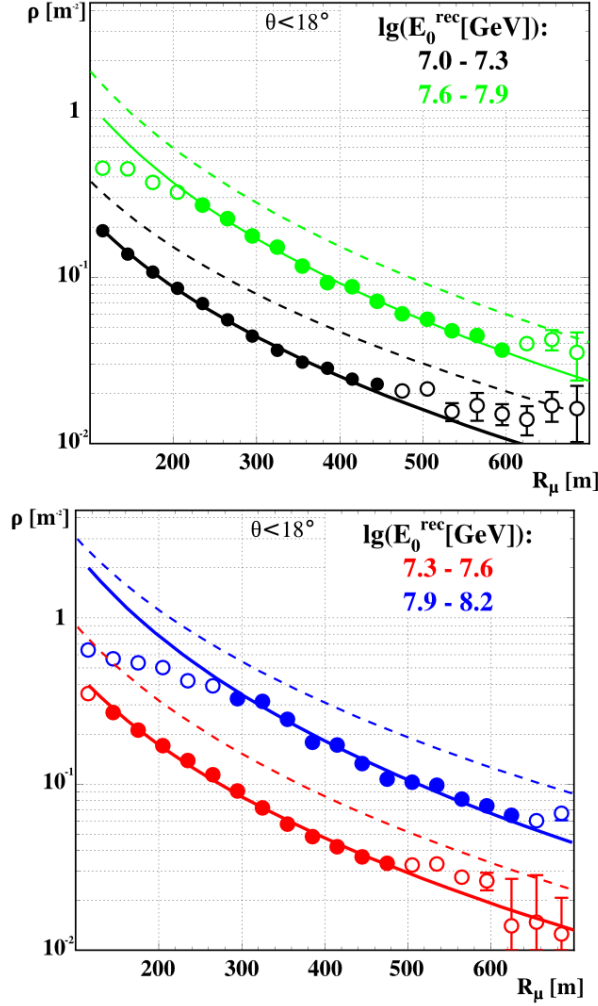


Figure 6.2.1: Lateral density distributions of muons from the MTD in four energy bins. Lines are fits to the muon density distributions obtained with the MTD (solid lines, points used in the Lagutin fit are marked with full symbols) and muon density distributions obtained with the KASCADE Array of shielded plastic scintillators (dashed lines).

four energy bins calculated with the  $N_e$  formula (5.1.1)<sup>1</sup> from  $10^{16}$  eV to  $1.6 \times 10^{17}$  eV and in muon-to-shower-axis distance range from 100 to 700 meters. For better visibility, the KASCADE Array muon distributions are represented by fits, only (dashed lines).

Lateral density distributions are fitted with Lagutin-like function (3.2.4)

<sup>1</sup>Results obtained for the energy bins calculated with the  $N_{ch}$  formula are in Appendix B.

given by the formula:

$$\rho(r) = N_\mu \cdot \frac{0.28}{r_0^2} \left(\frac{r}{r_0}\right)^{-0.69} \left(1 + \frac{r}{r_0}\right)^{-2.39} \left(1 + \left(\frac{r}{10 \cdot r_0}\right)^2\right)^{-1} \quad (6.2.1)$$

In this analysis the fitted parameters are  $r_0$  and the scaling factor  $N_\mu$  of the distribution. The results of the  $r_0$  fits are presented in Tab. 6.1.

In all energy bins the separation in measured muon density between MTD-muon and KASCADE-Array-muon density distributions corresponds to the values expected from simulations for the two muon energy thresholds (800 MeV and 230 MeV).

In Fig. 6.2.1 the experimental MTD-points used in the fits are marked with full symbols. As we see, in all energy intervals the MTD-muon distributions can be fitted with the function (6.2.1) only in a limited and different muon-to-shower distance range. To discuss the observed deviations of the experimental points from the fit-lines at small and large distances Fig. 6.2.2 has been constructed. There, the lateral muon density distributions are pre-

Table 6.1: Results of the fits of the lateral density of muons in energy range  $10^{16}$  eV– $10^{17}$  eV.

$lg(E_0^{rec}[GeV])$ range	$\langle E_0^{rec} \rangle$ [ $10^7$ GeV]	KASCADE		MTD	
		$r_0[m]$	$\chi^2/NDF$	$r_0[m]$	$\chi^2/NDF$
7.0 - 7.3	$1.340 \pm 0.001$	$402 \pm 9$	20/10	$345 \pm 3$	190/10
7.3 - 7.6	$2.689 \pm 0.005$	$280 \pm 10$	49/10	$300 \pm 4$	260/10
7.6 - 7.9	$5.34 \pm 0.02$	$260 \pm 15$	18/10	$243 \pm 7$	53/11
7.9 - 8.2	$10.41 \pm 0.06$	$306 \pm 27$	46/10	$207 \pm 14$	18/10

sented in the first and the last analysed energy bin and the uncertainty of each density point is multiplied by a factor 10 to show the changes of the shower and muon statistics discussed in the following text.

In the first energy bin, the MTD distribution can be fitted with Lagutin function in the distance range from 100 meters to 450 meters, thus being compatible with the KASCADE distribution in this distance range. At larger distances the MTD distribution is rising as well as the uncertainty of the density values. In the last energy bin, the MTD distribution can be fitted with Lagutin function in the distance range from 280 meters to 640 meters, thus being compatible with the KASCADE distribution in this distance range. In distances outside this range the MTD distribution is lower (<280 meters) or higher (>640 meters) than predicted by the Lagutin function, and the uncertainties of the densities are increasing.

The shape of the MTD muon density distributions at large distances is caused by the changes in the population of showers with muon tracks,

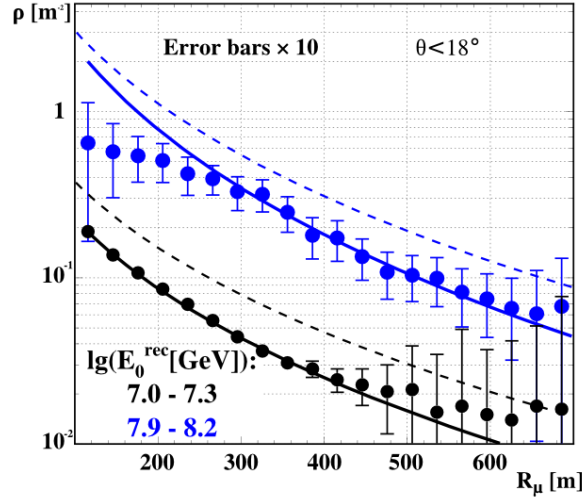


Figure 6.2.2: Lateral density distributions of muons from the MTD in the first and the last energy bin; the error bars of each point are multiplied by factor 10. Lines are fits to the muon density distributions obtained with the MTD (solid lines) and muon density distributions obtained with the KASCADE Array of shielded plastic scintillators (dashed lines).

reconstructed with the MTD, in that distance range. With rising  $R_\mu$  distance, the number of showers that stem from lower-energy, light-primary CR is decreasing because these showers cannot create an efficient trigger in KASCADE or Piccolo Array due to the low density of charged particles in EAS cascade<sup>2</sup>. In that case the information about the tracks of muons from the MTD is lost (see Chapter 4.2.2). On the other hand, the showers initiated by low-energy, heavy primary are able to create efficient triggers and information about muon tracks can be recorded. The density of particles is rising due to the larger number of reconstructed muon tracks from heavy showers.

The behaviour of the MTD density distributions at small muon-to-shower distances is influenced by the saturation of data acquisition system and/or limited track reconstruction efficiency (see Chapters 4.2.2 and 4.2.3). The reconstructed number of muon tracks is decreased while the determination of the detector area is not affected, thus the muon density is decreasing.

The influence of the shower population and its behaviour with the distance and energy is confirmed by the investigation of  $\lg(N_\mu)/\lg(N_e)$  ratio used in  $\langle \ln A \rangle$  investigation and the behaviour of the lateral pseudorapidity distribution, both discussed in Chapter 8.

<sup>2</sup>see Chapter 1.3.4 about dependence between CR primary, its energy and content of particles within EAS cascades

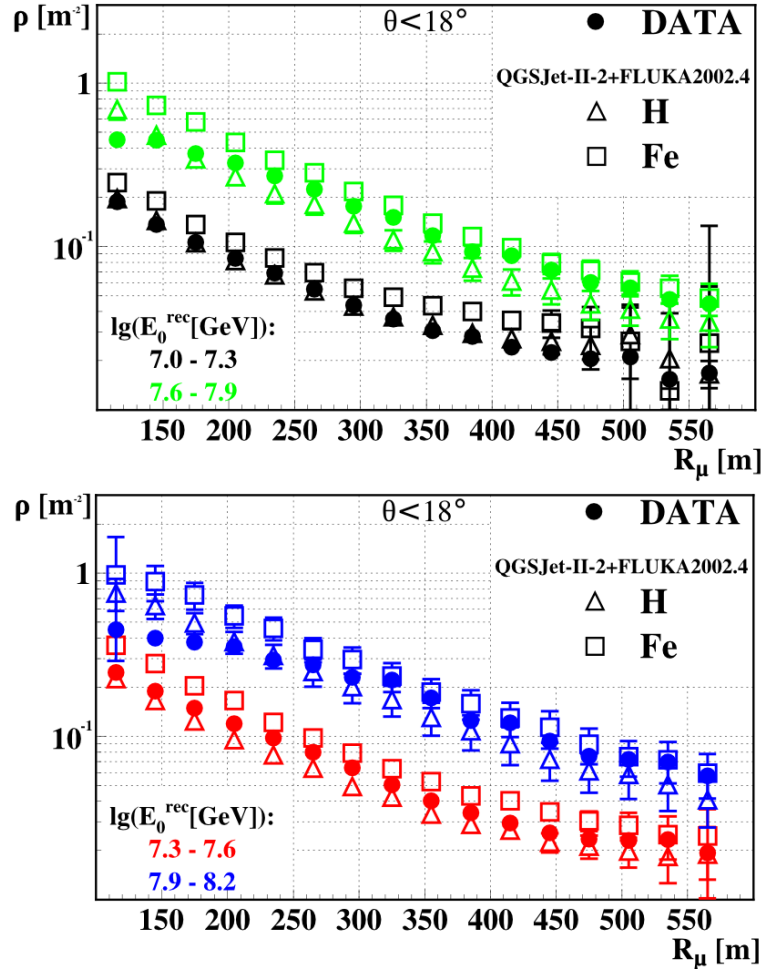


Figure 6.2.3: Lateral muon density distributions obtained with the MTD measurements (solid symbols) and CORSIKA simulations (open symbols) in four energy ranges.

In Fig. 6.2.3 the comparison of the MTD-muon density distributions with the results for H and Fe initiated showers simulated with CORSIKA (QGSJetII+FLUKA) is shown. In all energy bins presented distributions are in good agreement with each other within error bars. However, in the distance range up to 200 m (clearly visible in the 3<sup>rd</sup> and 4<sup>th</sup> energy bin) the densities from simulations are higher than densities from the measurement. This is due to the idealised description of the MTD in CRES (see Chapter 2.2) that “fails” in reproducing the detector behaviour in extreme cases when saturation of the data acquisition occurs.

It is important to notice that directions of muons that originate from

---

showers that are closer than 200 m or farther than 400 m are of acceptable quality and are useful for calculation of other parameters like pseudorapidity. Selection of muons, applied to other presented investigations, is motivated by other physics questions than behaviour of muon densities.

## Chapter 7

# Pseudorapidity of muons in EAS

In KASCADE-Grande EAS experiment, combining information about shower direction, obtained with detector arrays, with information about muon directions, obtained with muon tracking detector, it is possible for the first time to investigate pseudorapidity of high-energy hadronic interactions in forward kinematic region in energy range not accessible for man-made accelerators.

Pseudorapidity was devised to describe particle interactions in the accelerator experiments and is expressed by a function of an angle between the direction of produced particle and the direction of the beam. It is a high energy approximation of rapidity, the quantity that is related with the energy and momentum of the particles created in the interaction. In EAS experiment, the shower axis is equivalent of the beam and muons are particles carrying information about the particles that stem from HE hadronic interactions being essential for the development of EAS. Muon tracks in an air shower are, in general, not coplanar with the shower axis, thus for investigation of the angle between the muon track and shower axis a concept of radial and tangential angles was developed. With these two observables it is possible to investigate the muon momentum components in the shower.

In this chapter, the radial and tangential angles will be introduced. Results of the pseudorapidity investigation, derived from these two angles, in terms of model testing will be presented.

### 7.1 Radial and tangential angle

The MTD is able to reconstruct the directions of EAS muons with high accuracy. Combining this information with very accurate estimation of the shower core position and arrival direction it is possible to describe arrival pa-

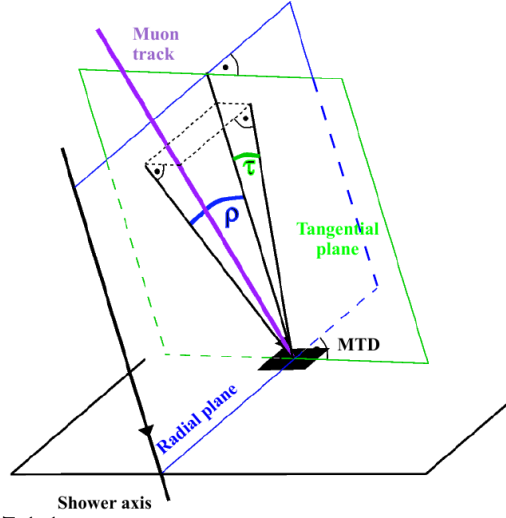
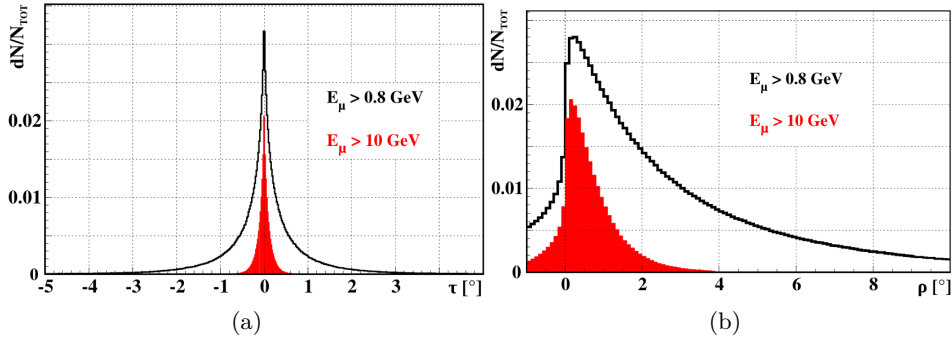
Figure 7.1.1: Definition of radial ( $\rho$ ) and tangential ( $\tau$ ) angles.

Figure 7.1.2: Tangential angle (panel (a)) and radial angle (panel (b)) distributions of muons for two muon energy thresholds. Muons stem from Hydrogen initiated, vertical showers with energy  $10^{16}$  eV simulated with CORSIKA using QGSJet-II-2+FLUKA2008.3. Distributions normalised to the total number of particles in distribution with lower energy threshold.

rameters of EAS muons in terms of *radial* ( $\rho$ ) and *tangential* ( $\tau$ ) angles [109]. Both angles are defined in Fig. 7.1.1. The radial angle and tangential angle are angles between the shower direction and the orthogonal projections of the track onto the radial and tangential plane, respectively. The radial plane is defined by the position of the detector and the shower axis. The tangential plane is the plane parallel to the shower axis at the position of the detector and perpendicular to the radial plane. Typical distributions of radial and tangential angles are shown in Fig. 7.1.2.

The radial angle is dominated by the transverse momentum of muon parents (Fig. 7.1.3), mostly  $K$  and  $\pi$  mesons. The tangential angle is domi-

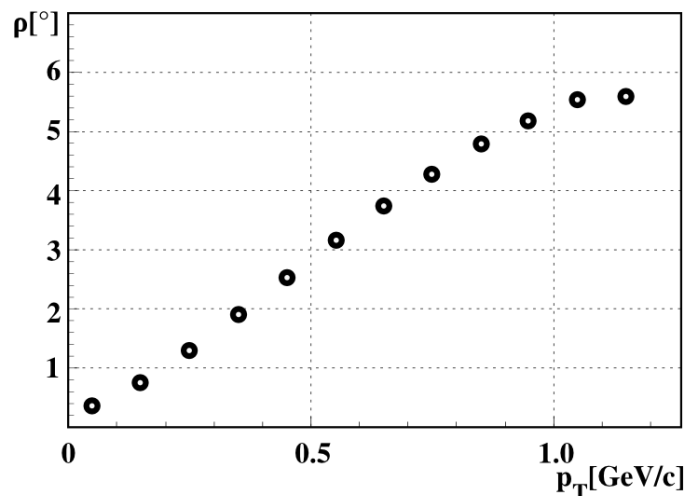


Figure 7.1.3: Radial angle of muons as a function of  $p_T$  of parent hadrons. Muons stem from Hydrogen initiated, vertical showers with energy  $10^{16}$  eV simulated with QGSJet-II-2+FLUKA2008.3.

nated by the amount of muon scattering in the atmosphere and absorber or detector material, together with a possible displacement of the muon production place from the shower axis. Distribution of this angle is symmetrical around zero and becomes narrower with increase of muon energy as muons with higher energy exhibit less scattering on their path from place of origin to the detector (Fig. 7.1.2a). The radial angle carries information about the transverse momentum of the parent hadrons and similar narrowing of the radial angle distribution with increase of the muon energy can be observed (Fig. 7.1.2b).

The behaviour of the angles with the muon-to-shower-axis distance  $R_\mu$  is a consequence of lateral distribution of energy of the EAS muons. The mean radial angle is increasing with the  $R_\mu$  as the muon energy is decreasing and lower energy particles are scattered more on their way to the observation level.

Radial and tangential angles are parameters used to calculate the pseudorapidity and mean production height of muons in a shower [110].

## 7.2 Pseudorapidity

The rapidity is defined by

$$y = \frac{1}{2} \ln \frac{E + p_z}{E - p_z} = \ln \left( \frac{E + p_z}{m_T} \right) = \tanh^{-1} \left( \frac{p_z}{E} \right) \quad (7.2.1)$$

where  $E$  is an energy of a particle,  $m_T$  is its transverse mass given by

$$m_T = m^2 + p_x^2 + p_y^2 \quad (7.2.2)$$

and  $p_z$  is particle momentum along  $z$ -axis (usually the beam direction). When  $p \gg m$  rapidity  $y$  may be expanded to obtain pseudorapidity  $\eta$ :

$$y = \frac{1}{2} \ln \frac{\cos^2(\theta/2) + m^2/4p^2 + \dots}{\sin^2(\theta/2) + m^2/4p^2 + \dots} \approx -\ln(\tan(\theta/2)) \equiv \eta \quad (7.2.3)$$

where  $\cos(\theta) = p_z/p$ . The  $\eta$  defined in such a way (right side of equation (7.2.3)) is approximately equal to the rapidity  $y$  for  $p \gg m$  and  $\theta \gg \gamma^{-1}$ . The pseudorapidity can be used when it is possible to measure angle of the particle with respect to the beam but not its energy and momenta.

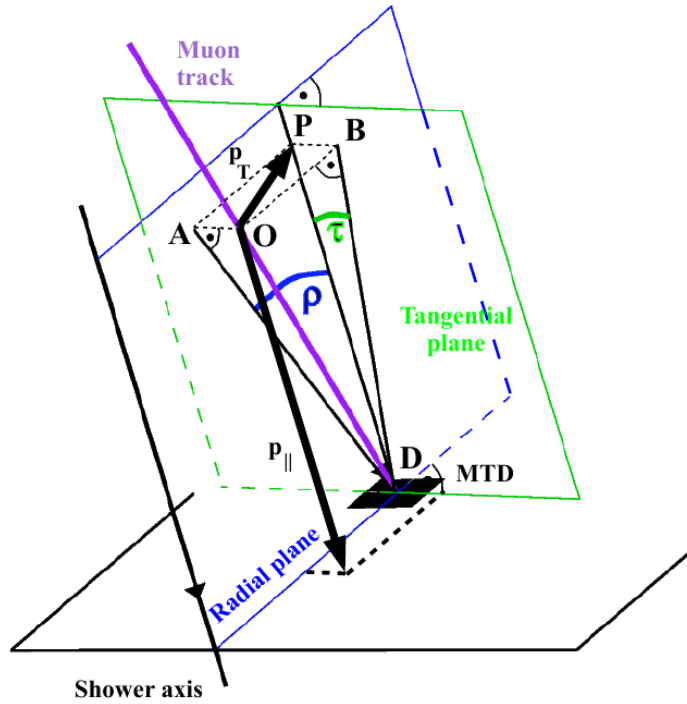


Figure 7.2.1: Muon track described in terms of the muon momentum, see text for explanation of the dependence between radial and tangential angles and components of the muon momentum.

Using simple trigonometry (depicted in Fig. 7.2.1) and substituting tangent for an angle, which is correct within 5% error up to 0.4 radian, one can write the following expressions for  $\tau$  and  $\rho$ :

$$\tau \approx \frac{PB}{PD} = \frac{p_T}{p_{||}} \times \sin(POB) \quad (7.2.4)$$

$$\rho \approx \frac{PB}{PD} = \frac{p_T}{p_{||}} \times \cos(POB) \quad (7.2.5)$$

Let us define the new parameter  $\zeta$  as follows:

$$\zeta \approx \sqrt{\tau^2 + \rho^2} = p_T/p_{||} \quad (7.2.6)$$

which is valid for  $\tau \leq 0.4$  radian, and  $\rho \leq 0.4$  radian. In EAS experiment, reconstructing direction of showers and directions of muons and calculating  $\rho$  and  $\tau$ , by means of  $\zeta$  one gets the possibility to investigate the muon momentum space and muon rapidities. Substituting momentum for the total energy, which is allowed above 1 GeV without significant error, one can express rapidity  $y$  and pseudorapidity  $\eta$  using parameter  $\zeta$  as follows:

$$y = \frac{1}{2} \ln \frac{E + p_z}{E - p_z} = \frac{1}{2} \ln \frac{\sqrt{(\zeta^2 + 1) + 1}}{\sqrt{(\zeta^2 + 1) - 1}} \quad (7.2.7)$$

$$\eta = \ln \frac{2 \times p_{\parallel}}{p_T} \approx -\ln \frac{\zeta}{2} \quad (7.2.8)$$

As simulations show, the shape of muon pseudorapidity distribution on ground follows the shape of distribution of their parent hadrons rapidity [111] (Fig. 7.2.2). This close relation is specially interesting in context of the development of high-energy interaction models because investigating pseudorapidity of muons we have an insight into interactions from which originate their parent particles.

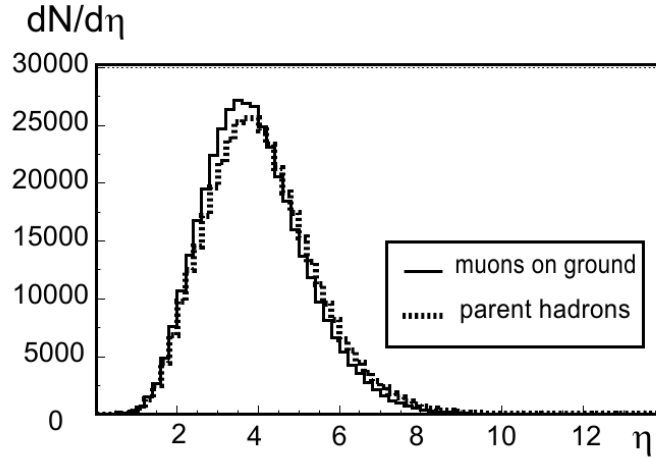


Figure 7.2.2: Simulated pseudorapidity of EAS muons on ground compared with rapidity of their parent hadrons, from Ref. [111].

### 7.3 Shower and muon selection

Showers selected for this analysis fulfill general conditions for showers and muon tracks described in Chapter 5.1 and 5.2 for measured data and Chapter 5.3 for simulations. Additionally, to restrict the error of pseudorapidity calculated from  $\rho$  and  $\tau$  angles it is necessary to introduce another condition

on these angles:

$$-0.5^\circ < \rho < 23^\circ \wedge |\tau| < 23^\circ \quad (7.3.1)$$

which is a results of applied method (see Chapter 7.2) and finite accuracy of the reconstruction of the angle. Condition  $-0.5^\circ < \rho$  helps to include into the analysis muon tracks with small  $\rho$  that were reconstructed with negative angle due to finite angle reconstruction accuracy.

To test interaction models efficiently, it is important to investigate the optimal conditions (muon-to-shower distance, radial and tangential angle cuts) that select muons from the data that in EAS simulation stem from interactions described by the model which is investigated. Here, the results of this investigation with use of showers simulated with CORSIKA will be presented. Analysed vertical shower were simulated with QGSJet-II-2 and EPOS 1.99, both with FLUKA 2008.3<sup>1</sup>.

### Investigation of $R_\mu$ range

In EAS, muons that originate from low energy interactions, exhibit stronger scattering, thus at the observation level are spread at larger muon-to-shower-axis distance than high energy muons and have larger radial and tangential angles. Restricting angles and  $R_\mu$  distance it is possible to select muon sample that is enriched in muons that stem from high energy interactions simulated with high energy hadronic interaction model. This is straightforward conclusion from dependence of the tangential and radial angle with energy (see Fig. 7.1.2). Additionally, with CORSIKA simulations it is possible to estimate what is the influence of angle cuts onto the number of muons that stem from high and low hadronic interactions.

The results of investigations of the lateral distributions of muon number in rapidity distribution that stem form high-energy and low-energy hadronic interaction models is depicted in Fig. 7.3.1. Presented distributions are obtained with vertical showers, initiated with H and Fe primaries with energy  $E_0=10^{16}$  eV. Showers were simulated with QGSJetII+FLUKA (panel 7.3.1a) and EPOS+FLUKA (panel 7.3.1b) model combinations.

The most convenient distance range to investigate high-energy interaction models is up to 100 meters from the shower core where muons that originate from these interactions dominate in the rapidity distribution over muons from low-energy interactions. However, this distance range has to be excluded from the MTD analysis due to problems with data acquisition saturation and problems with reconstruction of muon tracks (see discussion of lateral density distribution of muons in Chapter 6.2). In the more suitable

---

<sup>1</sup> For the purpose of **this section** the models will be referred to as “QGSJetII” or “EPOS” with “FLUKA”.

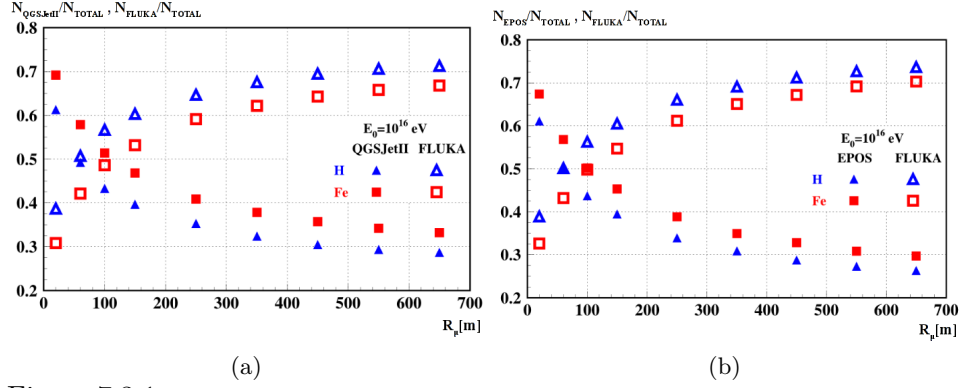


Figure 7.3.1: Lateral distributions of relative number of muons that stem from particles simulated with HE (QGSJetII in panel (a) and EPOS in panel (b)) hadronic interaction models and LE hadronic interaction model (FLUKA) relative to the total number of muons in rapidity distributions. Distributions obtained from vertical showers initiated by H and Fe primary of energy  $10^{16}$  eV. The radial and tangential angle of muons is restricted by condition (7.3.1).

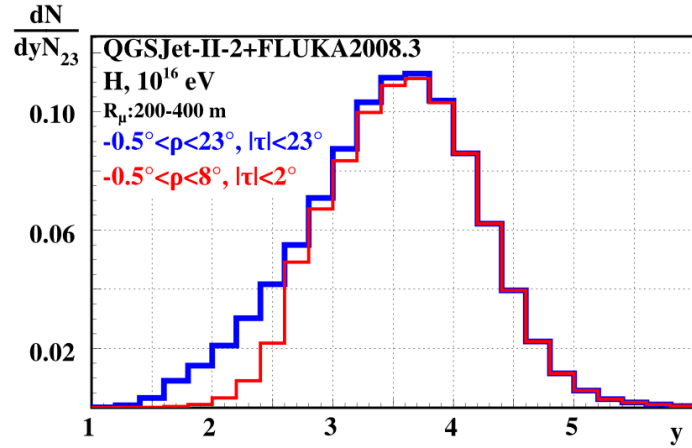


Figure 7.3.2: Influence of radial and tangential angle cut on rapidity distribution of muons from vertical, H initiated showers with energy  $10^{16}$  eV simulated with QGSJetII+FLUKA. See text for explanation.

distance range, from 200 to 500 meters, e.g. for proton showers, the number of muons that stem from interactions simulated with QGSJetII is changing from  $\sim 35\%$  to  $\sim 30\%$  and EPOS model nearly in the same range from  $\sim 33\%$  to  $\sim 27\%$ .

Selecting distance range it is necessary to consider not only content of muons that stem, in simulated showers, from high-energy interactions but also the changes of the population of heavy and light shower with the  $R_\mu$  distance and shower energy. Details of this investigation will be presented

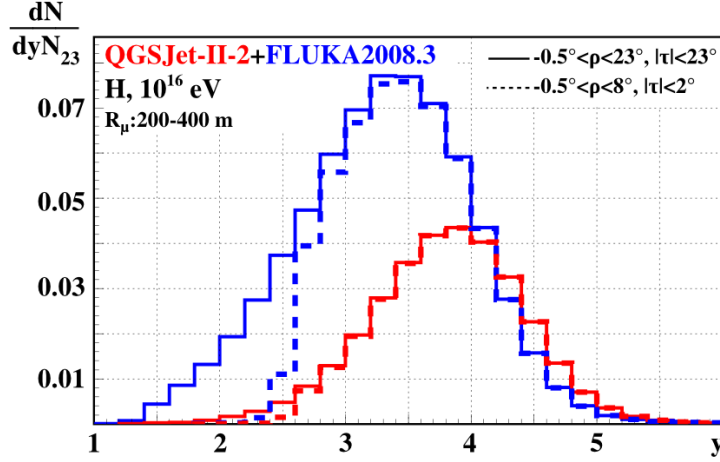


Figure 7.3.3: Example of influence of radial and tangential angle cut on rapidity distribution of muons from vertical, H initiated showers with energy  $10^{16}$  eV simulated with QGSJetII+FLUKA. The influence of the angle cuts are presented separately for low and high energy interaction model. See text for explanation.

in Chapter 8.1. The final result is that the pseudorapidity distributions are analysed in energy dependent distance range not closer than 250 meters and not farther than 520 meters.

### Investigation of angle cuts

In Fig. 7.3.2 and 7.3.3 the shapes of rapidity distribution for two radial and tangential cuts are shown. The distributions are normalised to the total number of muons in combined  $\eta$  distribution ( $N_{23}$ ) obtained with condition (7.3.1). After the angle cuts the distribution obtained with low-energy muons is changed significantly (left slope), the number of muons with low rapidity is reduced, thus the mean  $\eta$  of the distribution is shifted towards higher values.

In Fig. 7.3.3 the distributions of muon rapidity obtained with low and high-energy interaction model is shown separately to show the change in the shape of the distribution when applying two  $\rho$  and  $\tau$  cuts. All distributions are normalised to combined number of muons in rapidity distribution under condition (7.3.1). Here, the number of muons is  $\sim 14\%$  in FLUKA distribution and  $\sim 3.5\%$  in QGSJetII distribution smaller after applying the stronger angle cut (dashed distributions) and the mean value of rapidity is 5% higher for FLUKA and 1.1% higher for QGSJetII distributions. The shape of the FLUKA distribution is changed: most of the muons with  $y < 2.5$  are eliminated and number of muons with  $2.5 < y < 3.5$  is reduced. In the QGSJetII distribution only number of muons with  $y < 2.5$  is reduced.

Applying even stronger cuts on  $\rho$  and  $\tau$  would decrease the number of muons that stem from low-energy interactions but this would decrease the statistics of muons significantly and pseudorapidity distributions would be distorted by shower-to-shower fluctuations<sup>2</sup>. The radial and tangential angle condition

$$-0.5^\circ < \rho < 8^\circ \wedge |\tau| < 2^\circ \quad (7.3.2)$$

provide enough statistics to limit influence of the shower fluctuations in data and simulations.

## 7.4 Tests of interaction models with pseudorapidity distributions

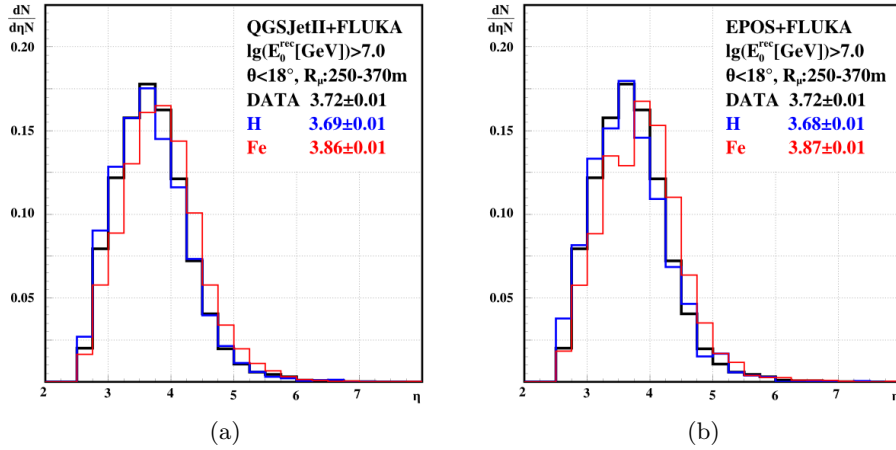


Figure 7.4.1: Pseudorapidity distributions (normalised to integral) from data and H and Fe initiated showers simulated with QGSJetII+FLUKA (panel (a)) and EPOS+FLUKA (panel (b)). Muons from showers with zenith angle up to  $18^\circ$  and  $\lg(E_0^{rec} [GeV]) > 7.0$ , collected from  $R_\mu$  range of 250-370 meters.

An example of  $\eta$  distributions for measured showers with  $\theta < 18^\circ$  and  $\lg(E_0^{rec} [GeV]) > 7.0$  compared with simulated results for two primary particles H and Fe, are shown in Fig. 7.4.1. In Fig 7.4.1a simulations employed QGSJetII+FLUKA model combination in CORSIKA and in Fig. 7.4.1b – EPOS+FLUKA. The data distribution is compared with distributions from H and Fe initiated showers ( $\theta < 18^\circ$ ). The same distributions together with the distributions from other energy ranges and for  $N_{ch}$  formula are in Appendix C.

The pseudorapidity distributions from simulations reproduce general

<sup>2</sup> Investigated condition  $-0.5^\circ < \rho < 8^\circ \wedge |\tau| < 0.7^\circ$  decreased the number of muons in data by factor 2 compared to condition (7.3.2), reducing the quality of the distributions.

shape of the data distribution well, the data are bracketed by simulations in nearly all investigated  $\eta$  bins. The mean value from data distribution is between mean values from simulated distributions (taking into account the errors of the mean values).

As simulations show, for  $\eta > 4.0$ , the muon sample contains mostly muons that stem from HE interaction model. Muons with lower  $\eta$  are predominantly from interactions simulated with low-energy hadronic interaction model but high-energy hadronic interaction model provides input particles, thus low pseudorapidity region reflects the behaviour of the latter. Comparing data and simulations in  $\eta > 4.0$  range it is possible to draw some conclusions about high-energy hadronic interaction model. In Fig. 7.4.1a the behaviour of QGSJetII model is presented: the data are between proton and iron results but closer to proton than expected from investigation of CR mass composition in this energy range (see Ref. [18]). The investigation of pseudorapidity distribution in view of model tests is closely related to the mean logarithmic mass investigation (see Chapter 8). In case from Fig. 7.4.1a one would expect that in this energy range data would be closer to iron than to proton distribution. The observed discrepancies indicate that in simulations with QGSJetII muons have larger mean pseudorapidity than observed experimentally. For the case of EPOS model (Fig. 7.4.1b) the very limited available shower statistics in simulations, and hence, large effects of shower-to-shower fluctuations prevent formulation of any similar statement about this model. One can only state, that the general shape of the pseudorapidity distribution seems to be reproduced by EPOS correctly.

In all investigated energy ranges (presented in Appendix C) pseudorapidity distributions from data and simulations behave as described above. However, with increasing energy the number of muon tracks is decreasing and the shape of the distributions and their mean pseudorapidity values are affected by the shower-to-shower fluctuations.

## Chapter 8

# Primary mass sensitivity of mean muon pseudorapidity

Estimation of the mass composition of cosmic rays is one of the main goals of the KASCADE-Grande experiment. From classical EAS observables, electron and muon numbers, reconstructed with high accuracy in the experiment, using unfolding procedures it was possible to reconstruct energy spectra for five elements representing different mass groups of cosmic ray particles. The analysis was done twice using simulations with two different high energy hadronic interaction models (QGSJet01 and SIBYLL 2.1). In both cases the *Knee-like* features are visible in the spectra of the light elements that is shifted towards higher energy with increasing elemental number. Detailed descriptions of this investigation can be found in Ref. [18] and [112].

However, when the determination of mass composition of cosmic rays in terms of individual mass group spectra, like in KASCADE, is not possible, one can try to estimate the *mean logarithmic mass* of detected showers from available parameters. The mean logarithmic mass is defined with formula:

$$\langle \ln A \rangle = \sum_i r_i A_i \quad (8.0.1)$$

where  $r_i$  is relative fraction of nuclei with mass  $A_i$ . Assuming the superposition model, the mean logarithmic mass can be calculated from pseudorapidity derived from the direction of EAS muons with respect to the shower arrival direction with the formula:

$$\langle \ln A \rangle = \frac{\langle \eta \rangle_{DATA} - \langle \eta \rangle_H}{\langle \eta \rangle_{Fe} - \langle \eta \rangle_H} \cdot \ln(A_{Fe}) \quad (8.0.2)$$

where  $\langle \eta \rangle_{DATA}$ ,  $\langle \eta \rangle_H$ ,  $\langle \eta \rangle_{Fe}$  is the mean pseudorapidity from the measurement and simulated H and Fe primary initiated showers, respectively.

Investigation of mass composition with  $\langle \ln A \rangle$  with  $\eta$  has some restrictions. Firstly, the hadronic interaction models used in CORSIKA simulations for this study should reasonably well describe the data. It means that experimental values for  $\langle \eta \rangle$  should be in-between the values for simulated H and Fe showers. Secondly, the mean value of muon pseudorapidity should be linearly dependent on  $\langle \ln A \rangle$ . Investigation of these restrictions is presented in Chapter 8.2.

## 8.1 Selection of shower events

The selection of showers for the analysis is described in Chapter 5.1. Investigating the primary mass composition with air shower data one has to check first whether the selection of the data is free from any bias towards light or heavy composition. In the case of analysis using the MTD data, we require having at least one muon track in every selected shower. The trigger and reconstruction efficiency in the MTD depends on the muon-to-shower distance (see Chapter 4.2.2). Therefore, it was necessary to investigate the mass sensitive parameter muon-to-electron-size-ratio and lateral pseudorapidity distribution in order to select the muon-to-shower distance range for this analysis.

As other investigations show, proton and iron initiated showers can be distinguished by its  $\lg(N_\mu)$  to  $\lg(N_e)$  ratio [113]. With the increase of the primary mass this ratio also increases [114]. Example of  $\lg(N_\mu)/\lg(N_e)$  lateral distribution is given in Fig. 8.1.1. To avoid bias towards heavy or light primary in  $\langle \ln A \rangle$  investigation it was necessary to choose limited  $R_\mu$  range where showers have constant  $\lg(N_\mu)/\lg(N_e)$ . Distance ranges for each analysed energy range are presented in Tab. 8.1.

Table 8.1:  $R_\mu$  distance ranges for each analysed energy range.

$\lg(E_0^{rec}[GeV])$	$R_\mu$ [m]
7.0-7.3	250-370
>7.0	250-370
7.3-7.6	280-400
7.6-7.9	280-430
>7.6	280-430

The selection of distances was supported also by investigation of lateral distribution of mean pseudorapidity. In Fig. 8.1.2 experimental lateral distribution is compared with simulations for two primary particles (H and Fe). Separation of H and Fe initiated showers is clearly visible, as well as the possibility of  $\langle \ln A \rangle$  investigation in the selected distance range.

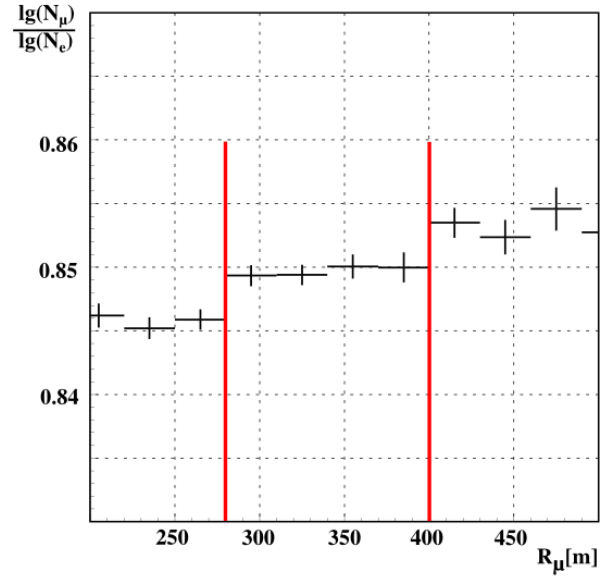


Figure 8.1.1: Example of  $\lg(N_\mu)/\lg(N_e)$  lateral distribution obtained with showers with at least one muon track. Showers fulfill condition  $7.3 < \lg(E_0^{\text{rec}}[\text{GeV}]) < 7.6$ . In a distance range between red lines the ratio is considered to be stable.

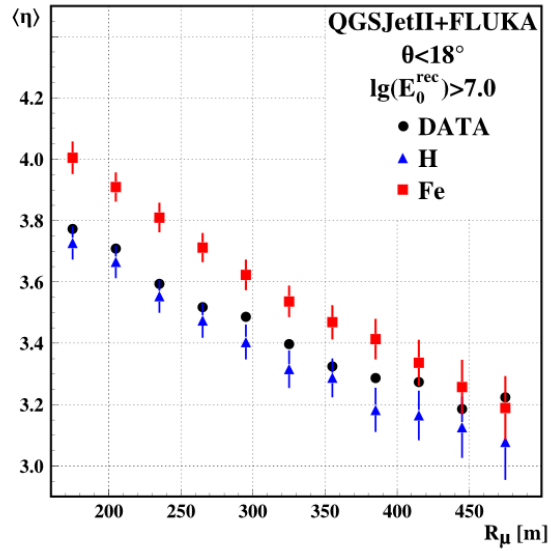


Figure 8.1.2: Lateral distribution of muon pseudorapidity. Measured data (circles) are compared with QGSJetII+FLUKA simulations of H (triangles) and Fe (squares) initiated showers. Separation of H and Fe showers is clearly visible in wide  $R_\mu$  range.

## 8.2 Data analysis and results

For the determination of mean logarithmic mass the muon tracks that fulfill the following conditions are used:

1.  $R_\mu$  distance is in a range where  $\lg(N_\mu)/\lg(N_e)$  is constant in investigated shower energy bin (see Tab. 8.1);
2.  $-0.5^\circ < \rho < 23^\circ$  and  $|\tau| < 23^\circ$ ;
3. general muon track conditions described in Chapter 5.2.

Investigation of the mean logarithmic mass is based on the mean value of pseudorapidity obtained from its distributions in the  $10^{16}$  eV -  $10^{17}$  eV decade of primary energies. The energy of each shower is estimated with the  $N_e$  formula (5.1.1)<sup>1</sup> and the mean logarithmic mass is calculated with formula (8.0.2).

Before calculating the mean logarithmic mass with pseudorapidity it is necessary to check whether this parameter depends linearly on primary mass. Examples of such investigation for two primary energy ranges are shown in Fig. 8.2.1. There, the mean pseudorapidities obtained for H, C and Fe primary initiated showers are plotted as a function of their known  $\ln A$ . Dependence  $\langle \eta \rangle = f(\ln A)$  for H, C and Fe has been fitted with a straight line (red dashed), where, e.g. for the Fig. 8.2.1a, the direction parameter is  $0.050 \pm 0.004$  and the free parameter is  $3.31 \pm 0.01$ . Fit to H and Fe primaries is shown as a blue line<sup>2</sup>. This straight line is, in fact, a graphical representation of expression (8.0.2), where the Carbon primary plays the role of data. The calculated values of  $\langle \ln A \rangle$ ,  $C_{\text{CALC}}$ , are within errors compatible with the true value for Carbon. The relatively large error bars in pseudorapidity of Carbon and corresponding  $C_{\text{CALC}}$  are due to the significantly lower number of simulated showers for this element<sup>3</sup>, comparing to the number available for H and Fe primaries.

The analysis was done in five energy ranges (with mean energy from  $1.3 \times 10^{16}$  eV to  $7.15 \times 10^{16}$  eV) and QGSJetII+FLUKA and EPOS+FLUKA model combinations. The results of the calculations are presented in Tab. 8.2. In Fig. 8.2.2, the two values of calculated  $\langle \ln A \rangle$  from this table are shown on the  $\langle \eta \rangle = f(\ln A)$  linear relation, obtained with the simulated  $\langle \eta \rangle$  values for H and Fe initiated showers.

In case of the QGSJetII model, simulated showers contain muons with too high pseudorapidity comparing to the measured values, thus calculated  $\langle \ln A \rangle$  is lower than expected from other investigations in this energy range.

<sup>1</sup>Results of investigation where the energy of each shower is estimated with the  $N_{ch}$  formula (5.1.2) are presented in Appendix D.

<sup>2</sup>The red and blue line is described with the same values of parameters up to fifth and third place after the coma for direction and free parameter, respectively.

<sup>3</sup>Simulations of shower initiated by this primary is available only in the standard and special sets of simulations

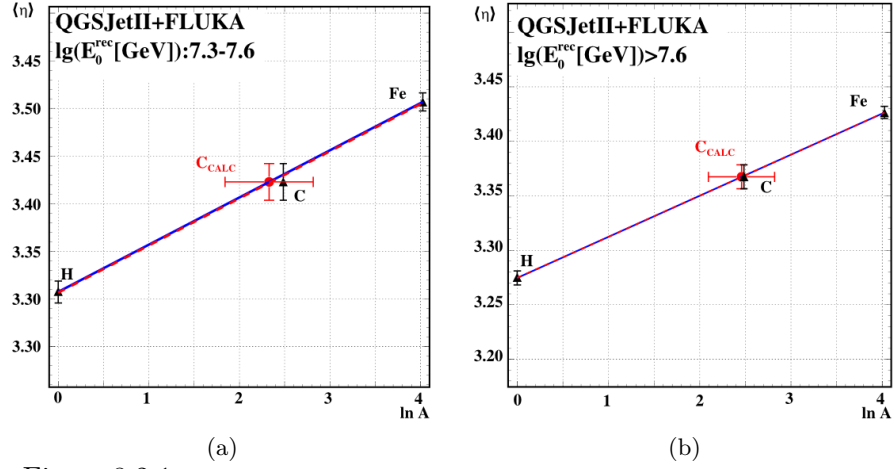


Figure 8.2.1: Example of the linearity investigation of the  $\langle \eta \rangle = f(\ln A)$  dependence in two energy ranges. The values of the mean pseudorapidity of Hydrogen, Carbon, and Iron are marked as black triangles. The  $\langle \ln A \rangle$  calculation obtained with Carbon pseudorapidity distribution ( $C_{\text{CALC}}$ ). The red dashed line represents the fit to the points obtained from simulations (H, C and Fe), the blue line is the fit to H and Fe. Panel (a) and panel (b) show the results for two energy ranges.

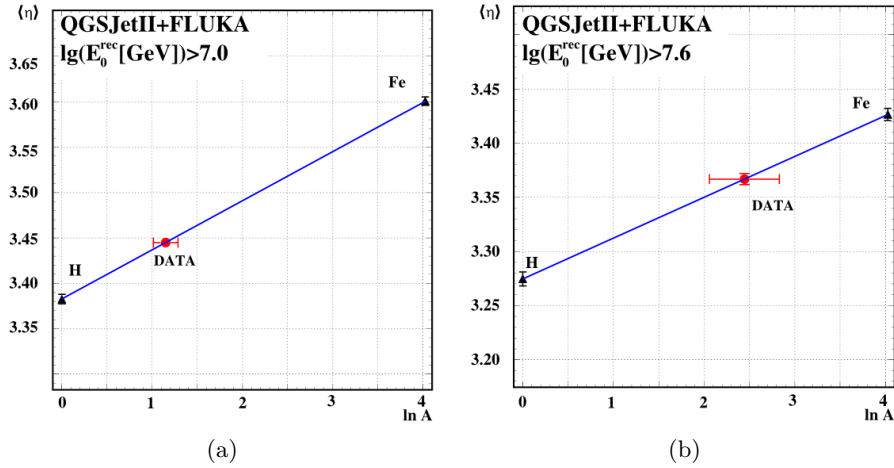


Figure 8.2.2: Example of the results of the  $\langle \ln A \rangle$  investigation. Mean pseudorapidity as function of logarithm of mass for two elements and data based on QGSJetII+FLUKA model combination in two energy ranges.

On the other hand, the EPOS model delivers lower rapidity muons, but due to the low number of particles available for the analysis the obtained results indicate only general trend of the  $\langle \ln A \rangle$  behaviour in this case.

The shift of  $\langle \ln A \rangle$  towards heavy elements is clearly visible for both

model combinations. This behaviour confirms the KASCADE-Grande result that contribution of heavy cosmic ray particles above the Knee region is rising with energy [18].

In Fig. 8.2.3 some of the results of the MTD analysis are compared with the results of the experiments that are able to investigate  $X_{max}$  of EAS by measurement of Cherenkov or fluorescent light. Observed rise of  $\langle \ln A \rangle$  with energy is consistent with other experiments results, but the values are lower due to model deficiency discussed above.

In Fig. 8.2.4 results of my analysis are shown together with the values of  $\langle \ln A \rangle$  of cosmic rays derived by experiments measuring numbers of electrons, muons and hadrons at the ground level. The inconsistency with these experiments is clearly seen.

The results of this analysis obtained with energy calculated with  $N_{ch}$  formula (5.1.2) are presented in Appendix D.

This compatibility of the MTD results rather with the results obtained from measurements of the light generated during shower development than the ones measured on ground (e.g. electron/muon ratio) is a consequence of the fact that the mean muon pseudorapidity measured on ground level is also a signature of longitudinal shower development.

Preliminary or partial results from this investigations of longitudinal shower development and  $\langle \ln A \rangle$  were presented on several international conferences [115–117].

Just recently, my investigation of muon pseudorapidity has been used to find a correlation with the lateral slope of radio signals generated by air showers, registered by LOPES experiment. This is the first experimental evidence for the sensitivity of the EAS radio signal to the longitudinal shower development, i.e. to the primary mass [118].

Table 8.2: Results of the  $\langle \ln A \rangle$  calculated in the  $10^{16}$  eV– $10^{17}$  eV primary energy range with QGSJetII+FLUKA and EPOS+FLUKA model combinations. Energy was calculated with  $N_e$  formula (5.1.1).

$\lg(E_0^{rec}[GeV])$	$\langle E_0^{rec} \rangle$ $10^7$ GeV	$\langle \eta \rangle_{DATA}$	$\langle \eta \rangle_H$ QGSJetII+FLUKA	$\langle \eta \rangle_{Fe}$ FLUKA	$\langle \ln A \rangle$	Entries		
						DATA	H	Fe
7.0 - 7.3	1.34±0.01	3.44±0.01	3.40±0.01	3.63±0.01	0.71±0.24	12939	4356	6516
>7.0	2.07±0.01	3.45±0.01	3.39±0.01	3.60±0.01	1.15±0.14	21453	20297	28712
7.3 - 7.6	2.69±0.01	3.40±0.01	3.31±0.01	3.51±0.01	1.87±0.34	4891	3920	6048
7.6 - 7.9	5.34±0.02	3.38±0.01	3.29±0.01	3.45±0.01	2.13±0.48	2349	4107	6377
>7.6	7.15±0.07	3.37±0.01	3.28±0.01	3.43±0.01	2.45±0.39	3445	12913	18328
EPOS+FLUKA								
7.0 - 7.3	1.34±0.01	3.44±0.01	3.37±0.03	3.62±0.03	1.14±0.47	12939	797	1020
>7.0	2.07±0.01	3.45±0.01	3.36±0.01	3.59±0.01	1.51±0.27	21453	3554	4515
7.3-7.6	2.69±0.01	3.40±0.01	3.28±0.03	3.51±0.03	2.11±0.26	4891	576	910
7.6-7.9	5.34±0.02	3.38±0.01	3.24±0.03	3.44±0.02	2.68±0.79	2349	674	1067
>7.6	7.15±0.07	3.37±0.01	3.23±0.01	3.43±0.01	2.79±0.47	3445	2941	3149

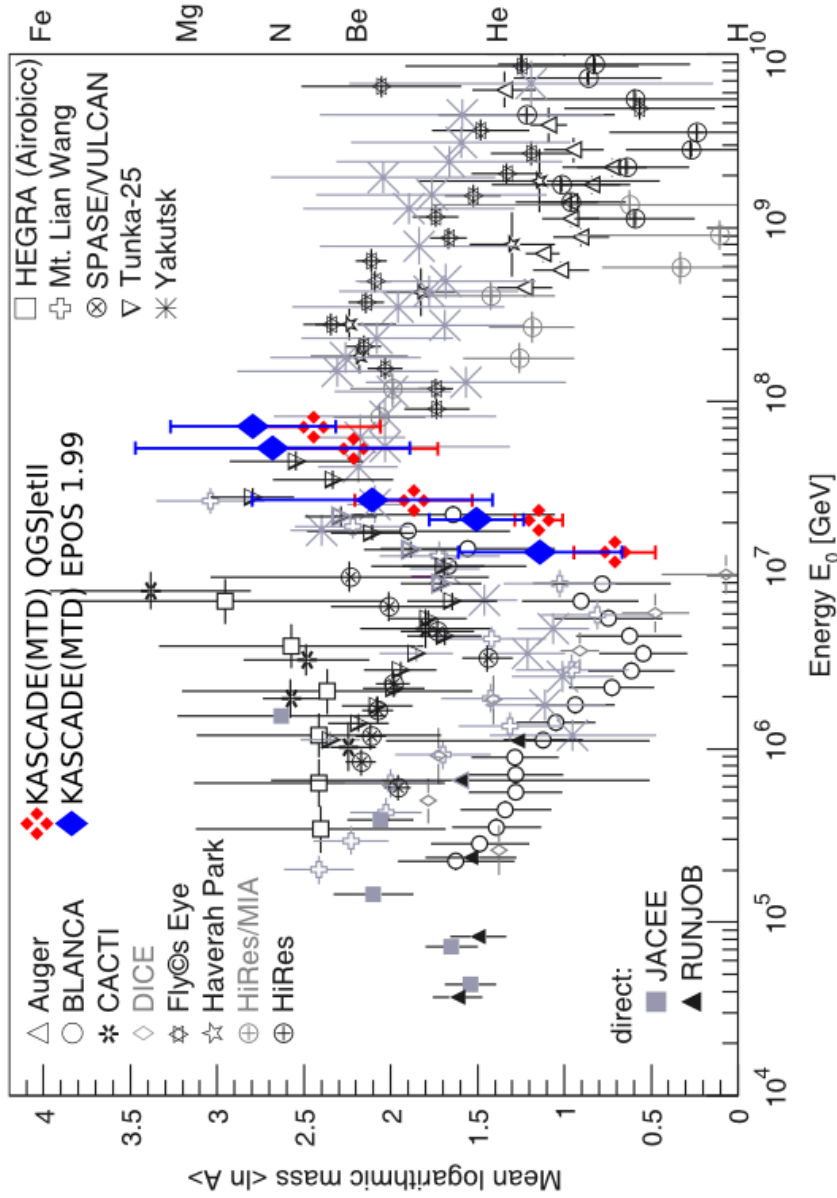


Figure 8.2.3: Results of the  $\langle \ln A \rangle$  values obtained with the mean muon pseudorapidities, shown together with the values derived from the average depth of the shower maximum by different experiments (Fig. 14(top) from Ref. [23]).

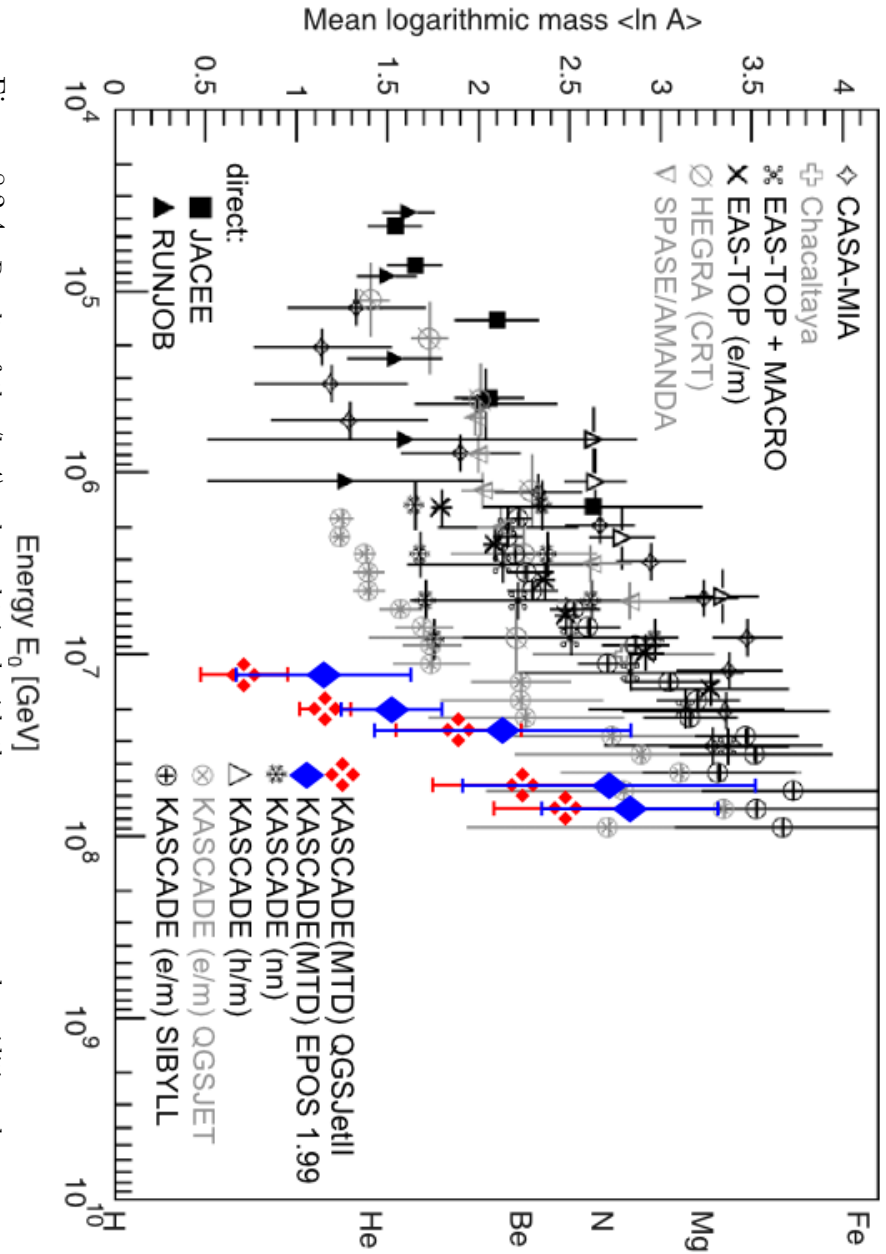


Figure 8.2.4: Results of the  $\langle \ln A \rangle$  values obtained with the mean muon pseudorapidities, shown together with the values derived from measurements of various shower particle numbers at ground level (Fig. 14(bottom) from Ref. [23]).

## Chapter 9

# Muon production height studies

Muon tracking allows to measure the composition sensitive profile of a shower in the Knee region, where it is not possible by the fluorescence technique. Muons have never been used up to now, with sufficient accuracy and large statistics, for the reconstruction of the longitudinal development of the EAS hadron component of individual showers due to the difficulty of building large area ground-based muon telescopes. It has become possible to do it only now by investigation of *muon production heights* with the MTD in KASCADE-Grande. The investigation has been based on the MTD's high reconstruction accuracy of muon directions and a very accurate determination of shower core positions by KASCADE and Grande scintillator arrays.

In this chapter the experimental investigation of the hadronic cascade in EAS using tracks of muons measured at the KASCADE-Grande experiment is presented. Those tracks are used to reconstruct muon production heights. The method of the investigation and the sensitivity of this quantity to the mass and energy of CR primary particle is shown. The validity of hadronic interaction models used in Monte Carlo simulations of muon production height is discussed. These investigations were one of the subjects of the current thesis. Their results served as starting point to the more detailed study of the primary CR composition derived with the mean muon production heights in the two decades of primary energy spectrum around the 'Knee'. This task, being outside the scope of this thesis, was a collaborative effort of several people, with some author's participation. Therefore, only final result of this spectrum will be shown at the end of this chapter for completeness.

The full and detailed final results of muon production height investigation with the MTD in KASCADE-Grande can be found in [119]. Preliminary and partial results, obtained with the active author's participation, were presented on many international conferences [120–124].

## 9.1 Reconstruction of muon production height

In our analyses we used an approach, where the muon production height  $h_\mu$  is being determined along the shower axis. For this purpose in the shower coordinate system the following relation can be used:

$$h_\mu = R_\mu / \tan(\rho) \quad (9.1.1)$$

In the formula (9.1.1) it is assumed that muons are created at the shower axis, which is not always the case. Usually they are created some meters away from the axis due to the transverse momenta of their parent mesons. However, for the investigation of mean muon production heights the assumption of relation (9.1.1) gives acceptable deviations from the true values what will be shown below, based on simulations.

Muon production height has been studied in the primary energy range  $10^{15}$  eV -  $10^{17}$  eV. In the energy range from  $10^{15}$  eV to  $10^{16}$  eV analysis was done with showers registered by the KASCADE array. There, to ensure a nearly full azimuthal symmetry of the measured muons, events with muon-to-shower distance  $R_\mu$  from 40 m to 80 m were selected (the location of the MTD is shifted by 54.65 m to the north from the KASCADE centre). In addition, this selection lowers the influence of the geomagnetic field on the mean muon directions. Below 40 m the punch-through effects forbid a valuable muon tracking and above 80 m the highly asymmetric azimuthal event distribution (see Fig. 6.3 in Ref. [125]) is difficult to correct for.

In the primary energy range from  $10^{16}$  eV to  $10^{17}$  eV showers registered with the Grande Array were used, with muons in  $R_\mu$  range from 250 m to 360 m to avoid extended punch-through and, for large distances, trigger efficiency problems. For KASCADE (Grande) selections a combined Array-MTD analysis is only reliable above shower size  $\lg(N_e) \geq 4.8$  (6.0) and  $\lg(N_\mu) \geq 4.1$  (5.5).

The zenith angle of investigated showers was restricted to be smaller than  $18^\circ$  and the mean muon production height was calculated in the altitude range up to 12 km along the shower axis, where the majority of muons with energy on ground above 800 MeV are produced ( e.g. about 90% of muons, according to CORSIKA simulations, in  $10^{16}$  eV proton induced showers). The value of 12 km was chosen because already at this altitude, and for the selected distance range of investigated muons to the shower core, the uncertainties in the  $\rho$  angle values become comparable to the values themselves.

In Fig. 9.1.1 an illustration of angular relations between muon track and the shower axis is given. The track of the muon produced from pion decay at some point away from the axis, as well as the reconstructed direction of this muon in the MTD, are shown. The difference between muon direction at production and on ground is mainly due to the multiple Coulomb scattering of the muon in the atmosphere. The  $h_\mu$  calculated with the radial

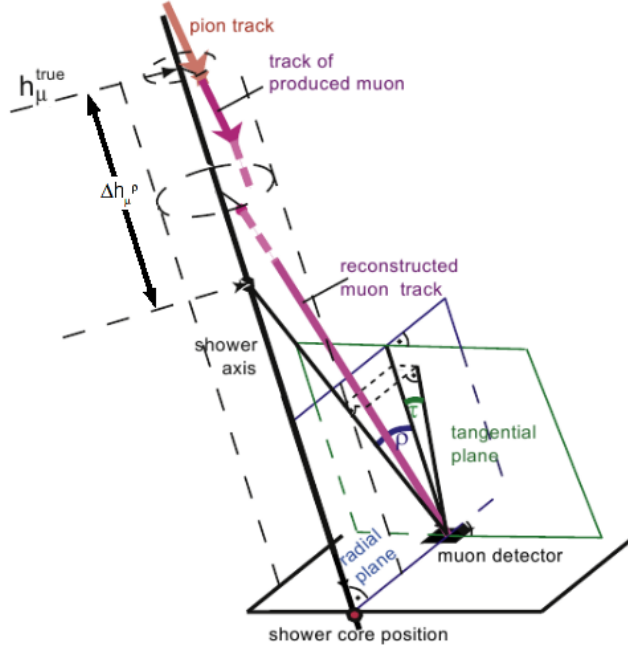


Figure 9.1.1: An illustration of angular relations between muon track and the shower axis. The difference between the true and the reconstructed  $h_{\mu}$  values is shown.

angle differs from the true one by  $\Delta h_{\mu}^{\rho}$ , as shown in the Fig. 9.1.1.

One can expect this difference being smaller if one could correct for this multiple scattering. However, the amount of scattering is not known. It can be restricted by applying radial and tangential angle cuts:  $0^{\circ} < \rho < 8^{\circ}$  and  $|\tau| < 0.7^{\circ}$ . The  $\tau$  cut, according to Monte Carlo simulations, enriches the sample with high-energy muons, above a few GeV [126], having smaller average scattering angles ( $\sigma_{\tau} \approx 0.2^{\circ}$ ) and smaller bending in the geomagnetic field, which improves the determination of the correct production height.

Limitation of radial angle values to  $0^{\circ} < \rho < 8^{\circ}$  and, in addition, considering for the analysis only tracks with cluster sizes along the wires and at the strips not larger than 10 cm and 16 cm, respectively, eliminate tracks not belonging to shower muons or originating in the absorber above the MTD.

It was checked with Monte Carlo simulations that up to 12 km altitude and in a distance range 40-80 m between a muon and the shower core, subtraction of the absolute value of  $\tau$  from  $\rho$  when calculating  $h_{\mu}$  - formula (9.1.2) - brings the reconstructed average value of  $h_{\mu}$  closer to the true one.

$$h_{\mu} = R_{\mu} / \tan(\rho - |\tau|). \quad (9.1.2)$$

In Tab. 9.1 comparison of differences between mean values of true muon production height and values calculated with the both formulas are presented. The systematic mean muon production height error, in % of the true value, is given for the two fixed primary energies and the two primary

Table 9.1: Dependence of the systematic mean muon production height errors (in % of the true value)

1	2	3	4
Primary	$E_0[\text{eV}]$	$\Delta h_\mu^\rho$	$\Delta h_\mu^\rho(\text{cor})$
H	$10^{15}$	-3.1%	+2.1%
Fe	$10^{15}$	-7.3%	-3.5%
H	$10^{16}$	-1.8%	+4.2%
Fe	$10^{16}$	-5.0%	-0.5%

species. Presented results for muons with energy above 800 MeV are obtained with CORSIKA simulated showers (500 showers for  $10^{15}$  eV and 158 showers for  $10^{16}$  eV) using QGSJet01 and GHEISHA model combination. In all investigated cases, the calculated mean muon production height differs from the true value by a few percent but the use of formula (9.1.2) gives indeed some improvement of the accuracy. Therefore, in this work the formula (9.1.2) has been applied.

The analysis is based on 3-hit tracks only. Together with the track quality parameters discussed in [95] this results in the number of muon tracks uncorrelated with a shower being below 1%.

Summarising, the following selection criteria were used for showers and muons in this analysis:

Shower cuts:

1. Showers with 3-hit tracks;
2. Shower zenith angle less than  $18^\circ$  ;
3. Shower age  $0.2 < s < 2.1$  ;
4. Electron shower size  $\lg(N_e) > 4.8$ .

Muon cuts:

1.  $0^\circ < \rho < 8^\circ$  and  $|\tau| < 0.7^\circ$ ;
2.  $40 \text{ m} < R_\mu < 80 \text{ m}$  for KASCADE analysis;
3.  $250 \text{ m} < R_\mu < 360 \text{ m}$  for Grande analysis;
4. Maximal cluster sizes: 10 cm (wires) and 16 cm (strips);
5. Hit pattern: patt3=123.

## 9.2 Muon production heights in showers induced by light and heavy primary masses

In investigation of primary mass sensitivity of any shower parameter the most straightforward approach is to study the behaviour of this parameter in heavy and light primary CR induced showers. As shown in [113, 125] the

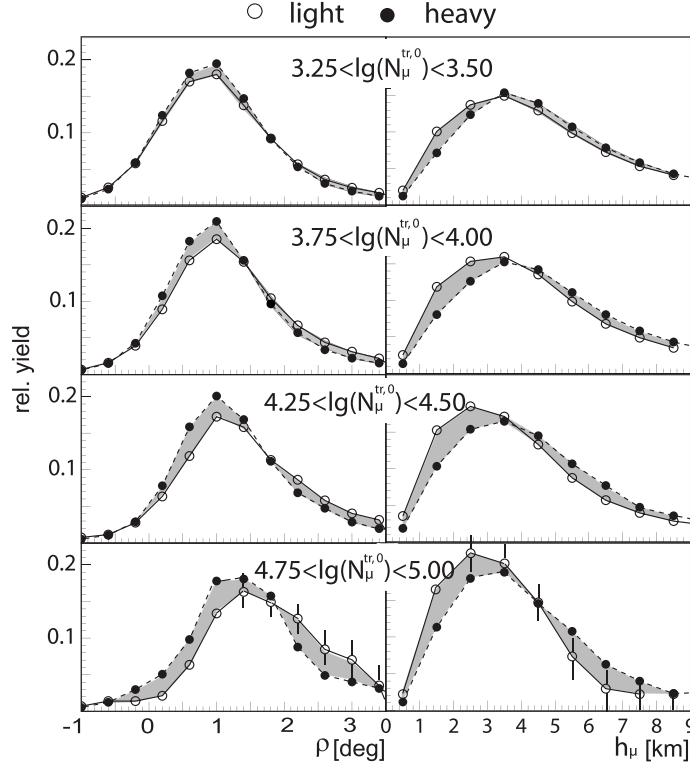


Figure 9.2.1: Radial angle distributions (left panel) and muon production height distributions  $h_\mu$  along the shower axis (right panel) for light and heavy CR primary mass enriched showers and for different  $\lg(N_\mu^{tr,0})$  intervals. Lines connect the data points to guide the eyes [119].

electron size  $\lg(N_e)$  and muon size  $\lg(N_\mu^{tr})$  provide an opportunity to separate light from heavy primary initiated showers. The ratio of the corrected for their shower angle dependent attenuation parameters  $\lg(N_\mu^{tr,0})/\lg(N_e^0)$  turned out to be sensitive to the mass composition of primary CR. In KASCADE analysis the border value of this ratio was 0.74.

Showers with  $\lg(N_\mu^{tr,0})/\lg(N_e^0) > 0.74$  and  $\lg(N_\mu^{tr,0})/\lg(N_e^0) \leq 0.74$  were classified as initiated by heavy and light primaries, respectively.

Fig. 9.2.1 shows the distributions of the radial angle and muon production height (left and right panel, respectively) for the selected distance range 40-80 m for different primary energies (expressed in terms of muon size). With the increase of the muon number radial angle distributions are shifting towards higher values and both quantities show increasing mass sensitivity (light and heavy distributions are better separated).

At high energies large muon production altitudes are predominantly created by heavy primaries. Distributions become narrower, differently for light and heavy components, what is an indication of a decrease of fluctuations in the  $\langle h_\mu \rangle$  parameter with increasing primary energy.

In Fig. 9.2.2 experimental values of the mean muon production height

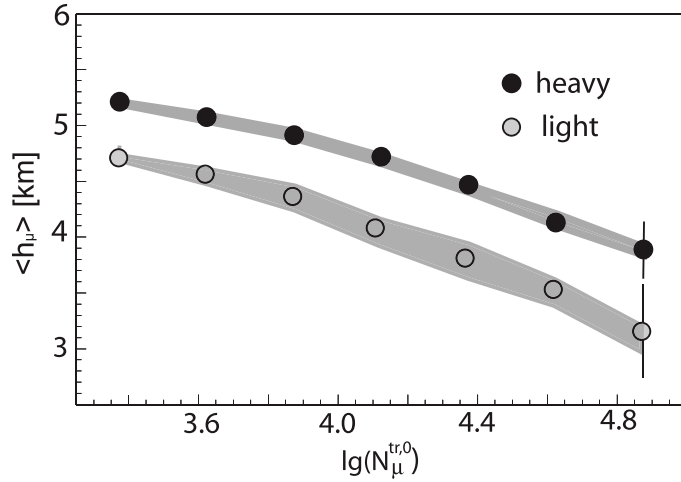


Figure 9.2.2: Experimental values of the mean muon production height along the shower axis  $\langle h_\mu \rangle$  vs.  $\lg(N_\mu^{tr,0})$  for light and heavy primary mass enriched showers. The bands bracketing the data points represent variations for the  $\lg(N_\mu^{tr,0})/\lg(N_e^0)$  ratio from 0.73 to 0.75 [119].

$\langle h_\mu \rangle$  as a function of  $\lg(N_\mu^{tr})$  are shown. A good separation between light and heavy enriched primary CR particles is seen. The dependence of both components on  $\lg(N_\mu^{tr,0})$  (dependence on primary energy) suggests that mean production heights corrected for an appropriate elongation rate will exhibit a clear remaining dependence on the CR particle mass. Mean muon production heights for light and heavy mass enriched showers exhibit a height difference of about 12%, which is 3–4 times the systematic error quoted in Tab. 9.1.

The sensitivity of the heavy/light separation on the chosen separation value 0.74 was checked. Shaded bands in Fig. 9.2.2 show how  $\langle h_\mu \rangle$  changes when the boundary between heavy and light is moved by  $\pm 0.01$  in the  $\lg(N_\mu)/\lg(N_e)$  ratio, which is 10–20% of the peak position difference in the distributions of this ratio for proton and iron primary induced showers [125]. A broader band observed for light sample can be explained by larger fluctuations in the shower development than in case of showers initiated by heavy CR primaries.

### 9.3 Test of hadronic interaction models with muon production heights

In Fig. 9.3.1 the muon production height distributions of Fig. 9.2.1 are compared to Monte Carlo simulation results for proton (triangles) and iron (squares) primaries. The CORSIKA simulations were using QGSJetII and, for interaction energies below 200 GeV, FLUKA2002.4 hadronic interaction models. Identical cuts for data and simulations were used and the slope of

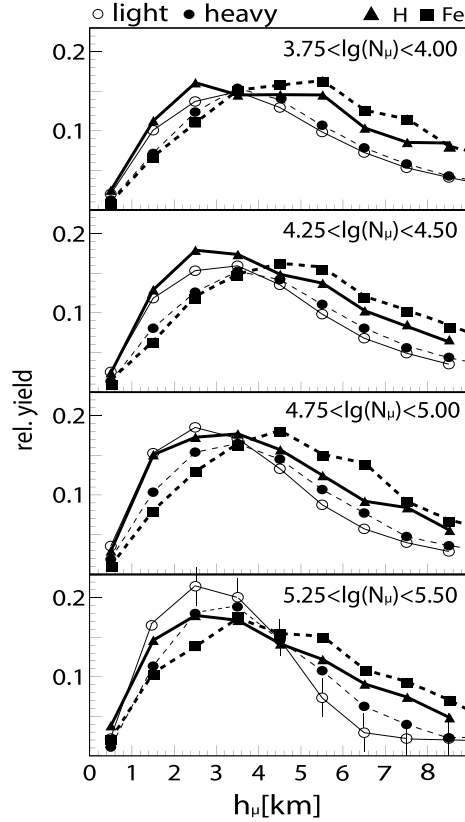


Figure 9.3.1: Light (open circles) and heavy (full circles) enriched shower samples compared to CORSIKA simulations employing QGSJetII+FLUKA models for proton (H) and iron (Fe) primaries. Lines connect the data points to guide the eyes [119].

the simulated energy spectrum was weighted to  $-2.7$  below and to  $-3.1$  above the Knee. Detector simulations were based on GEANT [75].

The plots of  $h_\mu$  (as well as in Fig. 9.2.1) are normalised to integral yield equal one in the full range up to 12 km but they are shown to 9 km only in order to expand the low production height region. However, the following discussion of the features seen at high values of  $h_\mu$  is also true for the production heights above 9 km.

In this expanded region we see that up to  $\approx 3.5$  km data points are embraced by the simulation results. Muons observed there, up to  $\lg(N_\mu) \sim 5.0$ , stem from hadronic interactions of energies below 200 GeV, modelled in simulations with FLUKA. This suggests that low-energy interaction model describes the data well. In the highest  $\lg(N_\mu)$  bin the contribution from higher interaction energies in this region increases and the description of the data by simulations is not so good any more.

Muons produced above 3.5 km have parent mesons predominantly cre-

ated at interaction energies larger than 200 GeV, which are modelled in simulations by the QGSJetII code. The discrepancies between data and simulations suggest that the high-energy model has problems in describing the data.

The comparison reveals more muons at high production heights in the simulations (the distributions are shifted to the right). This excess of muons in the simulations at high altitudes with respect to the data may indicate that muons produced higher up have too high an energy and do not decay, surviving to the observation level, what is not observed in the measurements. The same effect will occur when the simulated mesons have too small an energy in the region of the first or second interaction, and would decay earlier than in real showers.

The revealed discrepancy in muon production height distributions between QGSJet simulations and measurements points to the necessity of further investigation of high-energy interaction models. Our test results in a suggestion that shifting the maximum of shower development in the HE interaction models deeper in the atmosphere will act in the direction of reducing the observed discrepancy with the data.

## 9.4 Cosmic ray composition derived with the muon production heights

It has been demonstrated above that the muon production height depends on the mass of the primary CR and its energy. It has been also shown that the hadronic interaction models used in Monte Carlo simulations do not describe the experimental data in the whole range of investigated altitudes. Therefore, for the more detailed study of this mass dependence of muon production height a model independent method was developed [119]. Two parameter distribution  $\lg(N_e)$  vs.  $\lg(N_\mu)$ , for measured showers passing the shower and muon selection criteria, was used for this purpose. For each such shower the mean muon production height was calculated, now expressed in atmospheric depth  $H_\mu$  in  $\text{g}/\text{cm}^2$ . It has been found that certain muon production depth  $H_\mu^A$  regions create bands in the two parameter  $\lg(N_e)$  vs.  $\lg(N_\mu)$  space, which can be transformed into CR energy spectra of relative muon production depth abundances in the range from  $\approx 10^{15}$  eV to  $\approx 10^{17}$  eV (Fig. 9.4.1). In this figure the Grande data, analysed in the separate distance range, are normalised to KASCADE flux in two bins below and above  $\lg(E_0[\text{GeV}]) = 7.7$ , i.e. in the overlapping region. One observes distinct features in the spectra. While the ‘low mass’ (i.e.  $H_\mu^A$  large) spectra show a rapid drop with increasing shower energy, ‘medium’ and ‘heavy mass’ (i.e.  $H_\mu^A$  small) spectra seem to overtake at large primary energy. This feature is model independent because only the experimental data were used for obtaining muon production depth abundances.

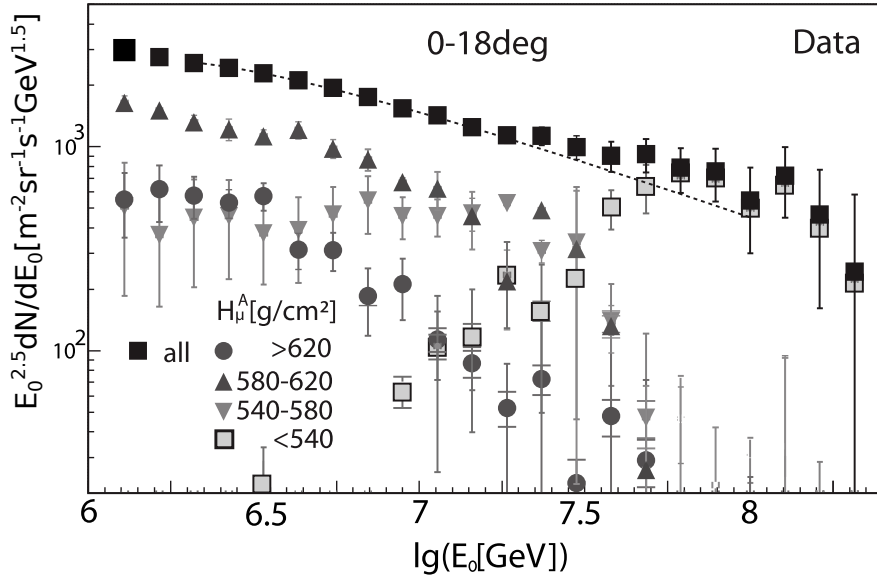


Figure 9.4.1: Energy spectra (from Ref. [119]) for primaries which produce muons at different effective muon production depth  $H_{\mu}^A$  in the atmosphere; above  $\lg(E_0[\text{GeV}])=7.7$  the Grande Array data analysed in a separate distance range are considered. The dashed line reproduces the CR spectrum as measured by KASCADE [112].

So far, no explicit mass range assignment has been given. A coarse mass scale may be provided by the relation between maximum of the muon production height distribution ( $H_{\mu}^A_{max}$ ) and the value of mean logarithmic mass  $\langle \ln A \rangle$ .

These spectra have features similar to the energy spectra of primary mass groups from Ref. [112]. The lightest masses (here the largest atmospheric depths) have a break in the spectrum at lower energies compared to the heavier (smaller depths) ones.

The total flux spectrum in Fig. 9.4.1 is in good agreement with the KASCADE spectrum (as indicated by a dashed line) obtained by an unfolding technique [112].

# Chapter 10

## Summary

In this work the results of the investigations of muons in EAS with the large area streamer tube Muon Tracking Detector (MTD) in KASCADE-Grande experiment has been presented. The MTD has been included into the multidetector EAS experiment KASCADE in order to supplement the conventional scintillation detector arrays in studying shower properties with the muon tracking technique. This made possible not only to cross-check with the results of the KASCADE array the measurements of lateral muon density distributions. It enabled to study such parameters, solely available with tracking, like muon production heights and, for the first time, EAS muon pseudorapidities.

The investigation of experimental data was based on EAS registered by KASCADE-Grande experiment from November 2003 to June 2009. For all but muon production height analyses showers with primary energy above  $10^{16}$  eV were selected, having muons registered by the MTD in the distance range to the shower core from 100 m to 700 m. The same analysis was performed for EAS simulated with CORSIKA software for QGSJetII+FLUKA and EPOS+FLUKA model combinations and the experimental results were compared with the results from simulations.

The lateral density distributions of muons were investigated, for the first time being based on counted muon tracks not on estimated numbers of particles from measured energy deposits (as it is in the case of scintillation detectors). This investigation provided information about distributions of EAS muons above energy 800 MeV, in four primary energy ranges above  $10^{16}$  eV, and in a large muon-to-shower distance range, from 100 m to 700 m.

The shown compatibility of the distributions with the results obtained for 230 MeV muons, measured with KASCADE detector array, was a proof of a good performance of the MTD in track measurements.

The experimental lateral density distributions were compared with the distributions for simulated showers. The simulations using QGSJetII+FLU-

KA model combinations well describe the shape of the distributions, giving a positive result of the model test with this shower parameter.

In KASCADE-Grande experiment high precision in measurements of such shower parameters like shower direction and shower core position, combined with high angular accuracy of muon tracking, made possible, for the first time, to investigate pseudorapidity of EAS muons. As proved by simulations, the pseudorapidity of detected EAS muons is closely related to the pseudorapidity of their parent particles, thus providing information about interactions from which they originate and reflecting the longitudinal development of the EAS cascade. Therefore, this parameter is very useful to test HE hadronic interaction models in the energy range not accessible to the man-made accelerators.

For this purpose the experimental pseudorapidity distributions were compared with distributions from simulations obtained with QGSJetII+FLUKA and EPOS+FLUKA model combinations in five primary energy intervals. The conclusion from these analyses is the following: both model combinations provide the distributions having shapes compatible with the experimental ones. Experimental distributions are embraced by distributions given by proton and iron initiated showers. However, the shape of the data distributions are closer to the proton shower distributions, which is not expected from other mass composition investigations in the analysed energy range. The experimental pseudorapidity should rather be closer to iron shower distribution (considering the shape and the mean pseudorapidity value). This indicates that the tested HE interaction models deliver too many high pseudorapidity muons to the observation level. Shifting the maximum of shower development deeper into the atmosphere in those simulations could be a change in right direction to lessen the observed discrepancy with the measurements.

Estimation of the primary mass composition of cosmic rays is one of the main goals of the KASCADE-Grande experiment. Therefore, various reconstructed shower parameters are checked for the mass sensitivity. The mean muon pseudorapidity was a very promising parameter in this aspect and such investigation was one of the tasks of this work.

Using the mean pseudorapidity values of measured MTD data and simulated for proton and iron initiated showers the mean logarithmic mass of cosmic rays was calculated in the primary energy range  $10^{16}$  eV -  $10^{17}$  eV for the two model combinations: QGSJetII+FLUKA and EPOS+FLUKA. The obtained values have been compared with the results of other experiments that estimate the mass composition from particle detectors, and experiments that detect Cherenkov/fluorescent light. The increase of  $\langle \ln A \rangle$  values with increasing energy was found, which is consistent with the results from other experiments, but obtained values are smaller than expected, due

to the mentioned above model deficiencies. Moreover, it was shown, that the MTD results are compatible with the  $\langle \ln A \rangle$  values found by experiments calculating it from the  $X_{max}$ , using the Cherenkov or fluorescent light. This is an experimental evidence that the mean muon pseudorapidity measured on ground level is a signature of the longitudinal shower development.

Muon tracking allows to measure the composition sensitive profile of a shower in the energy range of the Knee, where it is not possible with the fluorescence technique. Muons have never been used up to now, with sufficient accuracy and large statistics, for the reconstruction of the longitudinal development of the EAS hadron component of individual showers. It has become possible to do it only now by investigation of *muon production heights* with the MTD in KASCADE-Grande. The investigation has been based on the MTD's high reconstruction accuracy of muon directions and a very accurate determination of shower core positions by KASCADE and KASCADE-Grande arrays.

With the mean muon production heights the validity of the QGSJetII and FLUKA hadronic interaction models used in Monte Carlo EAS simulations has been checked and the mass composition of CR primaries in the two decades of primary energy around the Knee has been studied. A clear separation between light and heavy primary initiated showers in the data has been found. However, the comparison of the experimental data with the simulated showers revealed that there are more muons at high muon production heights in simulations, where most interactions of particles are described with QGSJetII model. This deficiency of HE model in describing the muon production height data was earlier revealed in the pseudorapidity analysis, where the excess of high pseudorapidity values (carried by muons from high altitudes) in simulated showers was found. The muon production height distributions from simulations at low altitudes (where most interactions of particles are described with FLUKA model) are consistent with the distributions from data. Due to this finding, that the hadronic interaction models used in Monte Carlo simulations do not describe the experimental data in the whole range of investigated altitudes, the detailed primary mass composition study with the mean muon production heights (being outside the scope of this thesis) was done in a model independent way. With this method energy spectra of four individual primary mass groups (represented by certain muon production height abundances) was obtained, having similar features as the energy spectra of primary mass groups obtained by KASCADE array data analysis.

The results of model tests with the muon pseudorapidity and muon production heights have already been taken into account in the next generation of the QGSJetII and EPOS models being prepared. With the further model development (supported by the MTD analyses) the investigation of

hadronic interactions using muon pseudorapidities and investigation of the mass composition should be continued, using possibly also another model, like SIBYLL. For this purpose the statistics of simulated showers should be sufficiently increased.

## Appendix A

# Selection of the experimental and simulated showers

Table A.1 contains numbers of showers and reconstructed muon tracks available in data and numbers of H and Fe initiated showers and muon tracks simulated with QGSJetII+FLUKA<sup>1</sup> and EPOS+FLUKA<sup>2</sup> model combination available for the MTD analysis. Shows fulfill condition  $\lg(E_0^{rec}[GeV]) > 7.0$ . “STD”, “SPEC” and “SPEC<sub>MTD</sub>” refer to standard, special and special MTD set of simulations, respectively (see Chapter 5.3 for details)<sup>3</sup>.

$N_{sh}$  is a number of shower events when the MTD was active and the shower core was within the MTD fiducial area.

$N_{sh}^{cut}$  is a number of showers after the cuts from Chapter 5.1.

$N_{tr3}$  ( $N_{tr2}$ ) is a number of 3-hit (2-hit) tracks in showers  $N_{sh}^{cut}$ .

$N_{tr3}^{cut}$  ( $N_{tr2}^{cut}$ ) is a number of 3-hit (2-hit) tracks after the cuts from Chapter 5.2.

---

<sup>1</sup> QGSJet-II-2+FLUKA2002.4

<sup>2</sup> EPOS1.99+FLUKA2008.3

<sup>3</sup> In case of EPOS+FLUKA simulations only fraction of the standard set of simulations could be used in the analysis presented in this work.

Table A.1: Numbers of showers and muon tracks in data and simulations available for the analysis before and after applying the shower and muon cuts. See text for details.

	DATA	QGSJet+FLUKA					
		STD		SPEC		SPEC <sub>MTD</sub>	
		H	Fe	H	Fe	H	Fe
$N_{sh}$	2977697	100245	124044	144982	184027	34405	38281
$N_{sh}^{cut}$	65912	2877	2778	1765	1646	13324	12882
$N_{tr3}$	328290	33319	44097	23880	28117	139375	189750
$N_{tr3}^{cut}$	29412	14258	20943	9704	13047	60703	90167
$N_{tr2}$	327238	9828	12436	6431	7683	41508	56160
$N_{tr2}^{cut}$	35056	3605	5519	2380	3271	15875	23898
EPOS+FLUKA							
$N_{sh}$		41908	48555	347	199	13151	11835
$N_{sh}^{cut}$		1310	1057	92	18	1489	1511
$N_{tr3}$		14007	19715	10105	2626	21815	28785
$N_{tr3}^{cut}$		6291	9028	3491	758	9029	13214
$N_{tr2}$		4338	5398	1490	306	5886	7873
$N_{tr2}^{cut}$		1629	2180	659	85	2227	3292

## Appendix B

# Lateral muon density distributions

Here the lateral muon density distributions in energy bins obtained with the  $N_{ch}$  formula (equation (5.1.2)) are presented. All conditions used in this analysis are the same as in Chapter 6. As expected, all conclusions from the analysis presented in Chapter 6 are valid for this analysis and all results are compatible.

Table B.1: Results of the fits of the lateral density of muons in energy range  $10^{16}$  eV– $10^{17}$  eV. The energy is obtained with  $N_{ch}$  formula

$\lg(E_0^{rec}[GeV])$ range	$\langle E_0^{rec} \rangle$ [ $10^7$ GeV]	KASCADE		MTD	
		$r_0[m]$	$\chi^2/NDF$	$r_0[m]$	$\chi^2/NDF$
7.0 - 7.3	$1.340 \pm 0.001$	$479 \pm 13$	23/10	$378 \pm 4$	18.5/10
7.3 - 7.6	$2.689 \pm 0.005$	$326 \pm 14$	37/10	$362 \pm 5$	160/10
7.6 - 7.9	$5.34 \pm 0.02$	$276 \pm 17$	31/10	$279 \pm 8$	61.6/11
7.9 - 8.2	$10.41 \pm 0.06$	$193 \pm 20$	37/10	$204 \pm 15$	46.8/9

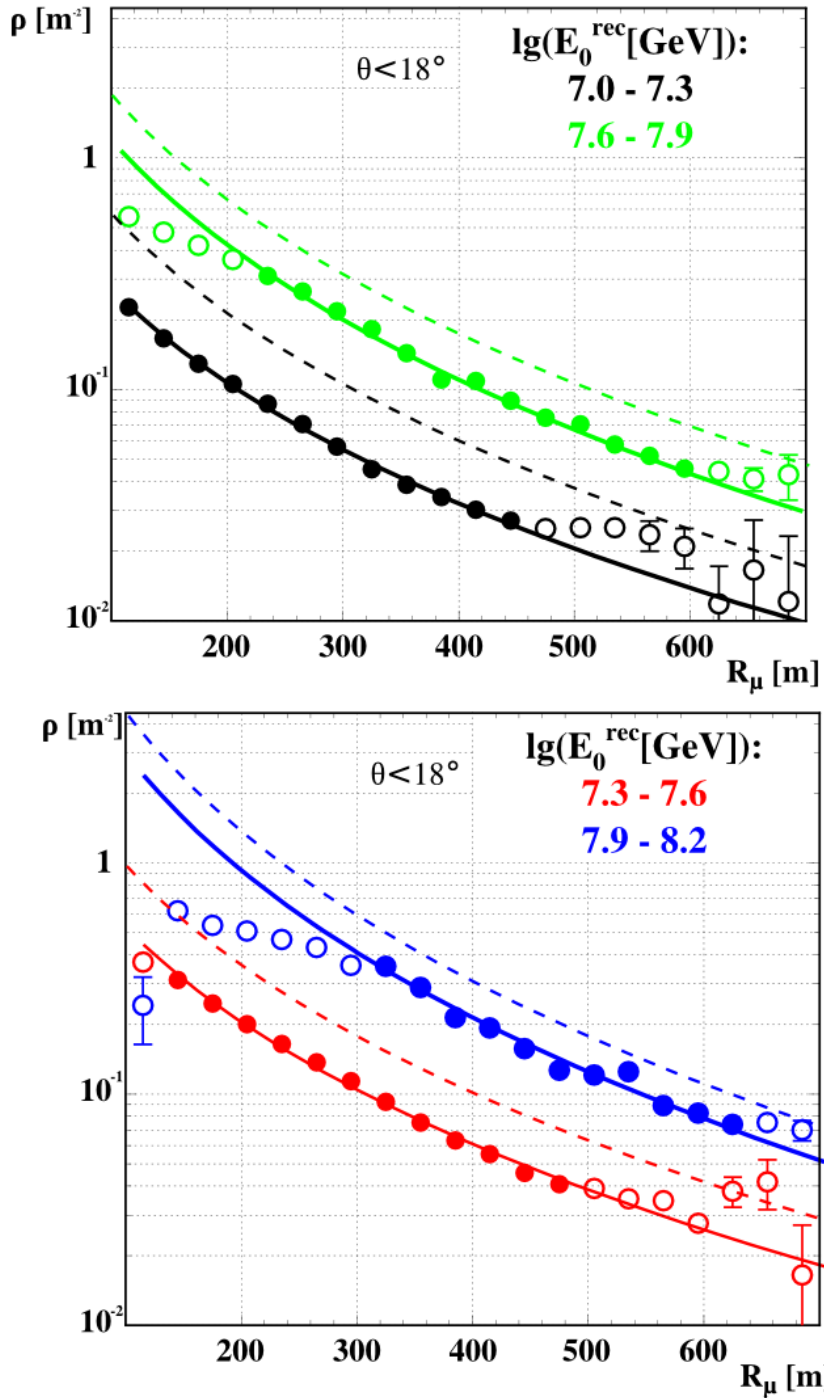


Figure B.0.1: Lateral density distributions of muons from the MTD in four energy bins. Lines are fits to the muon density distributions obtained with the MTD (solid lines, points used in the Lagutin fit are marked with full symbols) and muon density distributions obtained with the KASCADE Array of shielded plastic scintillators (dashed lines).

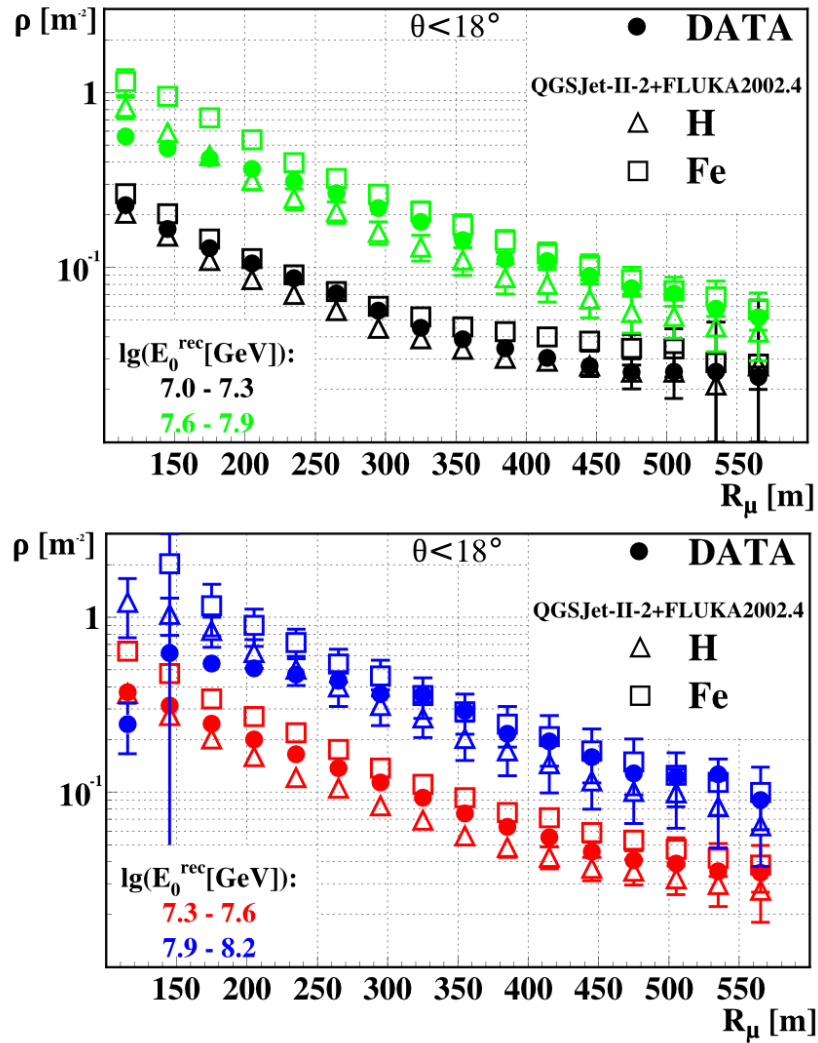


Figure B.0.2: Lateral muon density distributions obtained with the MTD measurements (solid symbols) and CORSIKA simulations (open symbols) in four energy ranges.

## Appendix C

# Pseudorapidity of muons in EAS

In this appendix the results of tests of interaction models with pseudorapidity distributions are presented. Pseudorapidity distributions calculated from MTD data are compared with pseudorapidity from proton and iron initiated showers simulated with CORSIKA for two model combinations: QGSJet-II-2+FLUKA2002.4 (Fig. C.0.1 and C.0.3) and EPOS1.99+FLUKA2008.3 (Fig. C.0.2 and C.0.4). Comparison is done in five energy and  $R_\mu$  distance ranges. The energy is calculated with  $N_e$  formula<sup>1</sup> in Fig C.0.1 and C.0.2 and with  $N_{ch}$  formula<sup>2</sup> in Fig C.0.3 and C.0.4.

---

<sup>1</sup> See equation (5.1.1), page 52

<sup>2</sup> See equation (5.1.2), page 53

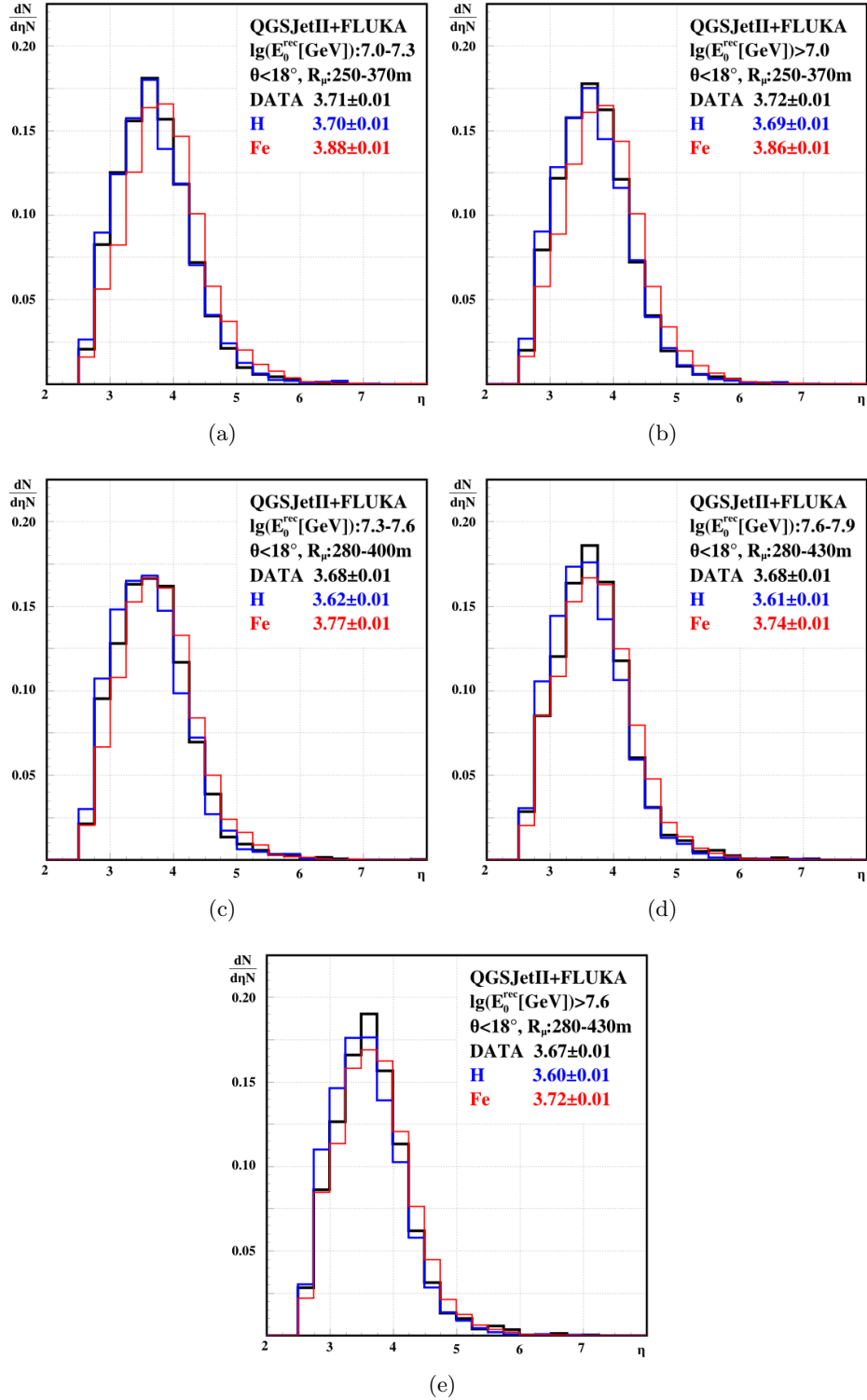


Figure C.0.1: Pseudorapidity distributions (normalized to integral) from data and H and Fe initiated showers simulated with QGSJetII+FLUKA model combination. Muons from showers with zenith angle up to  $18^\circ$ . The energy of showers is estimated with  $N_e$  formula.

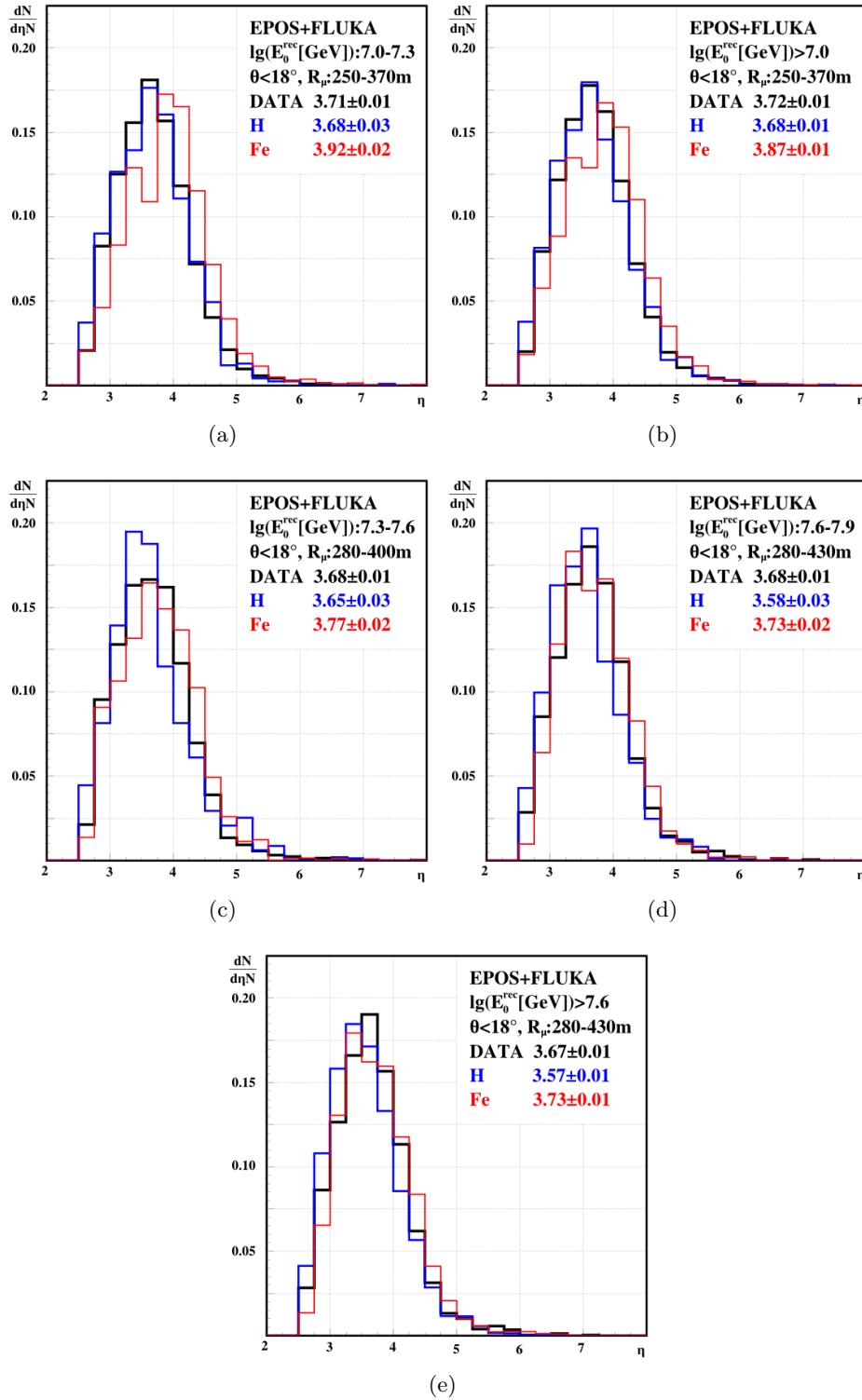


Figure C.0.2: Pseudorapidity distributions (normalized to integral) from data and H and Fe initiated showers simulated with QGSJetII+FLUKA model combination. Muons from showers with zenith angle up to  $18^\circ$ . The energy of showers is estimated with  $N_e$  formula.

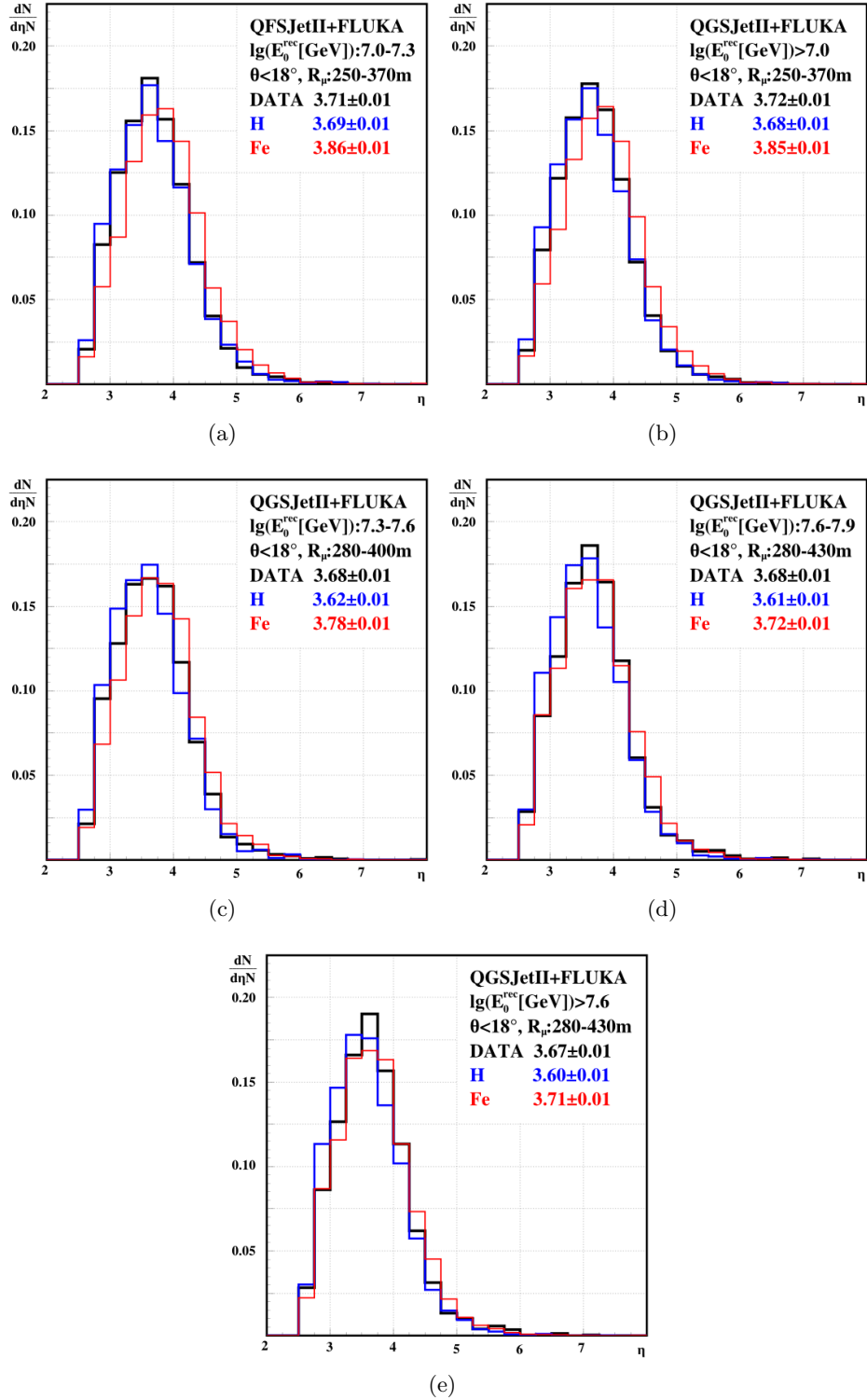


Figure C.0.3: Pseudorapidity distributions (normalized to integral) from data and H and Fe initiated showers simulated with QGSJetII+FLUKA model combination. Muons from showers with zenith angle up to  $18^\circ$ . The energy of showers is estimated with  $N_{ch}$  formula.

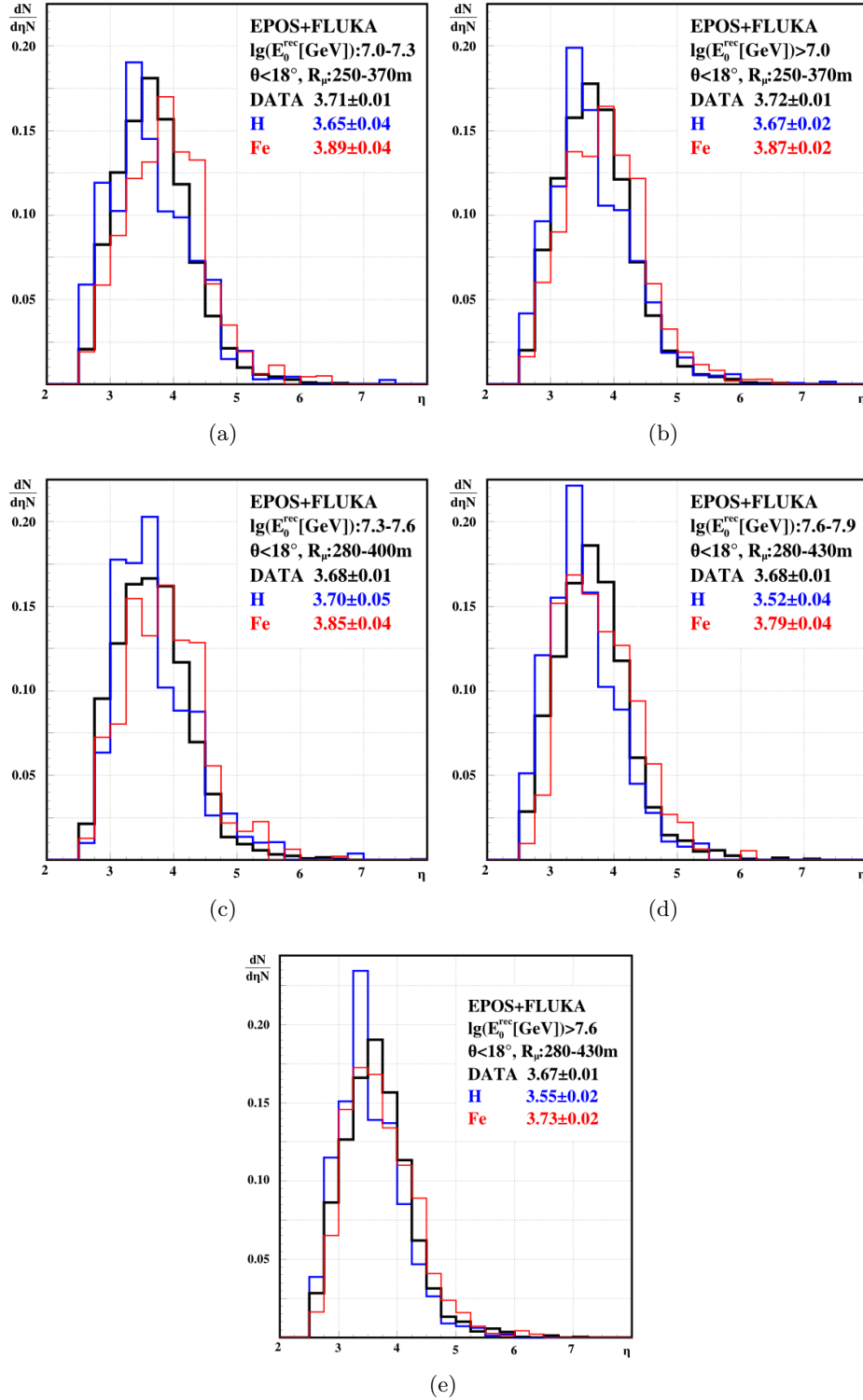


Figure C.0.4: Pseudorapidity distributions (normalized to integral) from data and H and Fe initiated showers simulated with QGSJetII+FLUKA model combination. Muons from showers with zenith angle up to  $18^\circ$ . The energy of showers is estimated with  $N_{ch}$  formula.

## Appendix D

# Primary mass sensitivity of mean pseudorapidity

In Tab. D.1 results of the  $\langle \ln A \rangle$  calculated in the  $10^{16}$  eV– $10^{17}$  eV primary energy range with QGSJetII+FLUKA and EPOS+FLUKA model combinations are presented. Energy was calculated with formula (5.1.2). The results are compatible with those presented in Tab. 8.2.

In Fig.D.0.1 results of the MTD analysis are compared with the results of the experiments that are able to investigate  $X_{max}$  of EAS by measurement of Cherenkov, fluorescent light or from direct measurements. Observed rise of  $\langle \ln A \rangle$  with energy is consistent with other experiments, but the values are lower than expected.

Table D.1: Results of the  $\langle \ln A \rangle$  calculated in the  $10^{16}$  eV– $10^{17}$  eV primary energy range with QGSJetII+FLUKA and EPOS+FLUKA model combinations. Energy was calculated with  $N_{ch}$  formula (5.1.2).

$\lg(E_0^{rec}[\text{GeV}])$	$\langle E_0^{rec} \rangle$ 10 <sup>7</sup> GeV	$\langle \eta \rangle_{DATA}$	$\langle \eta \rangle_H$ QGSJetII+FLUKA	$\langle \eta \rangle_{Fe}$ QGSJetII+FLUKA	$\langle \ln A \rangle$	Entries	
						DATA	H Fe
7.0 - 7.3	1.34±0.01	3.44±0.01	3.39±0.01	3.61±0.01	0.95±0.24	12939	4433 6862
>7.0	2.10±0.01	3.45±0.01	3.38±0.01	3.59±0.01	1.31±0.14	21453	19532 27417
7.3 - 7.6	2.69±0.01	3.40±0.01	3.31±0.01	3.51±0.01	1.87±0.33	4891	3892 5857
7.6 - 7.9	5.34±0.02	3.38±0.02	3.28±0.01	3.44±0.01	2.43±0.51	2349	3935 6241
>7.6	7.13±0.08	3.37±0.01	3.27±0.01	3.41±0.01	2.71±0.41	3445	12120 16813
7.0 - 7.3	1.34±0.01	3.44±0.016	3.35±0.04	3.60±0.04	1.42±0.78	DATA	H Fe
>7.0	2.10±0.01	3.45±0.015	3.37±0.02	3.60±0.02	1.32±0.42	12939	334 413
7.3 - 7.6	2.69±0.01	3.40±0.01	3.30±0.05	3.58±0.04	1.46±0.77	21453	1477 1699
7.6 - 7.9	5.34±0.02	3.38±0.02	3.18±0.05	3.47±0.04	2.72±0.95	4891	284 400
>7.6	7.13±0.08	3.37±0.01	3.19±0.02	3.41±0.02	3.24±0.64	2349	233 297
			EPOS+FLUKA			3445	1297 1201

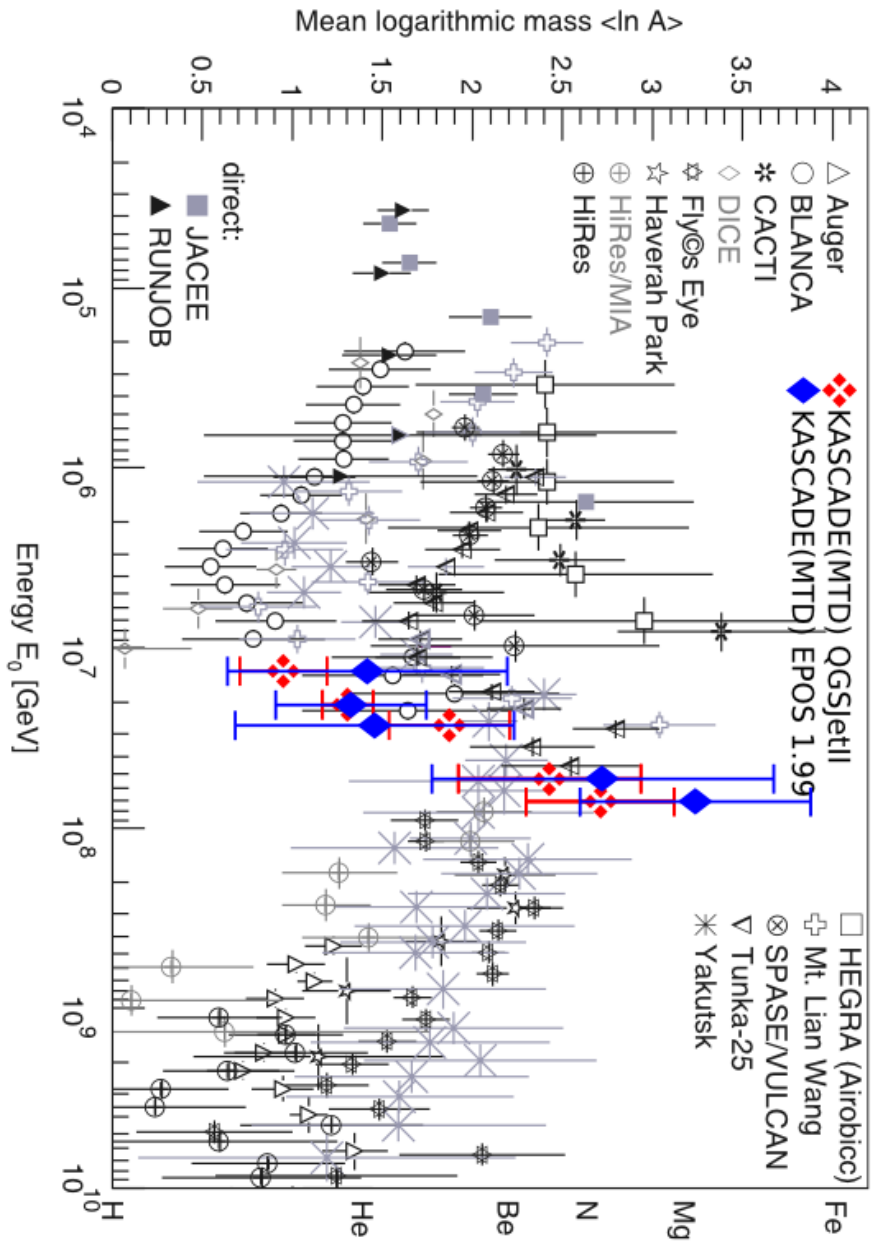


Figure D.0.1: Results of the  $\langle \ln A \rangle$  values obtained with the mean muon pseudorapidities, shown together with the values derived from the average depth of the shower maximum by different experiments (Fig. 14(top) from Ref. [23]).

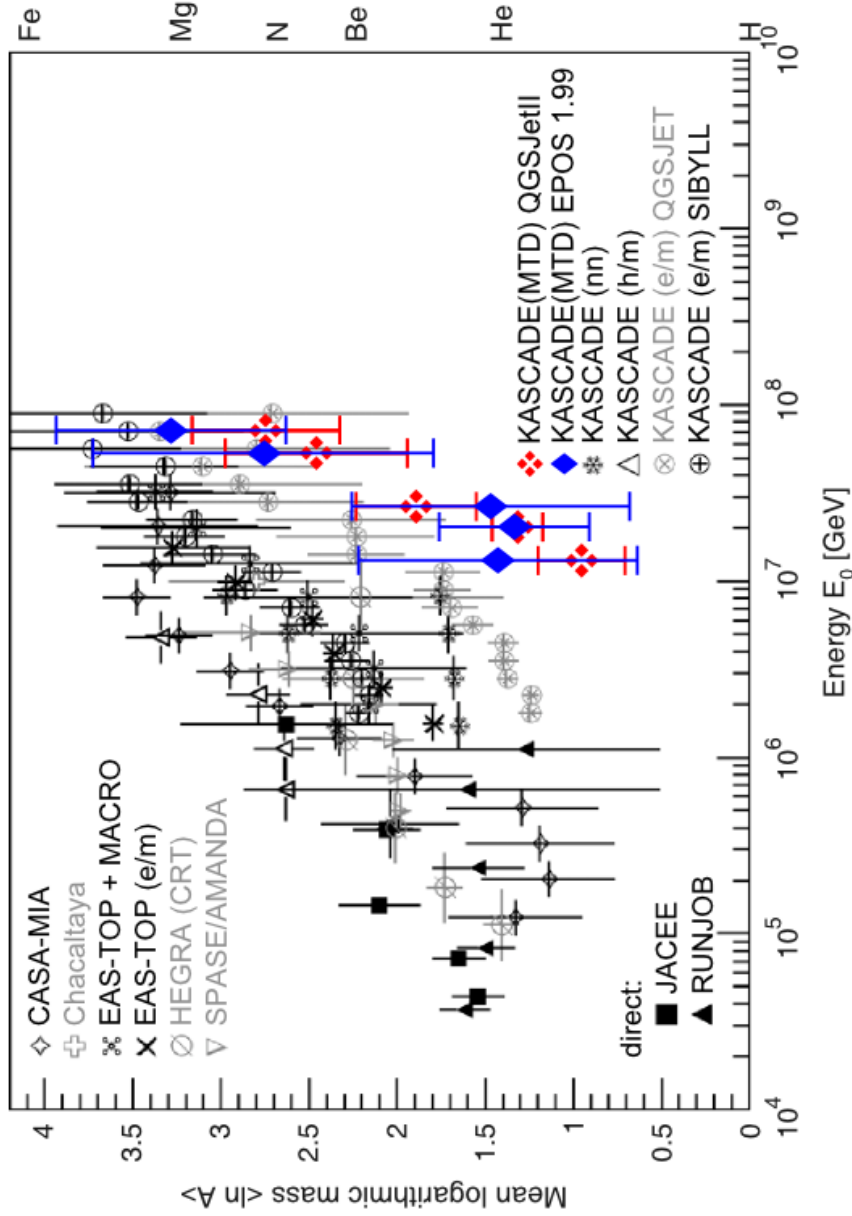


Figure D.0.2: Results of the  $\langle \ln A \rangle$  values obtained with the mean muon pseudorapidities, shown together with the values derived from measurements of various shower particle numbers at ground level (Fig. 14(bottom) from Ref. [23]).

# List of Tables

3.1	Components of the KASCADE-Grande experiment . . . . .	30
4.1	ST chamber design parameters . . . . .	45
6.1	Results of the fits of the lateral density of muons in energy range $10^{16}$ eV– $10^{17}$ eV. . . . .	60
8.1	$R_\mu$ distance ranges for each analysed energy range. . . . .	75
8.2	Results of the $\langle \ln A \rangle$ calculated in the $10^{16}$ eV– $10^{17}$ eV primary energy range with QGSJetII+FLUKA and EPOS+FLUKA model combinations. Energy was calculated with $N_e$ formula (5.1.1). . . . .	80
9.1	Dependence of the systematic mean muon production height errors (in % of the true value) . . . . .	86
A.1	Numbers of showers and muon tracks in data and simulations available for the analysis before and after applying the shower and muon cuts. See text for details. . . . .	97
B.1	Results of the fits of the lateral density of muons in energy range $10^{16}$ eV– $10^{17}$ eV. The energy is obtained with $N_{ch}$ formula . . . . .	98
D.1	Results of the $\langle \ln A \rangle$ calculated in the $10^{16}$ eV– $10^{17}$ eV primary energy range with QGSJetII+FLUKA and EPOS+FLUKA model combinations. Energy was calculated with $N_{ch}$ formula (5.1.2). . . . .	107

# Bibliography

- [1] V.F. Hess. “Über Beobachtungen der durchdringenden Strahlung bei sieben Freiballonfahrt”. *Physikalische Zeitschrift*, 13:1084–1091, 1912.
- [2] P. Auger, P. Ehrenfest, R. Maze, J. Daudin, and R. A. Fréon. “Extensive Cosmic-Ray Showers”. *Rev. Mod. Phys.*, 11:288–291, Jul 1939.
- [3] W.D. Apel et al. [Łuczak](KASCADE-Grande Collaboration). “Knee-like structure in the spectrum of the heavy component of cosmic rays observed with KASCADE-Grande”. *Phys.Rev.Lett.*, 107:171104, 2011.
- [4] M. Nagano et al. “Energy spectrum of primary cosmic rays above  $10^{17.0}$  eV determined from extensive air shower experiments at Akeno”. *J. Phys. G*, 18(2):423, 1992.
- [5] R. U. Abbasi et al. (High Resolution Fly’s Eye Collaboration). “First Observation of the Greisen-Zatsepin-Kuzmin Suppression”. *Phys. Rev. Lett.*, 100:101101, Mar 2008.
- [6] B. Peters. “Primary cosmic radiation and extensive air showers”. *Il Nuovo Cimento (1955-1965)*, 22:800–819, 1961. 10.1007/BF02783106.
- [7] J.R. Hörandel. “Cosmic Rays From The Knee To The Second Knee:  $10^{14}$  To  $10^{18}$  eV”. *Mod. Phys. Lett. A*, 22:1533–1551, 2007.
- [8] K. Greisen. “End to the Cosmic-Ray Spectrum?”. *Phys. Rev. Lett.*, 16:748–750, Apr 1966.
- [9] G. T. Zatsepin and V. A. Kuz’min. “Upper limit of the spectrum of cosmic rays”. *J. Exp. Theor. Phys. Lett.*, 4:78–80, 1966.
- [10] T. Stanev. “*High Energy Cosmic Rays*”. Springer-Verlag, Berlin, 1 edition, 2004.
- [11] E. Fermi. “On the Origin of the Cosmic Radiation”. *Phys. Rev.*, 75:1169–1174, Apr 1949.

- [12] W. I. Axford, E. Leer, G. Skadron. “The acceleration of cosmic rays by shock waves”. In *Proceedings of the 15<sup>th</sup> International Cosmic Ray Conference*, volume 11, pages 132–137, Plovdiv, Bulgaria, August 13–26 1977. B’lgarska Akademiia na Naukite. (A79-44583 19-93).
- [13] F. Aharonian et al. (H.E.S.S. Collaboration). “High-energy particle acceleration in the shell of a supernova remnant”. *NATURE*, 432:75–77, 2004.
- [14] C. J. Cesarsky and T. Montmerle. “Gamma rays from active regions in the galaxy: The possible contribution of stellar winds”. *Space Sci. Rev.*, 36:173–193, Oct 1983.
- [15] A.K. Harding and T.K. Gaisser. “Acceleration by Pulsar Winds in Binary-Systems”. *Astrophys. J.*, 358:561–574, 1990. Iss 2.
- [16] R. Antonucci. “Unified models for active galactic nuclei and quasars”. *Annu. Rev. AA*, 31:473–521, 1993. (A94-12726 02-90).
- [17] M. Aglietta et al. (EAS-TOP Collaboration, MACRO Collaboration). “The primary cosmic ray composition between  $10^{15}$  and  $10^{16}$  eV from extensive air showers electromagnetic and TeV muon data”. *Astropart. Phys.*, 20:641–652, 2004.
- [18] T. Antoni et al. (KASCADE Collaboration). “KASCADE measurements of energy spectra for elemental groups of cosmic rays: Results and open problems”. *Astropart. Phys.*, 24:1–25, 2005. arxiv:astro-ph/0505413.
- [19] G. V. Kulikov and G. B. Khristiansen. “On the size distribution of extensive atmospheric showers”. *J. Exp. Theor. Phys. Lett.*, 8:441, 1959. *Zh.Eksp.Teor.Fiz.* 35, 635 (1958).
- [20] D. Kazanas and A. Nicolaidis. “Cosmic Ray "Knee": A Herald of New Physics?”. In *Proceedings of the 27<sup>th</sup> International Cosmic Ray Conference*, page 1760 (2201), Hamburg, Germany, 2001. arxiv:astro-ph/0103147.
- [21] D. Kazanas and A. Nicolaidis. “Cosmic Rays and Large Extra Dimensions”. *Gen. Rel. Grav.*, 35:1117–1123, 2003. arxiv:hep-ph/0109247.
- [22] A.D. Erlykin and A.W. Wolfendale. “Structure in the cosmic ray spectrum: an update”. *J. Phys. G*, 27:1005, 2001.
- [23] J. Blümer, R. Engel, and J. R. Hörandel. “Cosmic Rays from the Knee to the Highest Energies”. *Prog. Part. Nucl. Phys.*, 63:293–338, 2009. arXiv/0904.0725.

- [24] V. Berezhinsky, A. Gazizov, and S. Grigorieva. “Propagation and Signatures of Ultra High Energy Cosmic Rays”. *Nucl. Phys. B*, 136:147, 2004.
- [25] A.M. Hillas. “Can diffusive shock acceleration in supernova remnants account for high-energy galactic cosmic rays?”. *J. Phys. G*, 31:R95–R131, 2005.
- [26] J. Abraham et al. (Pierre Auger Collaboration). “Observation of the Suppression of the Flux of Cosmic Rays above  $4 \times 10^{19}$  eV”. *Phys. Rev. Lett.*, 101:061101, Aug 2008.
- [27] Jörg R. Hörandel. “Cosmic-ray abundances and energy spectra at high energies: Measurements with TRACER and KASCADE”. *Adv. Space Res.*, 38:1549–1557, 2006.
- [28] J. A. Simpson. “Elemental and Isotopic Composition of the Galactic Cosmic-Rays”. *Annu. Rev. Nucl. Part. Sci.*, 33:323–381, 1983.
- [29] Katharina Lodders. “Solar System Abundances and Condensation Temperatures of the Elements”. *Astrophys. J.*, 591(2):1220, 2003.
- [30] J.R. Hörandel. “On total inelastic cross-sections and the average depth of the maximum of extensive air showers”. *J. Phys. G*, 29:2439–2464, 2003. arxiv:astro-ph/0309010.
- [31] J.R. Hörandel. “On the mean logarithmic mass of cosmic rays derived from measurements of the average depth of the maximum of extensive air showers”. *Nucl. Phys. Proc. Suppl.*, 151:75–78, 2006.
- [32] K. Greisen (editor:J.G. Wilson). “*Progress in Cosmic Ray Physics*”, volume 3. North-Holland, Amsterdam, 1965.
- [33] K. Kamata and J. Nishimura. “The Lateral and the Angular Structure Functions of Electron Showers”. *Prog. Theor. Phys. Suppl.*, 6:93–155, 1958.
- [34] J. Knapp and D. Heck. “Upgrade of the Monte Carlo code CORSIKA to simulate extensive air showers with energies  $10^{20}$  eV”. Technical Report 6097, Forschungszentrum Karlsruhe in der Helmholtz-Gemeinschaft (FZKA), Karlsruhe, 1998.
- [35] J. van Buren. “*Investigations of the muon component of extensive air showers measured by KASCADE-Grande*”. PhD thesis, Universität Karlsruhe, Karlsruhe, 2007. FZKA 7292.
- [36] G. Brooke and P.J.V. Eames. “An economical method for studying very large extensive air showers”. *Nucl. Instrum. Meth. A*, 241(2-3):572 – 580, 1985.

- [37] M. Teshima, H. Ohoka, Y. Matsubara, T. Hara, Y. Hatano, N. Hayashida, C.X. He, M. Honda, F. Ishikawa, K. Kamata, T. Kifune, M. Mori, M. Nagano, K. Nishijima, Y. Ohno, and G. Tamahashi. “Expanded array for giant air shower observation at Akeno”. *Nucl. Instrum. Meth. A*, 247(2):399 – 411, 1986.
- [38] M. Aglietta et al. (EAS-TOP Collaboration). “The EAS-TOP Array at  $E(0) = 10^{14}$  eV -  $10^{16}$ eV: Stability and resolutions”. *Nucl. Instrum. Meth. A*, 277:23–28, 1989.
- [39] T. Antoni et al. (KASCADE Collaboration). “The Cosmic ray experiment KASCADE”. *Nucl. Instrum. Meth. A*, 513:490–510, 2003.
- [40] W.D. Apel et al. [Łuczak](KASCADE-Grande Collaboration). “The KASCADE-Grande experiment”. *Nucl. Instrum. Meth. A*, 620:202–216, 2010.
- [41] J. Abraham, M. Aglietta, I.C. Aguirre, M. Albrow, D. Allard, and I. Allekotte (Pierre Auger Collaboration). “Properties and performance of the prototype instrument for the Pierre Auger Observatory”. *Nucl. Instrum. Meth. A*, 523(1-2):50 – 95, 2004.
- [42] Y. Takahashi1 et al. (JEM-EUSO Collaboration). “The JEM-EUSO mission”. *New J. Phys.*, 11:065009 (21pp), 2009.
- [43] <http://jemeuso.riken.jp>.
- [44] <http://www.mpi-hd.mpg.de/hfm/CT>.
- [45] H. Falcke et al. (LOPES collaboration). “Detection and imaging of atmospheric radio flashes from cosmic ray air showers”. *NATURE*, 435:313–316, 2005.
- [46] D. Ardouin et al. (CODALEMA Collaboration). “Radio-Detection Signature of High Energy Cosmic Rays by the CODALEMA Experiment”. *Nucl. Instrum. Meth. A*, 555:148, 2005.
- [47] T. Huege et al. (Pierre Auger Collaboration). “Radio detection of cosmic rays in the Pierre Auger Observatory”. *Nucl. Instrum. Meth. A*, 617:484–487, 2010.
- [48] J. Knapp and D. Heck. “Extensive air shower simulation with CORSIKA : a users manual”. Technical Report 5196B, Kernforschungszentrum Karlsruhe (KfK), Karlsruhe, 1993.
- [49] Igor Katkov. “Physics with the CMS forward CASTOR calorimeter”. *PoS*, QFTHEP2010:006, 2010.

- [50] Ralph Engel. “Hadronic interactions and extensive air showers”. *J. Phys.: Conf. Ser.*, 47(1):213, 2006.
- [51] O. Adriani et al. (LHCf Collaboration). “The LHCf detector at the CERN Large Hadron Collider”. *JINST*, 3(08):S08006, 2008.
- [52] H. Menjo et al. (LHCf Collaboration). “The status and preliminary results of the LHC forward experiment: LHCf”. In *Proceedings of the 18<sup>th</sup> International Workshop on Deep-Inelastic Scattering and Related Subjects*, Firenze, Italy, April 19-23 2010. Proceedings of the Science.
- [53] V. Berardi et al. (TOTEM Collaboration). “Total cross-section, elastic scattering and diffraction dissociation at the Large Hadron Collider at CERN : TOTEM Technical Design Report”. Technical report, CERN, Geneva, January 2004. CERN-LHCC-2004-002, TOTEM-TDR-001.
- [54] G. Latino et al. (TOTEM Collaboration). “First Results from the TOTEM Experiment”. In *Proceedings of the 2<sup>nd</sup> International Workshop on Multiple Partonic Interactions at the LHC*, 2010. arXiv:hep-ex/1110.1008.
- [55] P. Jenni, M. Nessi, and M. Nordberg. “Zero Degree Calorimeters for ATLAS”. Technical report, CERN, Geneva, Jan 2007. LHCC-I-016. CERN-LHCC-2007-001.
- [56] N.N. Kalmykov and S.S. Ostapchenko. “The Nucleus-nucleus interaction, nuclear fragmentation, and fluctuations of extensive air showers”. *Phys. Atom. Nucl.*, 56:346–353, 1993.
- [57] N.N. Kalmykov, S.S. Ostapchenko, and A.I. Pavlov. “EAS and a quark - gluon string model with jets”. *Bull. Russ. Acad. Sci. Phys.*, 58:1966–1969, 1994.
- [58] N.N. Kalmykov, S.S. Ostapchenko, and A.I. Pavlov. “Quark-gluon string model and EAS simulation problems at ultra-high energies”. *Nucl. Phys. Proc. Suppl.*, 52B:17–28, 1997.
- [59] S. Ostapchenko. “QGSJET-II: Towards reliable description of very high energy hadronic interactions”. *Nucl. Phys. Proc. Suppl.*, 151:143–146, 2006.
- [60] S. Ostapchenko. “Status of QGSJET”. *AIP Conf. Proc.*, 928:118–125, 2007. arXiv:hep-ph/0706.3784.
- [61] M. Hladik, H.J. Drescher, S. Ostapchenko, T. Pierog, and K. Werner. “Selfconsistency requirement in high-energy nuclear scattering”. *Phys. Rev. Lett.*, 86:3506–3509, 2001. arxiv:hep-ph/0102194.

- [62] R. Engel, T.K. Gaisser, T. Stanev, and P. Lipari. “Air shower calculations with the new version of SIBYLL”. In *Proceedings of the 26<sup>th</sup> International Cosmic Ray Conference*, volume 516, page 407, Salt Lake City, Utah, Aug 17-25 1999, published 2000. AIP Conference Proceedings.
- [63] J. Ranft. “Dual parton model at cosmic ray energies”. *Phys. Rev. D*, 51:64–84, Jan 1995.
- [64] K. Werner. “Strings, pomerons and the VENUS model of hadronic interactions at ultrarelativistic energies”. *Physics Reports*, 232(2-5):87 – 299, 1993.
- [65] H.J. Drescher, M. Hladik, S. Ostapchenko, T. Pierog, and K. Werner. “Parton-based Gribov–Regge theory”. *Physics Reports*, 350(2-4):93 – 289, 2001.
- [66] J. N. Capdevielle (editor). “The Karlsruhe extensive air shower simulation code CORSIKA”. Technical Report 4998, Kernforschungszentrum Karlsruhe (KfK), Karlsruhe, 1992.
- [67] A. Ferrari, P. R. Sala, A. Fasso, and J. Ranft. “FLUKA: A multi-particle transport code (Program version 2005)”. Technical report, CERN, 2005. CERN-2005-010.
- [68] <http://www.fluka.org>.
- [69] H. Fesefeldt. “*The simulation of hadronic showers: physics and applications*”, volume 2 of *PITHA*. Physikalisches Institut RWTH Aachen, 1985.
- [70] S.A. Bass, M. Belkacem, M. Bleicher, M. Brandstetter, L. Bravina, C. Ernst, L. Gerland, M. Hofmann, S. Hofmann, J. Konopka, G. Mao, L. Neise, S. Soff, C. Spieles, H. Weber, L.A. Winckelmann, H. Stoecker, W. Greiner, Ch. Hartnack, J. Aichelin, and N. Amelin. “Microscopic models for ultrarelativistic heavy ion collisions”. *Prog. Part. Nucl. Phys.*, 41(0):255 – 369, 1998.
- [71] M Bleicher, E Zabrodin, C Spieles, S A Bass, C Ernst, S Soff, L Bravina, M Belkacem, H Weber, H Stöcker, and W Greiner. “Relativistic hadron-hadron collisions in the ultra-relativistic quantum molecular dynamics model”. *J. Phys. G*, 25(9):1859, 1999.
- [72] W.R. Nelson, H. Hirayama, and David W.O. Rogers. “The EGS4 code system”. Technical Report SLAC-R-265, SLAC National Accelerator Laboratory, 1985.
- [73] <http://irs.inms.nrc.ca/software/egsnrc/>.

- [74] A. V. Pljasheshnikov A. A. Lagutin and V. V. Uchaikin. “On the lateral distribution of electrons in electromagnetic cascades in air”. In *Proceedings of the 16<sup>th</sup> International Conference on Cosmic Rays*, volume 7, page 18, Kyoto, Japan, 1979.
- [75] M. Goossens. “*GEANT: Detector Description and Simulation Tool, long writeup W5013; Oct 1994*”. CERN Program Library. CERN, Geneva, 1993.
- [76] W.D. Apel et al. [Łuczak](KASCADE Collaboration). “A test of the hadronic interaction model EPOS with air shower data”. *J. Phys. G*, 36(3):035201, 2009.
- [77] D. Heck. “The Influence of Hadronic Interaction Models on Simulated Air-Showers: A Phenomenological Comparison”. Talk presented at the CORSIKA School 2008, Lauterbad, Germany.
- [78] A.B. Kaidalov and K.A. Ter-Martirosian. “Multiple Production of Hadrons at High-Energies in the Model of Quark-Gluon Strings”. *Sov. J. Nucl. Phys.*, 39:979, 1984.
- [79] V.N. Gribov. “A reggeon diagram technique”. *Sov. Phys. J. Exp. Theor. Phys. Lett.*, 26:414–422, 1968.
- [80] V.N. Gribov. “Glauber corrections and the interaction between high-energy hadrons and nuclei”. *Sov. Phys. J. Exp. Theor. Phys. Lett.*, 29:483–487, 1969.
- [81] F.M. Liu, H.J. Drescher, S. Ostapchenko, T. Pierog, and K. Werner. “Consistent treatment of soft and hard processes in hadronic interactions”. *J. Phys. G*, 28:2597–2616, 2002. arxiv:hep-ph/0109104.
- [82] S. Ostapchenko. “Nonlinear screening effects in high energy hadronic interactions”. *Phys. Rev. D*, 74:014026, Jul 2006.
- [83] S. Ostapchenko. “On the re-summation of enhanced Pomeron diagrams”. *Phys. Lett. B*, 636:40–45, 2006.
- [84] T.K. Gaisser and F. Halzen. “Soft Hard Scattering in the TeV Range”. *Phys. Rev. Lett.*, 54:1754, 1985.
- [85] S.S. Ostapchenko. “Contemporary models of high-energy interactions: Present status and perspectives”. *J. Phys. G*, 29:831–842, 2003.
- [86] S. Ostapchenko. “Models for cosmic ray interactions”. *Czech. J. Phys.*, 56:A149–A159, 2006. arxiv:hep-ph/0601230.

- [87] D. Heck, G. Schatz, and J. Knapp. “Influence of hadronic interaction models on the development of EAS in Monte Carlo simulations”. *Nucl. Phys. Proc. Suppl.*, 52B:139–141, 1997.
- [88] J. Engler, F. Fessler, J.R. Hörandel, T. Holst, H. Keim, H.J. Mathes, H.H. Mielke, J. Milke, U. Raidt, and J. Wochele. “A warm-liquid calorimeter for cosmic-ray hadrons”. *Nucl. Instrum. Meth. A*, 427(3):528 – 542, 1999.
- [89] S. Plewnia, Th. Berghöfer, J. Blümer, P. Buchholz, J. Engler, N.O. Hashim, J.R. Hörandel, R. Lixandru, J. Milke, W. Walkowiak, and J. Wochele. “A sampling calorimeter with warm-liquid ionization chambers”. *Nucl. Instrum. Meth. A*, 566(2):422 – 432, 2006.
- [90] H. Bozdog, M. Elzer, H.J. Gils, A. Haungs, F. Herm, H. Koepf, K.U. Köhler, M. Kretschmer, H. Leibrock, H.J. Mathes, M. Petcu, D. Pröhl, H. Rebel, J. Wentz, A. Wolf, and S. Zagrowski. “The detector system for measurement of multiple cosmic muons in the central detector of KASCADE”. *Nucl. Instrum. Meth. A*, 465(2-3):455 – 471, 2001.
- [91] W.D. Apel et al. [Łuczak](KASCADE-Grande Collaboration). “Comparison of measured and simulated lateral distributions for electrons and muons with KASCADE”. *Astropart. Phys.*, 24(6):467 – 483, 2006.
- [92] A.A. Lagutin and R.I. Raikin. “Lateral distribution of electrons in EAS at superhigh energies: predictions and experimental data”. *Nucl. Phys. Proc. Suppl.*, 97:274–277, 2001.
- [93] A.A. Lagutin, R.I. Raikin, N. Inoue, and A. Misaki. “Electron lateral distribution in air showers: scaling formalism and its implications”. *J. Phys. G*, 28(6):1259, 2002.
- [94] F. Cossavella. “Measurements of high energy cosmic rays above 10 PeV with KASCADE-Grande”. PhD thesis, Universität Karlsruhe, Karlsruhe, 2009. FZKA 7513.
- [95] P. Doll, W. Bartl, C. Büttner, K. Daumiller, K.H. Kampert, H.O. Klages, D. Martello, R. Obenland, L. Pentchev, and J. Zabierowski. “Muon tracking detector for the air shower experiment KASCADE”. *Nucl. Instrum. Meth. A*, 488(3):517 – 535, 2002.
- [96] J. Zabierowski and P. Doll. “Front-end readout boards for streamer tube muon tracking detector in the KASCADE EAS Experiment”. *Nucl. Instrum. Meth.*, A484:528–532, 2002.

- [97] F. Sauli. “Principles of operation of multiwire proportional and drift chambers”. Technical report, CERN, Geneva, May 1977. CERN-77-09.
- [98] J. Zabierowski, H.O. Klages, and H. Schieler. “The trigger electronics for the array part of the KASCADE extensive air shower experiment”. *Nucl. Instrum. Meth. A*, 354(2-3):496 – 500, 1995.
- [99] H. Schieler. “Konzeption, Entwicklung und Test des lokalen Datenerfassungssystems für das strukturierte Detektor-Array von KASCADE”. PhD thesis, Universität Karlsruhe, 1996.
- [100] S. Over. “Development and commissioning of data acquisition systems for the KASCADE-Grande experiment. Master’s thesis, Universität Siegen, 2004.
- [101] R. Glasstetter et al. (KASCADE-Grande Collaboration). “Shower Size Reconstruction at KASCADE-Grande”. In *Proceedings of the 29<sup>th</sup> International Cosmic Ray Conference*, volume 6, page 293–296, Pune, India, 2005. FZKA 7187.
- [102] M. Bertaina et al. [Łuczak](KASCADE-Grande Collaboration). “The all particle energy spectrum of KASCADE-Grande in the energy region  $10^{16} - 10^{18}$  eV by means of the  $N_{ch} - N_{\mu}$  technique”. In *Proceedings of the 31<sup>th</sup> International Cosmic Ray Conference*, Lodz, Poland, 2009. FZKA 7516, p13-16 (0323).
- [103] T. Antoni et al. (KASCADE Collaboration). “Electron, muon, and hadron lateral distributions measured in air-showers by the KASCADE experiment”. *Astropart. Phys.*, 14:245–260, 2001.
- [104] T. Gnielka. “Untersuchungen zur gemeinsamen Analyse der Daten des Myonspurdetektors und des Detektorfeldes im KASCADE-Experiment”. Master’s thesis, Universität Karlsruhe, 2003.
- [105] P. Łuczak et al. (KASCADE-Grande Collaboration). “Muon tracking in KASCADE-Grande: Lateral distributions of EAS muon densities”. In *Proceedings of the 21<sup>st</sup> European Cosmic Ray Symposium*, Kosice, Slovakia, 2008. 6.04.
- [106] P. Łuczak et al. (KASCADE-Grande Collaboration). “Lateral distribution of EAS muons measured with the KASCADE-Grande Muon Tracking Detector”. In *Proceedings of the 31<sup>th</sup> International Cosmic Ray Conference*, Lodz, Poland, 2009. FZKA 7516, p41-44 (0220).
- [107] P. Łuczak, P.Doll, K. Daumiller and J. Zabierowski. “Lateral Distribution of EAS-Muon Density and Pseudorapidity”. Volume T84.2, DPG Frühjahrstagung Verhandlungen - Freiburg, Germany, Mar 2008.

- [108] P. Łuczak, P.Doll, K. Daumiller and J. Zabierowski. “Muon tracking in KASCADE-Grande: the lateral distributions of EAS muon densities”. Volume T98.7, DPG Frühjahrstagung Verhandlungen - Munich, Germany, Mar 2009.
- [109] K. Bernlöhr. “Measuring the UHE cosmic-ray composition with tracking detectors in air-shower arrays”. *Astropart. Phys.*, 5(2):139 – 146, 1996.
- [110] J. Zabierowski, K. Daumiller, and P. Doll. “Properties of tangential and radial angles of muons in EAS”. *Nucl. Phys. Proc. Suppl.*, 122:275–278, 2003.
- [111] J. Zabierowski et al. (KASCADE-Grande Collaboration). “Muon Tracking In KASCADE-Grande: CORSIKA Simulation Study”. In *Proceedings of the 29<sup>th</sup> International Cosmic Ray Conference*, volume 6, pages 357–360, Pune, India, 2005. FZKA 7187.
- [112] W.D. Apel et al. [Łuczak](KASCADE Collaboration). “Energy Spectra of Elemental Groups of Cosmic Rays: Update on the KASCADE Unfolding Analysis”. *Astropart. Phys.*, 31:86–91, 2009. arXiv:astro-ph/0812.0322.
- [113] J.H. Weber et al. (KASCADE Collaboration). “The electron/muon ratio in EAS at and above the “Knee” region”. In *Proceedings of the 25<sup>th</sup> International Cosmic Ray Conference*, Durban, South Africa, 1997. HE 2.1.4.,.
- [114] T. Antoni et al. (KASCDE-Grande Collaboration). “Muon density measurements with the KASCADE central detector”. *Astropart. Phys.*, 16:373–386, 2002.
- [115] P. Łuczak, P.Doll, K. Daumiller and J. Zabierowski. “Study of the longitudinal development of extensive air showers with the Muon Tracking Detector in KASCADE-Grande”. Volume T103.2, DPG Frühjahrstagung Verhandlungen - Bonn, Germany, Mar 2010.
- [116] M. Bertaina et al. [Łuczak](KASCADE-Grande Collaboration). “Results from KASCADE–Grande”. *Nucl. Instrum. Meth. A*, 2012. Article in press doi:10.1016/j.nima.2012.01.008.
- [117] J. Zabierowski, P. Łuczak, P. Doll et al. (KASCADE-Grande Collaboration). “On the primary mass sensitivity of muon pseudorapidities measured with KASCADE-Grande”. In *Proceedings of the 32<sup>nd</sup> International Cosmic Ray Conference*, volume 1, page 220, Beijing, China, 2011.

- [118] W. D. Apel et al. [Łuczak](LOPES Collaboration). “Experimental evidence for the sensitivity of the air-shower radio signal to the longitudinal shower development”. *Phys. Rev. D*, 85:071101, Apr 2012.
- [119] W.D. Apel et al. [Łuczak](KASCADE-Grande Collaboration). “Muon production height studies with the air shower experiment KASCADE-Grande”. *Astropart. Phys.*, 34(6):476 – 485, 2011.
- [120] P. Doll et al. [Łuczak](KASCADE Grande Collaboration). “Muon Production Height investigated by the Air-Shower Experiment KASCADE-Grande”. *Nucl. Phys. B - Proceedings Supplements*, 196:305 – 308, 2009. Proceedings of the XV International Symposium on Very High Energy Cosmic Ray Interactions (ISVHECRI 2008).
- [121] P.Doll, K. Daumiller, P. Łuczak and J. Zabierowski. “Myon-Produktionshöhe und longitudinale Schauerentwicklung bei KASCADE-Grande”. Volume T85.1, DPG Frühjahrstagung Verhandlungen - Freiburg, Germany, Mar 2008.
- [122] P. Doll et al. [Łuczak](KASCADE-Grande Collaboration). “Muon production height and longitudinal shower development in KASCADE-Grande”. In *Proceedings of the 31<sup>th</sup> International Cosmic Ray Conference*, Lodz, Poland, 2009. FZKA 7516, p.45-48 (0429)).
- [123] P.Doll, K. Daumiller, P. Łuczak and J. Zabierowski. “Myon Produktionshöhe und longitudinale Schauerentwicklung bei KASCADE-Grande”. Volume T98.9, DPG Frühjahrstagung Verhandlungen - Munich, Germany, Mar 2009.
- [124] P.Doll, K. Daumiller, P. Łuczak and J. Zabierowski. “Muon Production Height and Longitudinal Shower Development in KASCADE-Grande”. Volume T103.3, DPG Frühjahrstagung Verhandlungen - Bonn, Germany, Mar 2010.
- [125] R. Obenland. “*Verbesserung der Winkelaufloesung des Myonspurdetektors von KASCADE und Bestimmung der Myonproduktionshoe-hen*”. PhD thesis, Universität Karlsruhe, 2005. FZKA 7116.
- [126] C. Büttner et al. (KASCADE Collaboration). “Muon Production Height from the Muon Tracking Detector in KASCADE”. In *Proceedings of the 28<sup>th</sup> International Cosmic Ray Conference*, Tsukuba, Japan, 2003. HE 1.1, p. 33.

# ERRATUM

Page	Line	There is	Should be
4	2	"cascade of photons, leptons, muons and hadrons"	cascade of photons, leptons and hadrons
6	28	"inversly"	inversely
20	11	"featuers"	features
20	12	"estiamate"	estimate
22	9 bottom*	"tunned"	tuned
23	3	"desiged"	designed
23	22	"Normaly"	Normally
40	1	"KASACDE"	KASCADE
43	6	"hight"	height
47	11	"enviroment"	environment
48	7	"milimetres"	millimetres
49	7 bottom	"representsd"	represented
49	6 bottom	"alowed"	allowed
50	3 bottom	"reconsturcted"	reconstructed
69	12 bottom	"form"	from
39	equation 3.2.8	<b>There is:</b> $\delta_\alpha = \arccos(\cos(\theta_K) \cdot \cos(\theta_G) + \sin(\theta_K) \cdot \sin(\theta_G) \cdot \cos(\phi_K - \phi_G))$ <b>Should be:</b> $\delta_\alpha = \arccos(\cos(\theta_K) \cdot \cos(\theta_G) + \sin(\theta_K) \cdot \sin(\theta_G) \cdot \cos(\phi_K - \phi_G))$	
74	equation 8.0.1	<b>There is:</b> $\langle \ln A \rangle = \sum_i r_i A_i$ <b>Should be:</b> $\langle \ln A \rangle = \sum_i r_i \ln A_i$	

\* Number of lines from the bottom of the page.